UNIVERSITÀ DI PADOVA FACOLTÀ DI INGEGNERIA

SCUOLA DI DOTTORATO IN SCIENZE E TECNOLOGIE
DELL'INFORMAZIONE

TESI DI DOTTORATO

Extensive study of reliability and performances of next generation GaN light emitting devices

Supervisore: Prof. Gaudenzio Meneghesso
Direttore della scuola: Prof. Matteo Bertocco

Dottorando: Nicola Trivellin

DIPARTIMENTO DI INGEGNERIA DELL'INFORMAZIONE

Contents

Abstract

This thesis reports the results of a three-year extensive analysis carried out on Light Emitting Diodes (LEDs), Laser Diodes (LDs) and test structures based on Gallium Nitride (GaN) technology. The principal focus of the thesis has been the reliability study of GaN-based next generation optoelectronic devices. The degradation analysis has been carried out in collaboration with manufacturers leading the market for optoelectronic applications, in particular: Panasonic Corp, Osram OS, Sensor Electronic Technology Inc. The purpose of the reliability analysis is to understand: i) what are the effects of the degradation on device's performances and characteristics, ii) which ageing conditions are responsible for degradation iii) which are the degradation modes and mechanisms taking place during the device lifetime, iv) which is the lifetime of the optoelectronic devices when subjected to the operating conditions. The reliability analysis will be obtained by means of standard and accelerated lifetime stress tests; devices will be therefore subjected to several operating conditions with different current, temperature, optical power and voltage in order to obtain the required data necessary fo reliability study and relative analysis. The complete results of the research activity carried out during the Ph.D. period of the candidate are described in the following chapters and appendixes. The main results on the reliability of different optoelectronic devices are summarized in the following:

- For InGaN (Indium Gallium Nitride) Blue laser diode (LD) the degradation is an electro-thermal activated phenomena. The degradation mode is detected as an increase of the LD threshold current. Degradation kinetic is proportional to the square root of stress time, and the degradation is proportional to the stress current. Temperature acts as an accelerating factor, since pure thermal stress does not significantly modify the LD characteristics. The intensity of the coherent optical field taking place inside the optical cavity during lasing operation does not instead significantly influence the degradation. The non radiative lifetime is strongly correlated with the threshold current increase.

- InGaN LED-like samples, with the same epitaxial structure as LD devices, have been subjected to the ageing conditions used for LDs (current density and temperature). Results demonstrate that the LED-like optical power (OP) decrease kinetic is well correlated with the LD I_{th} increase. The OP decrease during degradation is also proportional to the square root of stress time.

- The degradation kinetics of Deep Ultra Violet AlGaN (Aluminum Gallium Nitride) LEDs have only a weak dependence on the junction temperature level, while they are strongly dependent on the stress current level. In addition, pure thermal stress did not determine a significant degradation of the devices. A number of

devices showed catastrophic degradation, with sudden decrease in their optical output. After catastrophic degradation the LEDs behaved as short circuits. By means of failure analysis it has been demonstrated that catastrophic failure is due to the poor definition of the mesa during processing. The generation of localized short-circuit paths in parallel to the junction is caused by an excessive electrical field related to the spike shaped border of the mesa itself.

- Green InGaN LEDs can be substantially damaged by reverse bias polarization. The degradation can be ascribed to the generation/propagation of point defects due to the injection of highly accelerated carriers.During reverse biasing a localized spot luminescence is detected. Leakage current is strongly correlated to the presence of reverse-bias luminescence.

- Different ageing mechanisms are present for InGaN violet LEDs emitting at 420nm: i) a fast electrical and capacitive degradation probably related to a Mg passivation; ii) an OP degradation at high injection regime probably related to defect density increase, iii) a gradual OP increase at low injection regime correlated to an apparent charge decrease in QW region and possibly ascribed to a reduction of Diagonal Tunnelling during ageing, iv) a sudden decrease of OP caused by a localized ohmic shunt path.

- The results of the reliability study on InGaN low flux White LEDs indicate that: (i) stress can induce both the gradual and catastrophic degradation of the LEDs; (ii) the degradation kinetics can be influenced by the stress temperature level, while they have no significant dependence on the stress current level; (iii) stress can induce a strong degradation of the chromatic properties of the analyzed devices; (iv) degradation can be correlated to the worsening of the optical properties of the phosphor-encapsulating material and of the package; (v) catastrophic failure is correlated to the generation of parasitic shunt paths; (vi) after stress a number of devices showed increased thermal resistance, due to the partial detachment of the chip from the package.

Sommario

Questa tesi di dottorato descrive i risultati ottenuti durante un periodo di studio di tre anni su diodi emettitori di luce (LED), diodi laser (LD) ed altre strutture di test basate su Nitruro di Gallio (GaN). Il principale scopo di questa tesi è lo studio dell'affidabilità di dispositivi optoelettronici di nuova generazione cresciuti su GaN. Grazie alla collaborazione di diversi produttori esterni leader di settore come: Panasonic Corp., Osram OS e Sensor Electronic Technologies, è stato possibile studiare diversi dispositivi allo stato dell'arte per prestazioni e tecnologie realizzative. Lo scopo dell'analisi di affidabilità è quello di comprendere nel modo più dettagliato possibile: i) quali sono gli effetti del degrado sulle performance e caratterische dei dispositivi, ii) quali condizioni operative sono responsabili del degradado, iii) quali modi e meccanismi di guasto avvengono durante il tempo di vita del dispositivo, iv) il tempo di vita dei dispositivi quando vengono sottoposti alle condizioni operative. Gli studi di affidabilità sono stati ottenuti sfruttando tecniche di stress accelerato. Sono state inoltre variate di volta in volta le condizioni operative, in particolare temperatura, corrente, potenza ottica e tensione applicata. E' stato quindi possibile ottenere una caratterizzazione completa dei meccanismi di degrado dei dispositivi testati. I risultati ottenuti sono descritti dettagliatamente nei capitoli e nelle appendici successive. Di seguito sono riassunti i principali risultati sull'affidabilità ottenuti su diversi dispositivi optoelettronici:

- Per i diodi laser blu basati su InGaN (Indium Gallium Nitride) il degrado è stato dimostrato essere un fenomeno elettro-termicamente attivato. Il modo di guasto si presenta come un aumento della corrente di soglia (I_{th}) durante la vita del dispositivo, nessuna sostanziale modifica è stata invece rivelata per l'efficiensa differenziale (SE). La cinetica di degrado è proporzionale alla radice quadrata del tempo di stress, mentre l'intensità del degrado dipende linearmente dalla corrente di polarizzazione. La temperatura agisce come un fattore di accelerazione del degrado, le proprietà dei dispositivi non sono infatti influenzate in modo sensibile da stress test puramente termici. Il campo ottico presente all'interno della cavità ottica e nella regione attiva non ha influenza diretta sull'affidabilità dei diodi laser. E' stato inoltre dimostrato come la variazione del coefficiente di ricombinazione non radiativo sia fortemente correlato con il degrado delle caratteristiche ottiche del dispositivo

- Alcuni dispositivi LED-like, con la stessa struttura epitassiale dei Laser diode, sono stati sottoposti a test di affidabilità con le stesse condizioni di quelle dei LD (densità di corrente e temperatura). I risultati hanno dimostrato un calo della potenza ottica proporzionale a quello della variazione della I_{th} dei LD. Anche nel caso dei LED-like il degrado è proporzionale alla radice del tempo di vita.

- Le cinetiche di degrado di Deep Ultra Violet LED basati su AlGaN (Aluminum Gallium Nitride) sono influenzate solo in modo minimo dalla temperatura di giunzione, mentre dipendono fortemente dalla corrente di stress. Anche in questo caso uno stress puramente termico non induce un degrado sensibile nei dispositivi testati. Un certo numero di dispositivi ha inoltre evidenziato un degrado catastrofico, ovvero un'improvvisa e sostanziale diminuzione della potenza ottica emessa, durante i test di affidabilità. Questo fenomeno è legato ad una scarsa definizione dei bordi della struttura LED che causano un localizzato aumento del campo elettrico e la conseguente creazione di percorsi di conduzione che cortocircuitano la giunzione del diodo stesso.

- E' stata valutata l'affidabilità di Diodi LED con emissione sul verde basati su InGaN sottoposti ad una polarizzazione inversa della giunzione. Il meccanismo di guasto si la creazione di difetti puntuali che agiscono come centri di generazione/ricombinazione a causa dell'iniezione di cariche altamente accelerate nella giunzione. Durante la polarizzazione inversa è stato inoltre dimostrato un meccanismo di elettroluminescenza puntuale. Tale meccanismo di elettroluminescenza è strettamente legato alla corrente di leakage.

- Diversi meccanismi di invecchiamento sono invece presenti nei dispositivi LED basati su InGaN con emissione nel violetto (420 nm). i)degrado rapido delle caratteristiche elettriche e capacitive probabilmente dovuto ad un calo del drogante Mg di tipo p, ii)degrado delle caratteristiche ottiche agli alti livelli di iniezione dovuto ad un possibile aumento della densità di difetti, iii)incremento graduale della OP alle basse iniezioni di corrente correlato con la diminuzione della densità di carica apparante nella regione delle QW ed imputabile ad un calo della corrente di Diagonal Tunnelling durante l'invecchiamento del dispositivo, iv)diminuzione repentina della OP in seguito alla creazione di meccanismi di conduzione resistivi localizzati nelle zone dei contatti di tipo n.

- Sudi di effidabilità effettuati su LED bianchi cresciuti in InGaN indicano che: i) lo stress elettrotermico può indurre sia degrado graduale che catastrofico dei dispositivi, ii) le cinetiche di degrado sono influenzate maggiormente dalla temperatura di invecchiamento, mentre il livello di corrente non ha un grande effetto sul degrado dei dispositivi, iii) le proprietà cromatiche dei dispositivi possono essere profondamente influenzate durante il degrado, iv) il degrado è imputabile al deterioramento delle caratteristiche del materiale di incapsulamento che contiene i fosfori ed al package, v) il degrado catastrofico è legato alla generazione di percorsi parassiti di conduzione di tipo shunt; vi) Al termine dei test di degrado alcuni dispositivi mostrano un sostanziale aumento della resistenza termica a causa del distacco parziale del chip dalla superficie di contatto.

Introduction

Thankfully to the continuous research carried out in the optoelectronic and compound semiconductor fields during the last decades, we are now approaching a new era of the illumination: the solid state lighting. Gallium Nitride and in general III-Nitride semiconductor have been immediately recognized as highly promising material for the development of high energy optoelectronic devices. Since the first working GaN LED produced by Pankove in 1971 and based on a metallic intrinsic N tyoe structure [1], several efforts has been done to bring to life a blue LED with improved efficiency and performances that would allow mass market distribution.

During the last decade, GaN alloys represented the reference materials for the optoelectronic devices working in the visible and UV range: in particular Blue, Green, UV, phosphor converted white LED and blue (and recently green) Laser Diode are now available on the market. Particularly interesting is the field of solid state lighting where white LED are now entering the market with superior performances with respect to traditional lighting systems. The development of GaN Laser Diode has also open the way to the Blu-Ray disk [2], where in order to increase the data density a reduced wavelength laser was needed to both write and read discs, and green LD that will be soon introduced for pocket size projector based on laser lights [3].

GaN based devices are also important in medical and biological field for example with the introduction of LEDs emitting in the UV and "‘Actinic wavelenght"’ spectra (i.e. absorption region of chlorophill). However, the effective penetration of these devices in the application market strongly depends on several factors which limit their practical performances and in particular their reliability; while some studies have demonstrated a lifetime of several thousands of hours [4], the reliability of such devices during operation, in particular at high output power levels is still a critical issue.

The better comprehension of the reliability issues of this devices is fundamental for the diffusion not only of high efficiency solid state lighting systems that can sensibly reduce the amount of energy consumed every day (and night), but also to develop new application in medical, biological and also entertainment field, that can atand the initial high costs only in return of guaranteed high reliability.

This need is surely understood by the international research community and during the last years, the performances and in particular the reliability of GaN-based optoelectronic devices have been studied by several groups and international projects [5] [6] [7]. Even if these works have studied the degradation mechanism involved in degradation like: gliding of dislocations [8], formation of non-raditive defects [9], impurity diffusion [10], decrease of injection efficiency [11], and many others, something is still missing: a sistematic and precise characterization of the degradation kinetics when devices are subjected to different ageing conditions. The work presented in this thesis is based around this principle. As it is possible to see in the following chapters the principal degradation analysis tools that will be applied are the comparison and correlation of degradation kinetics with stress condition. This will allow a systematical study of the cause-effect in the GaN optoelectronic devices reliability issues.

Chapter 1

GaN: a revolutionary material

1.1 Introduction to III-Nitride compound semiconductor materials

The most well known semiconductor for electronic applications is Silicon, this material is the most important and widely spread semiconductor for electronic devices. The fundamental characteristic that made Silicon so important for the semiconductor market is not the material itself but his intrinsic oxide. Silicon oxide (SiO_2) properties make SiO_2 nearly perfect for electronic manufacturing: native, stable, insulating and easily processable. Thankfully to deep researches and continuous technological developments Silicon technology is now able to produce more than 3 Billion transistor on a single chip. This material is therefore optimal for electron devices, like transistor and memories, unfortunately the reduced (1.24eV) and indirect bandgap make Silicon not suitable for Optoelectronic light emitting devices at visible wavelength. For many years several semiconductor materials have been studied in order to obtain good performances at different wavelengths (both Infrared, visibile and Ultraviolet). In the last three decades the compound semiconductor materials, in particular the III-V group, has been viewed as highly promising for light emitting devices. III-Nitride group: GaN, AlN, InN and their alloys are all wide-bandgap semiconductors and can crystallize both in wurtzite and zincblende structures. With a wurtzite Bandgap of 3.4, 6.2 and 1.9 eV respectively they are suitable for UV, blue and green emitters. Since Gallium Nitride (GaN) is the principal semiconductor material for the nitride family we will refer in the following to GaN based techology and devices, but AlN and InN are fundamental for their alloys with GaN: AlGaN and InGaN. The GaN based devices have been seen, since a long time, as keystone in the development of solid state illumination systems and high energy laser diodes. We should therefore not be surprised that many efforts have been directed toward the development of GaN techology during the last three decades. Several challenges are still to be solved in therm of substrates, growth of epitaxial layers, creation of different alloys with InN and AlN, doping and contacts. One particular difficulty in the growth of GaN structure is the very limited availability and cost of large single crystal to be used as substrates. For this reason during the years several substrates of different materials have been used, in particular Shappire and Silicon Carbide. However, the use of a foreign substrate lead to several disadvantages: high treading dislocation density (TDD), electrical isolation, reduced thermal conductivity and optical opacity. Therefore several methods have been studied to obtain thick buffer of GaN with reduced TDD on foreign substrates, the most promising is the Epitaxial lateral overgrowth (ELO) which has been used for some of the devices studied in this work. Many epitaxial growth process have also been developed, the most important are: Molecular Beam Epitaxy (MBE), Hydride Vapor Phase Epitaxy (HVPE) and MetalOrganic Chemical Vapor Deposition (MOCVD). Thanks to its high epitaxial quality and the ability to grow abrupt layers, MOCVD (also known as MO Vapor Phase Epitaxy - MOVPE) is the most used for both light emitting devices and electronic devices. Also in this field several challenges are still limiting the efficiency and quality of the crystals, in particular the research of optimal growth conditions (temperature, pressure, precursors, etc) is the main objective to achieve. The development of high efficiency devices is based on the capacity to obtain good confinement structures and reduce power dissipation, and therefore a good control of Nitride alloys (in particular InGaN and AlGaN), dopings and contacts. GaN doping, in particular p-type, has been critical for several years. Before starting any in dept discussion on GaN based devices it is important to first understand the physics, and in particular optical properties of GaN, the several characteristic of the substrates materials, the differences between the growth techniques, the properties and availability of Nitride alloys and finally the doping and contacts necessary to obtain the junction an electrical connection of the light emitting devices.

1.2 Physics of GaN

1.2.1 Crystal forms

The properties of a semiconductor are strictly related to the lattice structure of the crystal. This is also true for III-V compound semiconductors where the crystalline structure is formed by atoms of different elements. Compound semiconductor have several possible phases, or lattice structures, some of them are stable, others are metastable. The most stable phase of III-Nitride is hexagonal (i.e. wurtzite structure 1.1a)), while the cubic form (zincblend 1.1b)) is generally metastable and not used for optoelectronic devices. The definition of a crystalline structure of GaN is given by three lattice constants (a,b,c) and three angles α, β and γ.

Wurtzite lattice has an hexagonal structure with equal constants a and b. The c axis is orthogonal to the hexagonal plane. For Wurtzite the constants are $a = b \neq c$, $\alpha = \beta = 90$ and $\gamma = 120$. The lattice is in fact a sequence of Gallium and Nitride atom surfaces which are placed along c axis. Thus, the Wurtzite is formed by two hexagonal lattice structures com penetrated.

Zincblend lattice instead is formed with Nitride atoms which are placed in a cubic structure and bonded to a thetraedric lattice formed by Gallium atoms. Thus, the Zincblend is formed by two cubic lattice structures compenetrated; Zincblend has $a = b = c$ and $\alpha = \beta = \gamma = 90$.

Cubic-GaN phase will not be discussed further in the following since it properties makes it inefficient for optoelectronic devices and it is therefore not used for the realization of optoelectronic devices.

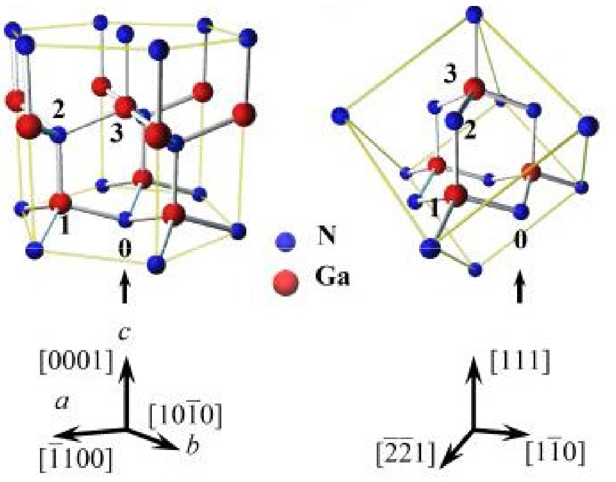

Figure 1.1: Schematic diagram of Wurtzite and Zincblend structure

Properties (300K)	Symbol	Ge	Si	GaAs	GaP	GaN
Crystal structure (D=Diamond, Z=Zincblende, W=Wurtzite)		D	D	Z	Z	W Z
Gap (D=Direct, I=indirect)		I	I	D	I	D
Lattice constant	$a_0 = b_0$[Å] c_0 [Å]	5.64	5.43	5.65	5.45	3.19 4.52 5.19 4.52
Bandgap energy	$E_g[eV]$	0.66	1.12	1.42	2.26	3.44 3.3
Intrinsic carriers concentration	$n_i[cm^{-3}]$	$2{\times}10^{13}$	$1{\times}10^{10}$	$2{\times}10^{16}$	$1.6{\times}10^{10}$	$1.9{\times}10^{10}$
Electron mobility	$\mu_n[cm^2/Vs]$	3900	1500	8500	110	1500
Hole mobility	$\mu_p[cm^2/Vs]$	1900	450	400	75	30
Electron diffusion constant	$D_n[cm^2/s]$	101	39	220	2.9	39
Hole diffusion constant	$D_p[cm^2/s]$	49	12	10	2	0.75
Electron affinity	$\chi[V]$	4.0	4.05	4.07		4.1
Refractive index	n_{opt}	4.0	3.3	3.4		2.67 2.5
Breakdown field	$\varepsilon_1[\times 10^5$ V/cm]	0.8	3	3.5		33
Thermal conductivity	$k[W(cm\ k)^{-1}]$	0.606	1.412	0.455	0.97	1.5

Figure 1.2: Compound semiconductor properties.

1.2.2 Polarization properties

The spontaneous and piezoelectric polarization properties of Nitride semiconductors are becoming more and more important for the development of optoelectronic devices, in the last years the interest has exponentially grown around crystal planes different from the standard [0001] c-axis to allow the development of non-polar and semipolar structures.

Spontaneous polarization

The spontaneous polarization along the c-axis is due to the Coulomb interaction between atoms caused by an absence of an inversion symmetry along the [0001] axis and because of the large ionicity of the metal-nitrogen bond. The values of spontaneous polarization have been calculated by Zoroddu et al. and reported in table 1.1 [12]. The direction of the spontaneous polarization field is parallel to the c-axis, while the sense is related to the different face pointing up (Ga or N) 1.3. For the GaN, the spontaneous polarization effect can lead to an internal electric field of up to 3 MV/cm, as extracted from optical measurement by

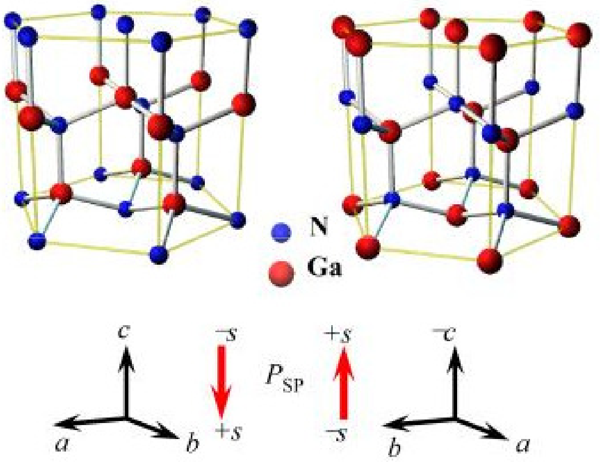

Figure 1.3: Schematic diagram of Wurtzite and Zincblend structure

Parameter $[C/m^2]$	GaN	InN	AlN
Spontaneous polarization	-0.032	-0.041	-0.1
Piezoelectric constant e_{33}	0.86	1.09	1.8
Piezoelectric constant e_{31}	-0.4	-0.52	-0.64

Table 1.1: Spontaneous polarization and piezoelectric constant of II-Nitrides

Piezoelectric polarization

When heteroepitaxial structures are grown, tensile or compressive strain of the different material crystalline structure take place as a consequence of the different lattice constants; the constant a_0 is equal to 3.189Åfor GaN, 3.112Åfor AlN and 3.54Åfor InN.

The strain induces a piezoelectric polarization field in the crystal that has important effects on the electrical and optical properties of the semiconductor because it causes the bending of the band structure. Thin heterostructures like Quantum Wells and superlattices are particularly sensible to the piezoelectric field [13].

The physical properties of GaN make it an attractive semiconductor for many electronic and optoelectronic devices. Its wide, direct energy band gap makes it suitable for short wavelength emitters that are analyzed in this work. The wide energy bandgap and good thermal stability of GaN is also advantageous for high-temperature (HT)and high power electronics. Gallium nitride forms solid solutions with AlN and InN, making a wide range (1.9 - 6.2 eV) of energy bandgap possible. This ability to form alloys is essential for producing specific wavelengths for LEDs and laser diodes, in this

1.3 Substrates for GaN devices

The epitaxial growth of a crystal needs to be carried out on a substrate where the crystal structure starts to grow. As a consequence the quality of the GaN films is very dependent on the properties of the substrate. In order to grow a crystal virtually free of dislocations and defect, the substrate must have lattice constants and thermal expansion coefficients as close as possible to the deposited material. Defects such as threading dislocations, inversion domains, and the unintentional incorporation of impurities into the epitaxial GaN layer resulting from heteroepitaxy are strongly dependent with the type of substrate used. In the following the principal substrates used for Gan devices will be analyzed: Silicon Carbide, Shappire and Silicon; GaN substrate will be also discussed.

1.3.1 Sapphire

Sapphire, single crystal aluminum oxide , was the original substrate used in Maruskas and Tietjen [14] pioneering study of GaN epitaxy by hydride vapor phase epitaxy (HVPE) in 1969, and it remains the most commonly employed substrate for GaN epitaxy. The large lattice constant (15%) mismatch of sapphire (Al_2O_3) with GaN leads to high dislocation density ($10^{10}cm^2$) in the GaN epitaxial film. These high defect densities reduce the charge carrier mobility, reduce the minority carrier lifetime, and decrease the thermal conductivity, all of which degrade device performance. Sapphire's coefficient of thermal expansion is greater than GaN, thus, producing biaxial compressive stress in the layer as it cools down from the deposition temperature, the subsequent bowing of the wafer generate an axial simmetric variation of the crystal properties . One of the reasons sapphire has been so successful as a substrate for GaN epitaxy are it wide availability, hexagonal symmetry, mechanical robustness, temperature stability and low cost. The large lattice constant mismatch between GaN and sapphire causes the film to be completely relaxed (not strained) essentially from the beginning of growth. Consequently, the defect density at the film/substrate interface is very high. The detrimental effect of sapphire large lattice constant mismatch must be ameliorated by a sophisticated processing scheme [15]. First, the substrate surface is treated to remove contaminants, remnant polishing damage, and to produce a step and terrace surface structure. Second, the substrate is nitridated to alter the wetting characteristics of the deposited layers. Third, a thin buffer layer of either GaN or AlN (usually 10 - 100 nm thick) is deposited at a LT and annealed to produce a surface ready for the final epitaxial growth. Schematical results of the crystal structure can be observed from figure 1.4.

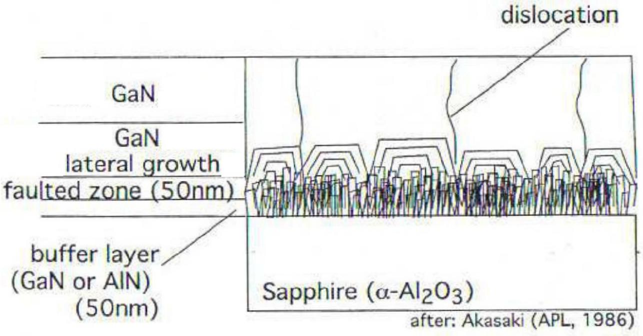

Figure 1.4: Example of GaN defect and dislocation on Sapphire substrate with buffer layer.

The advantage of sapphire for optoelectronic devices consists in his transparency to visible wavelengths. Unfortunately Sapphire is electrically insulating, thus, all electrical contacts must be realized in the front side of the device reducing the available area and causing uneven current distribution on the sample. The disadvantages are compensated by the possibility to realize flip-chip encapsulation devices as it will be discussed in the following.

1.3.2 Silicon Carbide

Silicon carbide (6H-SiC) is another substrate available for GaN devices, the two materials have a reduced lattice mismatch, in the order of 3.5%. Due to this reduced mismatch, a good quality GaN can be growth on a SiC substrate with less lattice and thermal mismatch, consequently, the defect density at the film/substrate interface is not so high related with sapphire. Conductive substrates are available, making electrical contacts to the backside of the substrate possible, thereby simplifying the device structure compared to sapphire substrates (see figure). The crystal planes in epitaxial GaN parallel those of the SiC substrate, making facets formation by cleaving easier. However, SiC does have its disadvantages. Gallium nitride epitaxy directly on SiC is problematic, due to poor wetting between these materials. This can be remedied by using an AlN or AlxGa1/xN buffer layer, but such layers increase the resistance between the device and the substrate. Even though the lattice constant mismatch for SiC is smaller than that for sapphire, it is still sufficiently large to cause a large density of defects to form in the GaN layers. Preparing smooth silicon carbide surfaces is difficult, thus, its surface roughness is an order of magnitude (1 nm RMS) higher than that for sapphire (0.1 nm RMS). This roughness and also remnant subsurface polishing damage are sources of defects in the GaN epitaxial layer. The screw dislocation density in SiC is 10^3 to 10^4 cm^2, and these defects may propagate into the GaN epitaxial layer and degrade device performance. SiC's thermal expansion coefficient is less than that of AlN or GaN, thus, the films are typically under biaxial tension at room temperature. Lastly, the cost of silicon carbide substrates is high, and currently single crystal SiC is produced by relatively few manufacturers.

1.3.3 GaN

The high quality material required for GaN laser diode has pushed toward the development of intrinsic GaN substrates thus eliminating all the problem of heteroepitaxy, but only in last few years it has been possible to grow GaN on native substrate bulk. Homoepitaxy offers better control over the crystal polarity, dopant concentration, and strained layer thickness. Gallium nitride homoepitaxy of smooth films in a two-dimensional growth mode does not require nitridation or buffer layers, as is required for sapphire and silicon carbide. Unfortunately obtaining GaN substrates is extremely difficult and expensive. Although there are several techniques under development for producing bulk GaN crystals including growth by vapor phase transport, growth from supercritical fluids, and growth from sodium fluxes, only high pressure growth from solutions and hydride vapor phase epitaxy have produced usable area crystals [16]. The production of an thick GaN bulk layer is generally obtained with HVPE (Hydrogen Vapor Phase Epitaxy) over a layer of sapphire [17] or GaAs [18], then the GaN layer is removed and used for homoepitaxy. This kind of growth is quite fast and for a thick GaN layer the dislocation density at the surface is small. To date optoelectronic devices with GaN substrate are entering the market solving critical problems of efficiency, maximum output power and stability. The Blu-Ray laser diode analyzed in this work are produced using a GaN substrate.

1.4 Growth of GaN

1.4.1 Hydride Vapor Phase Epitaxy

HVPE is a technique based on the reaction between a metallic chloride and a group V metal hydride that take place over the substrate to form the crystal film. To obtain the metallic Ga chloride an HCl gas is flown over a metallic Ga sample at a temperature of 900řC before entering the chamber. The reactor is sketched in Fig. 1.5

The chemical reation is expressed as following:

$$GaCl(g) + NH_3(g) \rightleftharpoons GaN(s) + HCl(g) + H_2(g)$$

As can be noticed both reaction are available: it is possible to create GaN or to etch it from the substrate depending on the reaction temperature. Maruska and Tietjen grown GaN with a metallic Ga temperature and sapphire substrate of 900řC and 825řC respectively. HVPE has one major issue related to the GaCl generation inside the chamber, therefore GaCl gas cannot be finely tuned with a vent-run arrangement. The system is not suitable to obtain the compositional control and fast flow rate change necessary for the growth of III-N alloys and nanostructures. However HVPE has still one big advantage over other techniques, growth rate is much higher; thus it is still used nowadays for the realization of thick GaN layers and therefore it is the principal method used for the growth of self standing GaN substrates.

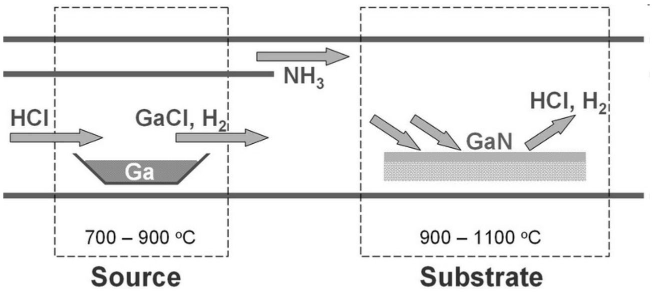

Figure 1.5: Schematic view of the fluxes inside an HVPE reactor.

1.4.2 Metalorganic vapor phase epitaxy

MOVPE, also called Metal organic chemical vapor deposition (MOCVD) is the most used process for III-N optoelectronic devices, it has been first studied in 1990. Vapor phase III group alkyls and V group nitrides reacts in MOCVD chamber at atmospheric pressure over an heated substrate reproducing his crystal structure. The technique utilizes vapor transport of source materials (precursors), subsequent reaction of these materials in the heated zone, and deposition of the final crystalline product on a substrate (see Fig. 1.6. The group III precursors are metalorganic compounds, alkyls that are either trimethylor triethyl based. The most extensively utilized group III sources are trimethylaluminum $Al(CH_3)_2$ (TMAl), trimethylgallium $Ga(CH_3)_2$ (TMGa), and trimethylindium $In(CH_3)_2$ (TMIn) as sources of Aluminum, Indium and Gallium, respectively. The group V precursors are the hydrides PH_3 (phosphine) and NH_3 (ammonia) for phosphide and nitride growth, respectively. Typical dopant precursors are the metalorganic compounds diethylzinc (DEZn), dimethylzinc (DMZn), bis (cyclopentadienyl) magnesium (Cp_2Mg), and diethyltellurium (DETe), as well as hydrides: silane (SiH_4) and disilane (Si_2H_6). Although basic reactions contain intermediate stages that are not completely understood, high quality epitaxial layers are obtained. During the growth process the substrate is placed over a rotating graphite plate initially at 1150 °C, then the temperature is lowered to 450 °C allowing the build up of a low temp buffer layer, then for the real GaN growth the temperature is raised to approximately 1075 °C. The precursors compounds should be stable at normal conditions, but completely decompose on contact with the heated substrate surface. It is also fundamental that precursors do not give any residual impurities. The process is monitored by means of a reflectivity measurement obtained with a 640 nm laser reflected by the wafer surface during growth, this will therefore give a feedback on the growth conditions and rates.

To increase the efficiency of the process, Nakamura in 1997 has developed a new system of MOCVD with the aim to increase the rate of metalorganic compounds that reach the heated substrate and perform a complete reaction. In Nakamura's system, also called two flow MOCVD, one gas flows parallel and the other flows perpendicular to the surface. The configuration suppresses thermal convection currents on the substrate

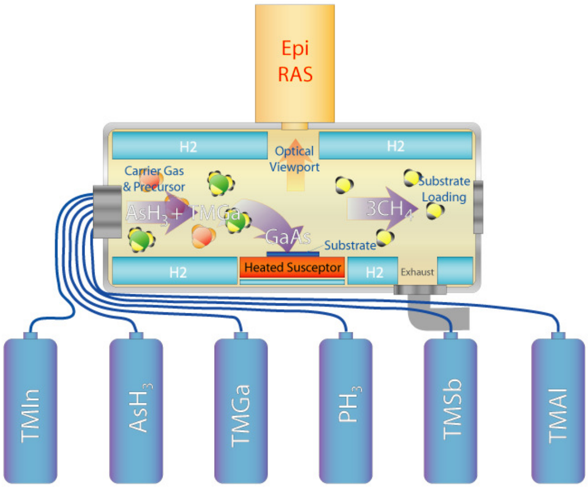

Figure 1.6: Schematic view of the fluxes inside an MOCVD reactor.

and cools the reactant gases just before they react. This lower temperature, in turn, leads to more stable reactions and higher-quality films. A stainless steel chamber contains a rotating susceptor with a sapphire substrate. An example of Nakamura reactor is presented in Fig. 1.7. The precursors are delivered by the horizontal flow through a quartz nozzle, flowing parallel to the substrate. Another flow of inactive gases (N2 + H2) is directed vertically and serves to bring the precursors into contact with the substrate. Prior to the high quality nitride layer, a nucleation layer is grown at reduced temperature (450 to 600°C). Then growth proceeds at higher temperatures (>1000°C), a typical growth rate being 4 $\mu m/h$. Growth takes place at atmospheric or lower pressure. With TF-MOCVD it's possible to achieve an high speed growth with an acceptable dislocation density at the surface of the layer growth. With this technique it is possible to obtain several type of GaN alloys with enough accuracy to realize precise bandgap layers. This geometry helps to reduce parasitic gas phase reactions, especially for nitride ternary alloys, and also enhances the 2D growth mode of the layer, which is favorable for obtaining good quality flat surface. A problem is still present for InGaN alloy with high Indium level: Indium fragmentation occurs and thin layer present an heterogeneous structure. High hydrogen level during reaction is the weak point of the process, to date by several studies H is accused to be the principal responsible for GaN degradation phenomena.

The MOCVD growth process is subdivided in different phases, to monitor the different step the laser reflectivity of the wafer is studied. The lower the reflectivity, the higher is the surface roughness, indicating that a) the coalescence is not good or b) the growth of initial rough nucleation layer is taking place. The oscillations in the reflectivity indicate that constructive and destructive interferences arises from a thickness change in the wafer, the frequency of the oscillations is related to the growth or etching speed. The tipical LED structure

1.4.3 Molecular beam epitaxy

This technique is an Ultra-High-Vacuum (UHV) technique based on simple reaction and it has been invented by Arthur and Cho at Bell Laboratories in the 1960 [19]. It can

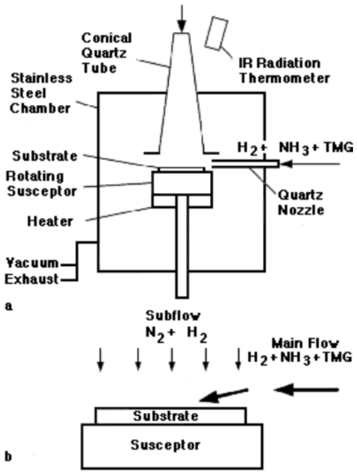

Figure 1.7: Schematic view of two flow MOCVD system.

be used for for nitride, II-VI compounds and silicon growth. With MBE it's possible to achieve a non intentional doping and the reaction is performed at temperature lower than HVPE. Only in last few year it has been possible to use N2 as a source of Nitrogen by means of a plasma source (PMBE, Plasma-Assisted MBE), due to N2 strong bonding energy in the past decades the source for N was ammonia (NH3) with the strong drawback to be also Hydrogen rich. The reaction chamber conditions are a constant pressure of 10^{-10} torr, and a temperature of 800 °C lower than HVPE permits the use of volatile elements like Indium and Magnesium. The Gallium atoms are extracted with thermal evaporation from effusion cells connected to the main chamber and regulated with a shutter as presented in Fig. 1.8. During operation, RHEED (Reflection High Energy Electron Diffraction) is often used for monitoring the growth of the crystal layers. Controlling shutters in front of each effusion cell, allow precise control of the thickness of each layer, down to a single layer of atoms. Intricate layers of different materials may be fabricated this way allowing the build up of heterostructures and MQW structures.

1.5 InN, AlN and alloys with GaN

In this section the different structure and materials that compose the GaN heterostructure are analyzed and discussed.

1.5.1 Nucleation Layer

The nucleation layer is a low temperature buffer layer deposited at the initial stage of the growth over the substrate (in particular with sapphire). It was firstly introduced by Nakamura and Akasaki in 1989 and it sensibly reduces cracks and dislocation density of the subsequent layers. It is composed by an AlN or AlGaN alloy deposited at around 550°C, it is characterized by a low coalescence and it is in fact a 3D structure (as presented in Fig. 1.9) from which, when the temperature starts to increase, a recrystallization takes place and a good growth quality of the successive layers can

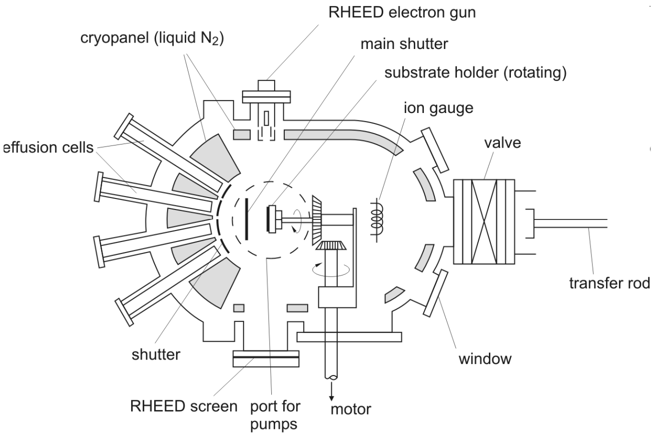

Figure 1.8: Schematic view of an MBE reactor.

be achieved. Nucleation layer is critical for the quality of the entire structure: an accurate control of temperature, starting time and thickness is necessary for an efficient reduction of dislocations.

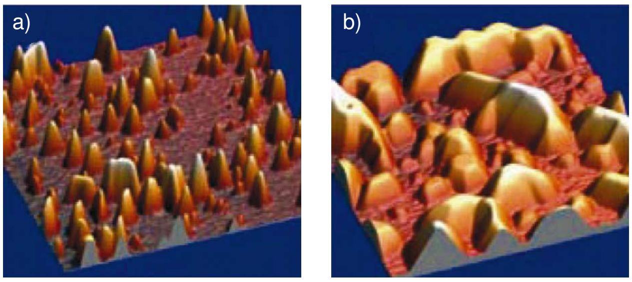

Figure 1.9: AFM view of a nulceation layer a) after the LT nucleation phase and b) during the recrystallization phase.

1.5.2 Gallium Nitride

Gallium Nitride is the main material used in III-Nitride structures. After the deposition of the nucleation layer a thick GaN layer of around 1-2 μ m is grown to allow a full coalescence from the nucleation centers to a flat surface. The GaN layer is generally n type doped to allow the formation of the p-n junction. A GaN layer can be obtained with MOVPE reaction in two different manners, i) at high temperatures (1000-1100 °C) by the mixing of TMGa and NH_3 precursors with hydrogen as a carrier gas or ii) at lower temperatures (750-850 °C) combining TEGa with mmonia.

1.5.3 Indium Gallium Nitride

InGaN is fundamental for the realization of Blue and Green emitting devices with a wavelength greater of 360nm. Since InGaN has to be grown at limited temperature (around 700°C) due to spinoidal decomposition and segregation, TMIn is used in combination with TEGa to obtain low temperature GaN to grow single and multiple quantum wells. A known issue During the growth of InGaN is the generation of Indium clusters, however they are ascribable for the high luminescence of InGaN/GaN devices also if a large treading dislocation is present.

1.5.4 Aluminium Gallium Nitride

AlGaN is used as electron blocking layer to increase current confinement and reduce carrier spilling during operation and to grow Ultra Violet LEDs: up to date wavelenght down to 222-227 nm has been obtained [20]. AlGaN is grown at high temperature (around 1000°C) but has a large lattice mismatch with GaN, which can result in crack and dislocations. For this reason it is generally not grown directly over the GaN bulk layer, but on a AlGaN/GaNsuperlattice to allow the lattice relaxation and reduce the dislocation density [21].

1.6 GaN n-type and p-type doping

The III-Nitride doping is obtained with the inclusion of dopant like Bis (cyclopentadienyl) magnesium (Cp2Mg) or Silane (SiH_4).

1.6.1 n-type doping

Silicon and Germanium are used as an n-type dopants because undoped GaN films had a carrier concentration as low as $10^{16}cm^{-3}$. In order to obtain high blue emission efficiency, the n-type layer requires a high carrier concentration because many electrons must be injected into the p-type layer due to the presence of blue emission centers in the p-layer. Therefore, studies on n-type doping of GaN films are required in order to fabricate high-efficiency emission devices since ptype GaN films can now be obtained. Si and Ge are well known as n-type dopants. The carrier concentration and Hall mobility of undoped GaN films grown with GaN buffer layers are $4x10^{16}cm^{-3}$ and $600cm^2/(Vs)$, respectively. Therefore, by using these high-quality GaN films, the doping efficiency of Si and Ge can be studied accurately in a wide doping range because there are fewer crystal defects or residual impurities in comparison with those of previous studies where the carrier concentration of undoped GaN films was as high as $2x10^{19}cm^{-3}$. During MOVPE growth the Silane (SiH_4) or Germane (GeH_4) gas is injected into the camber and mixed with other precursors to obtain doped crystal.

1.6.2 p-type doping

Ever since research into the GaN system began in the 1960s, the biggest unsolved problem has been the production of p-type GaN. For a long time it was impossible to obtain p-type GaN films. Unavailability of p-type GaN films has prevented III-V nitrides from yielding visible light emitting devices, such as blue LEDs and LDs. In 1989, Amano et al. succeeded in obtaining p-type GaN films using Mg doping, MOCVD, and post low-energy electron-beam irradiation (LEEBI) treatment [22]. After growth, LEEBI (Low Energy Electron Beam Irradiation) treatment was performed for Mg-doped GaN films to obtain a low-resistivity p-type GaN film. The hole concentration and lowest resistivity were $10^{17}cm{-}3$ and $12\Omega cm$, respectively. These values were still insufficient for fabricating blue LDs and high-power blue LEDs. On the other hand, Amano et al. first discovered the LEEBI treatment as a method for obtaining p-type GaN. The effect of the LEEBI treatment was argued to be Mg-displacement due to energy transfer from the electron beam: in the case of as-grown Mg-doped GaN, the Mg atoms occupy sites different from Ga sites where they are acceptors. Under the LEEBI treatment, the Mg atoms move to exactly occupy Ga sites.

In 1992 Nakamura et al. found that p-type GaN with low resistance could be obtained by thermal annealing of the GaN crystal after growth [23]. This thermal annealing technique represents a breakthrough in obtaining p-type III-V nitride films because it is an easy, reliable, and mass-production technique. Thus, the thermal annealing technique is now commonly used to obtain MOCVD-grown p-type GaN layers. The LEEBI treatment makes it possible to obtain a low-resistivity p-type GaN film. With this LEEBI treatment, however, only a very thin surface region of the GaN epitaxial wafer can be a strongly p-type. This is because the low-resistivity region of the Mg-doped GaN film depends on the penetration depth of the incident electrons in the LEEBI treatment. The LEEBI technique has severe restrictions for the fabrication of light emitting devices: only a very thin region close to the surface of the GaN films can be made strongly p-type using LEEBI. Therefore a different method is necessary for the flexible fabrication of optical devices.

In Nakamura experiments, low-resistivity p-type GaN films were obtained by N2-ambient or vacuum-ambient thermal annealing above 700°C. Before thermal annealing, the resistivity of Mg-doped GaN films was approximately $1x10^6\Omega cm$. After thermal annealing at temperatures above 700°C in an N_2 atmosphere, the resistivity, hole carrier concentration, and hole mobility became $2\Omega cm$, $3x10^17cm^{-3}$, and $10cm^2/(Vs)$, respectively. The process was reversible: if the same p-GaN sample was annealed in an NH_3 atmosphere the resistivity goes back to $10^6\Omega cm$ as it is shown in Fig

1.7 Defects on III-Nitride materials

Main causes of reliability fault on solid state devices are the creation of new defects, or modification of existing ones in the crystal structure of the device itself. There are many types of defects with different effect on the device, most relevant are described in this section.

- Strain Effect;
- Point defects;
- Stacking faults;
- Dislocations.

1.7.1 Strain

When GaN is growth on a substrate with a different lattice constant, the difference between the two lattices establish a strain on both crystal structure. In the case of a particularly hard material like GaN, strain can induce crack in the crystal structure. Since lattice strain due to lattice misfit is relaxed by generation of misfit dislocations, lattice strain in GaN thick films grown on sapphire is dominated by compressive strain generated by thermal stress.

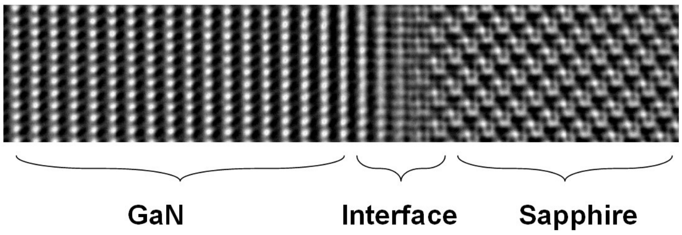

Figure 1.10: TEM image of GaN - Sapphire interface: at the interface strain and defects appear.

1.7.2 Point defects

Point defects are defects which are not extended in space in any dimension. A point defect may be related to impurities trapped in the semiconductor or a vacancy of an atom in the crystal structure.

Vacancies are sites which are usually occupied by an atom but which are unoccupied. If a neighboring atom moves to occupy the vacant site, the vacancy may move in the opposite direction to the site which used to be occupied by the moving atom. GaN may be affected by Nitrogen vacancy (V_N). Recent experimental results indicate that the N vacancy may play a similar role in passivating Mg like Hydrogen, thus reducing the doping in p-type GaN.

Interstitials are atoms which occupy a site in the crystal structure at which there is usually not an atom. They are generally high energy configurations. Small atoms in some crystals can occupy interstices without high energy, such as hydrogen, this is the case of GaN. H is highly present as interstitial due to grow procedure and can react with Mg as said before.

Impurities In the case of an impurity, the atom is often incorporated at a regular atomic site in the crystal structure. GaN main impurities are:

- Oxygen: acts like a surface donor, enhancing n non-intentional doping; main source for H are precursor gases in MOCVD.
- Hydrogen: is the most common, it establishes MgH bonding passivating Magnesium.

- Carbon: present in MOCVD precursor gases, is thought to be CN impurity and thus acts like an acceptor atom [24].

Impurity profiles in a GaN layer can be analyzed in the SIMS image presented in fig. 1.11, while in fig. 1.12 it is noticeable different activation energies for main impurities inside GaN bandgap.

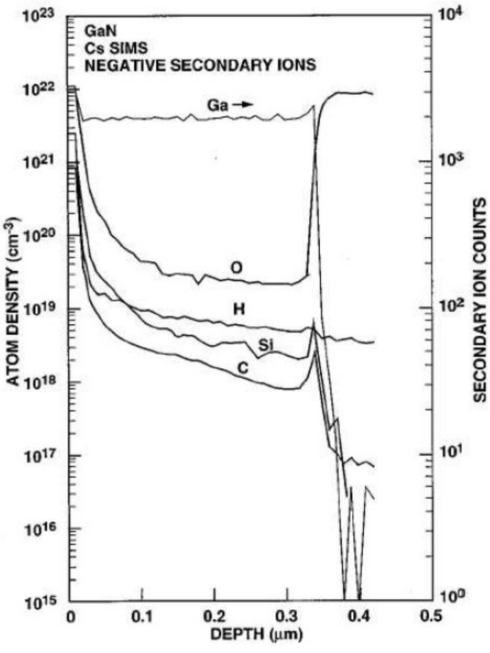

Figure 1.11: Undoped GaN layer SIMS image grown with MOCVD.

1.7.3 Stacking Faults

When the lattice is subjected to strain, a crystal plane interruption may occur so that it can decrease the mechanical tension of the crystal structure itself. This phenomena is called stacking fault and a schematical situation representation is fig 1.13 GaN is particularly affected by stacking faults, especially if grown on Sapphire.

There are several kinds of stacking faults:

- those close to the GaN/substrate interface on c plane that cause vertical propagating defects;
- prismatic faults, generated by planar stacking faults on c plane whose propagate in [0001] direction;
- stacking mismatch boundaries;
- inversion domain boundaries.

Considering the lower thermal mismatch, GaN grown on 6H-SiC has a reduced density of stacking faults. Local bandgap variation is the main effect of stacking faults.

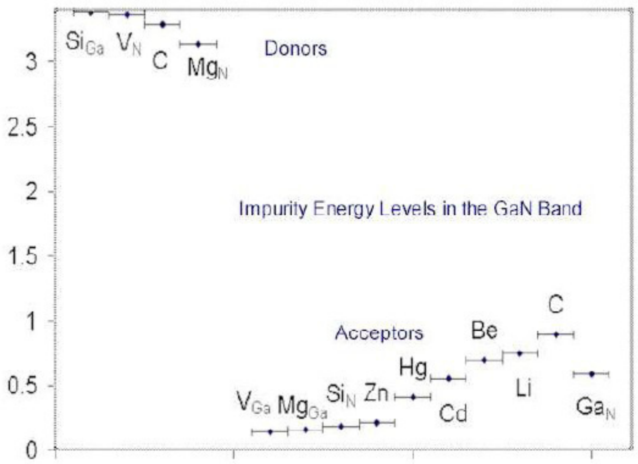

Figure 1.12: Activation energy of main GaN impurities.

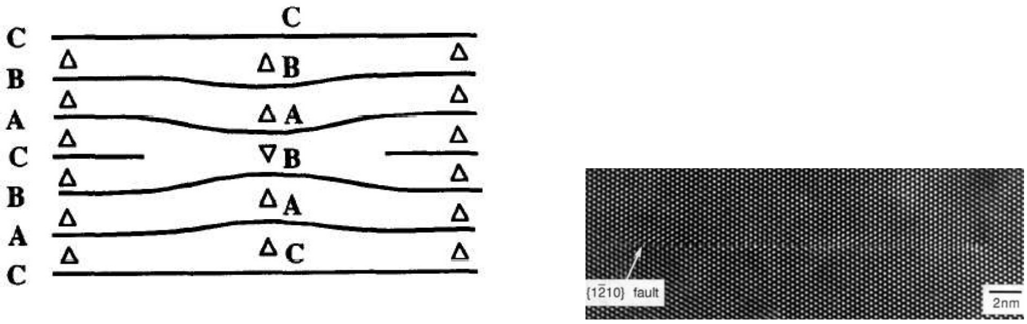

(a)

(b)

Figure 1.13: (a) Schematic representation (a) and SEM image(b) of a stacking fault in GaN lattice.

1.7.4 Dislocation

The strain induced by the epitaxial layer, particularly in multilayer Nitride alloys, can provoke a dislocation in order to reduce the mechanical tension.

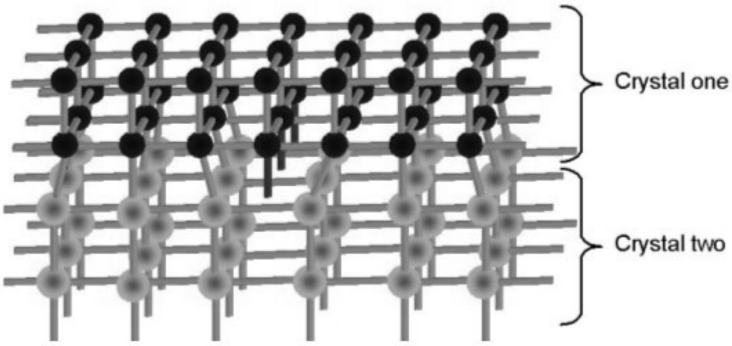

Figure 1.14: Example of a dislocation caused by strain relaxation.

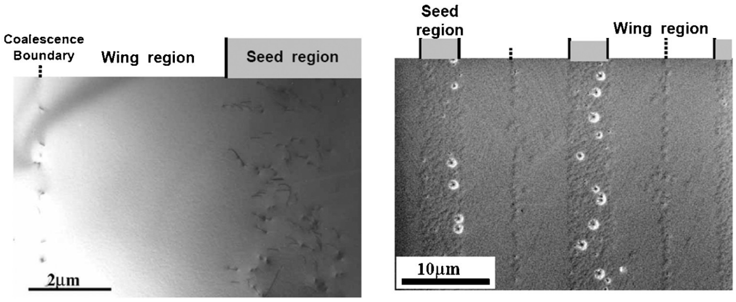

(a)

(b)

Figure 1.15: (a) Plan-view TEM image. (b) SEM image of the ELO GaN surface.

Many types of dislocation have been observed and are generally divided in: perfect, partial, V dislocation. V dislocation are those of main interest, they assume a flippedup pyramidal form with a size varying from 10 to 250 nm, and are common in MQW structure (multi layer Nitride alloys interface). Dislocation mobility on GaN is quite lower than those in GaAs and GaP due to strong GaN bonding energy. Dislocation mobility is 10^{-10} - 10^{-16} times slower than in GaAs at room temperature and 10^{-19} in biasing condition. Dislocations act like non radiative recombination centers, therefore a high dislocation density entails a lower efficiency of the devices and can provoke dark spot on the surface of the device. Using epitaxial lateral overgrowth the problem of high dislocation density on GaN has been reduced by several orders of magnitude. As presented in fig. 1.15 it is possible to see the reduced dislocation densities the wing region. In the case of LDs fabricated from III-V arsenide and phosphide the lifetime is strongly related to the densities of any dislocations that are present. It is important to consider

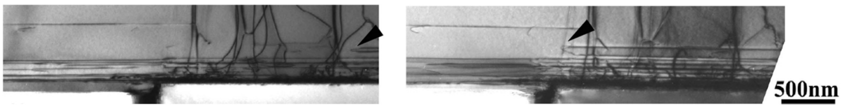

(a) (b)

Figure 1.16: (a) Dislocation in [0001] plane before stress and (b) Glide of the dislocation after stress.

the recombination enhancement effect for dislocation motion in light-emitting devices, since this effect is one of the primary causes of defect growth in III-V arsenides and phosphides. Two modes for dislocation motion has been discovered: dislocation glide and dislocation climb. An applied shear stress is needed for dislocations to glide and is mainly caused by misfit strain. Dislocation multiplication by recombination enhanced dislocation glide (REDG) occurs in this type of devices along the [110] directions, since the intersections between the (001) planes and the slip planes are in the directions. In the case of GaN LDs, their crystal structure is of wurtzite type and their primary slip system is in the direction [0001]. The lattice misfit does not give rise to a shear stress on the primary slip systems, since the primary slip planes are parallel to the device interface [0001] plane. Thus, the dislocations are thought to hardly glide at all. In the work proposed by Tomiya et al. [25], neither dislocation multiplication from the threading dislocations, nor any structural changes of the threading dislocations were observed. Only dislocations lying in the [0001] basal plane move by REDG under a current density below the laser operation threshold current, as can be observed in fig. 1.16. However, the dislocations extending along the c axis were not observed to move nor to glide. ELO GaN growth technique is then also particularly poor in dislocation densities and also in the case of GaN devices narrow the possibility of dislocation glide along c-axis of the crystal structure.

Chapter 2

Light emitting diode technology

Light emitting devices cannot be considered as a simple p-n junction, in order to improve the efficiency both electrically, optically and thermally the devices have been subjected to deep improvements. The final purpose of an LED is to transform injected electrons into extracted photons. For this reason, in order to study the light emission mechanisms inside an LED, it is crucial to comprehend the physics that rule the recombination of carriers and extraction of light from the device structure.

2.1 Physical mechanisms of LEDs

2.1.1 Recombination

The light emission precess inside an LED is based on the radiative electron-hole recombination. In every semiconductor two antagonist phenomena take place: generation and recombination of electron and hole pairs (EHP). Excess carriers can be generated by either absorption of light (with an energy greater than energy bandgap) or by injected current. During a recombination a certain amount of energy, the differential energy of the electron before and after the recombination, is transformed into a different form of energy. The energy resulting from the recombination can be of different forms: heat (phonon), light (photon) and kinetic (in the case of auger recombination). Therefore there recombination mechanisms in semiconductors are classified with different names, radiative, non-radiative and Auger recombination. In a radiative event, one photon with energy equal to the bandgap energy of the semiconductor is emitted, while during non-radiative recombination, the electron energy is converted to vibrational energy of lattice atoms, emitting a phonon, the energy is thus converted in heat. In semiconductor generally two different types of non radiative recombination take place: i) Deep level defect recombinations and ii) surface level recombinations.

2.1.2 Non-radiative recombination

There are several physical mechanisms by which non-radiative recombination can occur [26]. The most common cause for non-radiative recombination events are defects in the crystal structure and Auger recombination. Deep level defect recombination Defect in the crystal structure have energy level structure that are different form substitutional semiconductor atoms. It is quite common for such defects to form one or several energy levels within the forbidden gap of the semiconductor. These are generally called deep levels and recombination through them has been analyzed by Shockley, Hall and Read (SHR theory), the recombination ratio is:

$$R_{SHR} = \frac{p_0 \Delta n + n_0 \Delta p + \Delta n \Delta p}{\left(N_T \nu_p \sigma_p\right)^{-1} (n_0 + n_1 + \Delta n) + \left(N_T \nu_n \sigma_n\right)^{-1} (p_0 + p_1 + \Delta p)} \tag{2.1}$$

where $\Delta n = \Delta p$ are the variation in electron and hole density relative to steady state; ν_n and ν_p are the carrier thermal velocity, and σn and σp are the capture cross sections of the traps. The quantities n_1 and p_1 are the electron and hole concentrations if the Fermi energy is located at the trap levels. It is important to analyze the timing dynamics of the recombination generation process in order to have a powerful instrument to investigate degradation mechanism. The non-radiative lifetime of excess electrons can be deduced from the equation $R_{SHR} = \Delta n / \tau$

$$\frac{1}{\tau} = \frac{p_0 + n_0 + \Delta n}{\tau_{p0}(n_0 + n_1 + \Delta n) + \tau_{n0}(p_0 + p_1 + \Delta p)} \tag{2.2}$$

Assuming that the semiconductor is p-type, and thus hole are majority carrier we have: $p_0 >> n_0$ and $p_0 >> p_1$. Assuming also a small variation from equilibrium ($\Delta n << p_0$), the minority carrier lifetime is given by:

$$\tau = \tau_{n0} \frac{1}{N_T \nu_n \sigma_n} \tag{2.3}$$

while in the case of a n-doped semiconductor we have:

$$\tau = \tau_{p0} \frac{1}{N_T \nu_n \sigma_n} \tag{2.4}$$

Assuming that the trap captures electrons and holes at the same rate: $\nu n \sigma n = \nu p \sigma p$ and $\tau_{n0} = \tau_{p0}$ it is possible to obtain

$$\tau = \tau_{n0} \left(1 + \frac{p_1 + n_1}{2n_i}\right) = \tau_{n0} \left[1 + cosh \left(1 + \frac{E_T + E_F}{kT}\right)\right] \tag{2.5}$$

Where EF is the Fermi level, typically close to the gap. The cosh function has a minimum when the argument of the function is zero. Thus the non-radiative lifetime is minimized, if ET - EF is zero; i.e. when the trap levels, the lifetime is given by $\tau = 2\tau_{n0}$. This result shows the relationship between non-radiative lifetime and level of the recombination center in the bandgap. With this information it is possible to correlate Capacitance-Frequency measurement with the depth of recombination center.

2.1.3 Auger recombination

In Auger recombination process the energy released by EHP recombination is dissipated by excitation of a free electron high into the conduction band, or a hole deeply excited into the valence band. The process is schematically shown in fig. 2.1. The excited carrier will then lose energy by multiple phonon emission until they are close to the band edge. Auger recombination is proportional to the square of the carrier concentration, for example in the case of an electron excitation we have: $R_{Auger} = C_n np^2$. But in a high-excitation situation, where non-equilibrium carriers have a higher concentration than equilibrium carriers, the Auger rate equations reduce to:

$$R_{Auger} = (C_n + C_p)n^3 = Cn^3 \tag{2.6}$$

Although the constant C has a very limited value, in the order of $10^{-30} cm^6/s$, the cubic growth of the Auger recombination term makes it not negligible in the case of high injection regimes. This is the case of state of the art high brightness LEDs which, in order to push the performances, they work with a very high injection current (near to kA/cm^2). Since Auger recombination is a non radiative term it has been considered by many research group as the principal cause for LED "‘droop"’ as we will discuss in the following.

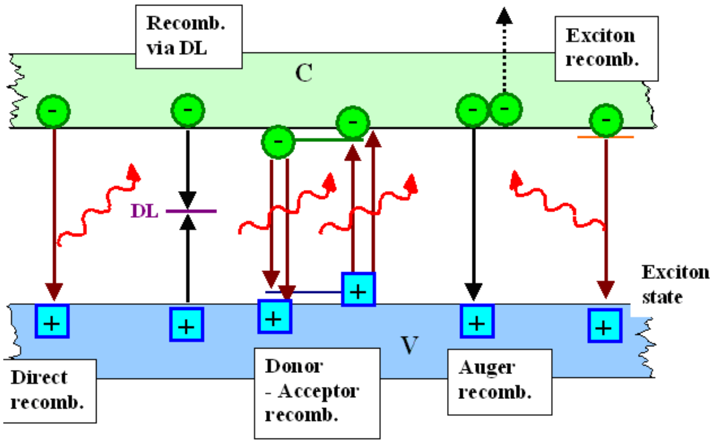

Figure 2.1: Different recombination mechanisms on semiconductors.

2.1.4 Radiative recombination

Radiative recombination is the process that takes place when one or more photon is emitted as a consequence of the energy lost by the recombining electron hole pair, it is based on two different mechanism: spontaneous emission and stimulated emission.

Spontaneous emission If a light radiation with an energy greater than bandgap energy hits a semiconductor, then electron from valence band will be excited and moved to conduction band, thus generating an EHP. This phenomena is called absorption, or pumping for a Laser. The excited electron will, in a time indicated as lifetime, recombine with an hole and emits a photon with a fixed wavelength. The wavelength value varies with the type of recombination that occurs during the event:

$$\lambda_{bb} = \frac{hc}{E_g} \; ; \; \lambda_{intraband} = \frac{hc}{E_g - E_{phonon}} \tag{2.7}$$

respectively in band to band transition and intraband or defect assisted recombination. The emitted spectrum will reveal that the emission is not purely monochromatic, but has a spread due to distribution of electrons and holes in conduction and valence band, and by thermal agitation. Some other wavelength will be also present, caused by recombination through defect or impurity acting like transition levels inside bandgap.

The phase and direction of the emitted light is random, typical of a LED. The spontaneous emission rate, is proportional to the free carrier density injected into the active region.

$$R_{sp} = B_{sp}np$$

Where B_{sp} is constant known as the Einstein radiative recombination factor it has typical values of $10^11..10^9 cm^3/s$ for III-V semiconductors [94], Parameter B decreases with the increase of temperature and with tensile strain. Considering n' and p' intrinsic concentration of electrons and holes, and n_0 and p_0 concentration of free carriers injected in the region we can conclude that the actual densities af electrons and holes are respectively: $n = n_0 + n'$ and $p = p_0 + p'$. The recombination rate is given by the sum of two different coefficients: thermal equilibrium recombination rate R_{sp0} and excess carrier recombination rate R_r.

$$R_{sp} = B_{sp}(n' + n_0)(p' + p_0) = B_{sp}n_0p_0) + B_{sp}(n'p' + n'p_0 + n_0p') = R_{sp0} + R_r \quad (2.8)$$

Considering a strong injection regime we have $n' >> n_0, p_0$, we should also consider the approximation that $n' \approx p'$. Therefore the spontaneous radiative recombination rate can be expressed as:

$$R_{sp} \approx B_{sp}n'^2 \approx B_{sp}n^2 \quad (2.9)$$

As expressed by Equation 2.9, the net recombination rate depends on the availability of electrons in the conduction band and of holes in the valence band. Under equilibrium conditions, net recombination rate is zero.

Stimulated emission and Einstein Approach This type of emission is based on the presence of an "‘external"’ photon with the same energy of the bandgap. An amplification effect is then produced and the photon emitted has the same direction, phase and energy of the "‘external"’ photon, the emission is then called coherent. This is the working principle of the LASER. In order to obtain stimulated emission it is necessary to have a, so called, population inversion. Electrons must be "‘pumped"’ from low energy level to high energy levels, or in the case of semiconductor from valence to conduction band.

The Einstein approach allow us to calculate the recombination dynamics inside a laser cavity with simple considerations and using rate constants to simplify equations.

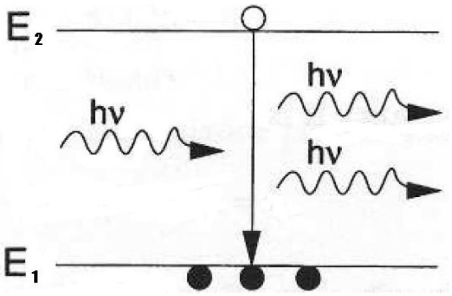

Figure 2.2: Stimulated emission between two levels E_1 and E_2.

It is important to understand the relation between stimulated and spontaneous emission, consider a system presented in fig. 2.2 that has N_1 carriers per unit volume with energy E_1 and N_2 carrier per unit volume with energy E_2. Then the rate of upward transitions from E_1 to E_2 by photon absorption will be proportional to the number of carriers N_1 and also to the number of photons per unit volume with energy $h\nu = E_2 - E_1 : \rho(h\nu)$ which is also the photon energy density per unit frequency. Thus, we can consider different processes: spontaneous recombination, stimulated recombination and generation, using the proportionality Einstein coefficients A_{21}, B_{21} and B_{12} respectively, and onsidering that a simple two level system the the energy of the upward transition is identical to the energy of the downward transition we obtain:

$$R_{21} = A_{21}N_2B_{21}N_2\rho(h\nu) \tag{2.10}$$

$$R_{12} = B_{12}N_1\rho(h\nu) \tag{2.11}$$

To find the Einsten coefficients we consider the events in equilibrium, so that we have:

$$R_{21} = R_{12} \tag{2.12}$$

In equilibrium condition we can use Boltzman approximation and thus we have:

$$N_2 = N_1 exp^{(E_1 - E_2)/k_BT} \tag{2.13}$$

where k_B is the Boltzman constant and T, the absolute temperature. In equilibrium condition the radiation must also reach an equilibrium photon energy density ($\rho_{eq}(h\nu)$) which is given by *PlanckŠs black body radiation law*:

$$\rho_{eq}(h\nu) = \frac{8\pi h\nu^3}{c^3}\left[exp\left(\frac{h\nu}{k_BT}\right) - 1\right]^{-}1 \tag{2.14}$$

Resolving previous equations it can be shown that:

$$B_{12} = B_{21} \text{ } and \text{ } A_{21}/B_{21} = 8\pi h\nu^3/c^3 \tag{2.15}$$

Considering the ratio of stimulated to spontaneous emission we obtain:

$$\frac{R_{21}(stim)}{R_{21}(spon)} = \frac{B_{21}N_2\rho(h\nu)}{A_{21}N_2} = \frac{B_{21}\rho(h\nu)}{A_{21}} \tag{2.16}$$

which can be written as:

$$\frac{R_{21}(stim)}{R_{21}(spon)} = \frac{c^3}{8\pi h\nu^3}\rho(h\nu) \tag{2.17}$$

Another important ratio is stimulated emission to absorption:

$$\frac{R_{21}(stim)}{R_{12}(absorp)} = \frac{N_2}{N_1} \tag{2.18}$$

Concluding it is important to notice that in order to increase stimulated emission to spontaneous emission rate we must have a large photon concentration which is achieved by building an optical cavity to contain photons. Instead to increase stimulated to absorption rate we need to achieve population inversion, that is N2 $>$ N1 which means that we depart from thermal equilibrium.

2.2 External Quantum Efficiency

The external quantum efficiency (EQE) is the ratio of the number of photons emitted from the LED to the number of electrons flowing through the device - in other words, how efficiently the device coverts electrons to photons and allows them to escape. Exteranal efficiency depends on different mechanisms that take place inside the device structure. They are generally subdivided in 3 different parameters: Injection efficiency: η_{inj}; Internal quantum efficiency: IQE; Extraction Efficiency: η_{Extr}

$$EQE = \eta_{inj} x IQE x \eta_{Extr} \tag{2.19}$$

It is important to notice that in order to have the maximum performances of the device all the parameter must analyzed and should as close as possible to the unity. The several aspect that limit these efficiencies and their definition will be analyzed in this section.

2.2.1 Injection efficiency

In order that they can undergo electron-hole recombination to produce photons, the electrons flowing through the device have to be injected into the active region. Injection efficiency is the proportion of electrons passing through the device that are injected into the active region. This parameter has been extensively studied by several authors [27] and several mechanism has been investigate as responsible for a reduced injection efficiency:

- Carrier Spillover: the injected carriers, in particular when operating at high current density, do not distribute in the active region thus allowing recombination, but escape without giving any EHP, electrons (with reduced mass) are more sensible to this phenomena which can therefore be reduced by the introduction of an electron blocking layer. The electron blocking layer is a thin layer of doped high energy semiconductor (generally AlGaN in GaN technology) that reduces electron spillover, while allowing holes conduction by means of tunneling effect, see fig. 2.3.
- Surface Conduction: the presence of dandling bonds on the surface of the device may lead to a conduction path that reduces the amount of carriers flowing trough the active region. The impact of this effect is now quite reduced by means of passivation layer that cover the external surface of the LED device.
- Shunt paths: they are generally related to defects in the wafer structure (like Threading dislocations, stacking faults or impurities). This conduction mechanism can be controlled by improving the growth conditions, but can also appear during device degradation (as reported in the next chapters of this work).

2.2.2 Internal Quantum Efficiency

Not all electron-hole recombinations are radiative. Internal Quantum Efficiency (IQE - also termed Radiative Efficiency) is the proportion of all electron-hole recombinations in the active region that are radiative, producing photons. IQE is probably the

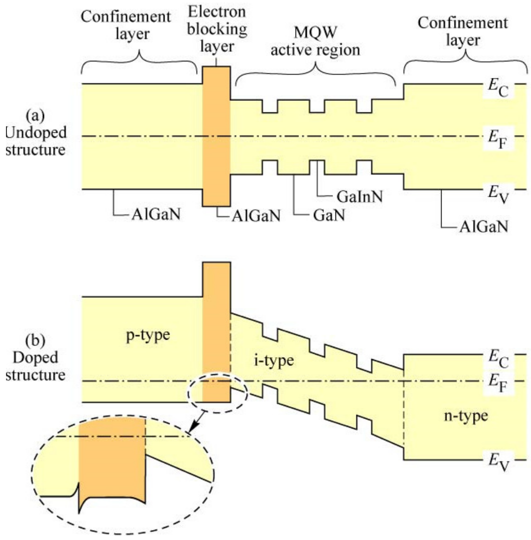

Figure 2.3: Schematic representation of AlGaN Electron blocking layer and effect of doping to allow hole tunneling toward the active region. Courtesy of Schubert [26].

most difficult parameter to study and to ameliorate. It is also difficult to measure, still some controversy exist in the research field on the accuracy of the PL meausurement at different temperatures, as decribed in [28], the IQE at room-temperature can be defined as the ratio between the efficiency of resonantly excited photoluminescence (PL) at room temperature and at low temperature (i.e. 4K) since the extimation of 100 % efficiency at 0K is a quite large assumption. For this reason different methods are now studyed for example a precise simulation of the device structure and comparison with experimental details, as proposed by [29]. The principal causes for a reduced IQE are the non radiative recombinations, both SHR and Auger. They are strictly correlated to the quality of the material and thus the use of improved substrate and growth methods have greatly improved IQE [30] [18] [31].

2.2.3 Extraction Efficiency

Once the photons are produced within the semiconductor device, they have to escape from the crystal in order to produce a light-emitting effect. Extraction efficiency is the proportion of photons generated in the active region that escape from the device. The high refractive index of the semiconductor material limits the fraction of generated light that can be extracted from the device itself (see fig. 2.4), this phenomena is called total internal reflection and greatly reduces the amount of extracted light.

The extraction efficiency is directly correlated with the optical properties of the device, some of the can be modified during growth, like $\lambda/4$ and $\lambda/2$ layer thickness, or during processing, like surface roughness or device shape. Some example are: the increase of surface roughness or the pyramidal shape of the samples. The LED extraction efficiency has also been studied during the PhD visitng period at EPFL- Lausanne, results are reported in the following chapters.

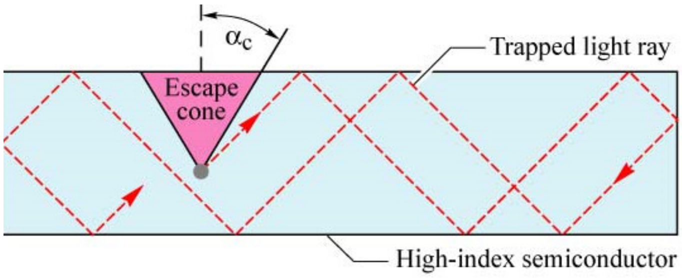

Figure 2.4: Total internal reflection for emission angles grater than the escape cone. Courtesy of Schubert [26]

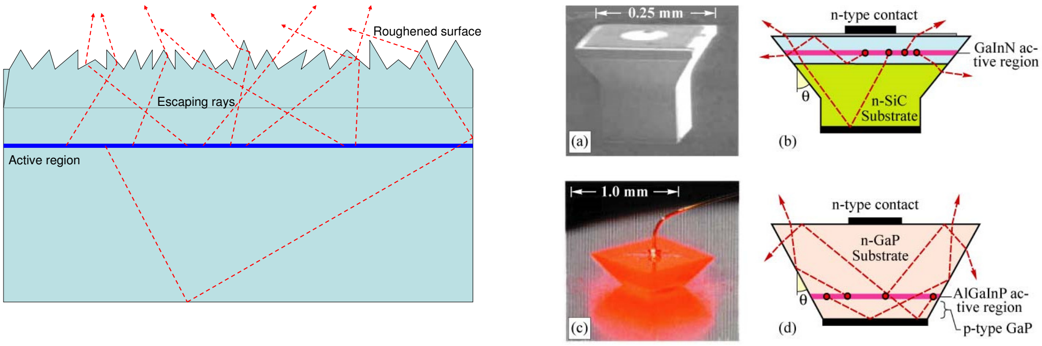

(a) (b)

Figure 2.5: (a) Surface Roughnening and (b) pyramidal shape of LED to increase extraction efficiency. Courtesy of Schubert [26].

Chapter 3

Reliability of InGaN Laser Diodes

The main part of the research carried out during the PhD period has been devolved to the study of the reliability of InGaN Laser Diodes. The work is the result of a collaboration between Panasonic Corp. and DEI, UniPD. Panasonic has supplied with several LD and LED-Like test samples which have been characterized, stressed and in deep studied by DEI.

3.1 Introduction

GaN-based laser diodes (LD) emitting at short wavelength are of great importance for the development of high-capacity optical data storage systems, in particular Blu-Ray disks and next generation High density media. The continuous reduction of the data pit size (in the order of 400nm for Blu-Ray) has required the reduction of the laser wavelength required for reading and writing operations. These devices can emit in the blue-violet spectral range, and will find extensive application in the next-generation optical data storage systems. While low-power laser operation [10 $\div$ 20 mW Optical Power (OP)] is sufficient for disk reading systems, higher operating power levels are required for optical recorders (120 $\div$ 300 mW OP), corresponding to high electrical power (up to 1 W) and current density levels (around $10kA/cm^2$). The effective penetration of these devices in the application market strongly depends on their reliability; while some studies have demonstrated a lifetime of several thousands of hours, the reliability of such devices during operation at high OP levels is still a critical issue.

During the last years, many efforts have been done to study the processes that limit the lifetime of these devices during operation. In particular, works focused on parametric failure have shown that constant optical power or constant current stress imply the gradual increase of the operating and threshold current, that has been attributed to the diffusion of an impurity (e.g. Mg-point defects), possibly across threading dislocations [25] [32]. However, the nature of the diffusion process responsible for devices degradation has not been clarified, as well as its dependence on the stress parameters (current, temperature, optical power).

Over the last few years, a number of authors have investigated the degradation of InGaN-based LDs. Many results have been described so far, particularly in the following studies.

1) Kummler et al. [33] and Furitsch et al. [32] showed that stress at constant OP level can determine the increase in the threshold current of the LDs.

2) Marona et al. [34] showed that during stress the threshold current increases with the square root of stress time.

3) Tomiya et al. [25] suggested that degradation proceeds by the diffusion of point defects through threading dislocations in the active layer. Furthermore, they demonstrated that degradation is not correlated to dislocation multiplication.

4) Nam et al. [35] indicated that the instabilities of the acceptor dopant (magnesium) can influence the performance of devices during stress.

5) Ikeda et al. [2] demonstrated the strong correlation between the lifetime of the LDs and the density of dislocations within the LD stripe, and studied the dependence of lifetime on the OP and temperature levels used for the stress tests.

6) Schoedl et al. [36] analyzed the degradation of the facets of LDs under different atmospheres, namely, dry air, water vapor, and pure nitrogen.

Even if the studies quoted above contributed significantly to the knowledge of LDs reliability, they did not clarify in detail the nature of the physical processes responsible for the degradation. In other words, no comprehensive study of the dependence of the degradation kinetics on the most important driving forces (namely, current, temperature, and OP) has been published up to now. Therefore, it is not clear if LD instabilities are related to a purely thermal effect, or if they depend also on current and high optical field. The aim of this work is to describe a detailed analysis of the degradation of InGaN-based LDs. This analysis consists in a wide set of stress tests carried out under different temperatures, OPs, and current levels. During stress, the electrical and optical characteristics of the samples have been extensively monitored, with the aim of achieving a detailed description of the degradation kinetics. This work provide detailed information on the thermal behavior of the samples, on the activation energy of the analyzed degradation process, on the dependence of degradation kinetics on the different driving forces, and on the modifications of the electrical characteristics of the samples during stress time. The results presented within this work demonstrate that: 1) stress induces an increase in the threshold current of the devices, well correlated to the decrease in the subthreshold emission, thus suggesting that degradation is related to the increase in the nonradiative recombination rate; 2) an increase in stress temperature determines an increase in the degradation rate; 3) the activation energy of the degradation process is equal to 250 meV; 4) pure thermal stress (high temperature storage, with no bias applied to the device) does not induce a significant degradation of device characteristics, the last two points indicate that temperature has a limited impact on the degradation kinetics; 5) the operating OP level does not significantly influence degradation kinetics; and 6) the degradation rate is strongly determined by the stress current level. Therefore, the results presented in this chapter demonstrate that the degradation of the LDs is related to the increase in the nonradiative recombination rate and is due to an electrothermally activated process. Details on the experimental conditions and results are given in the following paragraphs.

3.1.1 Device structure

The structure of the devices is a blue-violet InGaN/GaN MQW devices, produced by Panasonic Corp. LDs are micro stripe gain guided lasers. They are obtained using a GaN substrate bulk grown with ELO process. The chip dimensions are: $200\mu m$ width with a length of $600\mu m$.

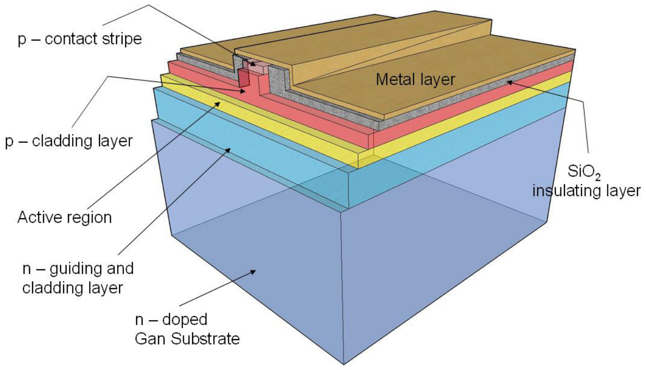

Figure 3.1: Schematical layer structure of the LD.

The microstripe has a thickness of $1.5\mu m$. The devices are grown on a GaN substrate, and by mean of ELO the threading dislocation density has been contained to approx $10^6 cm^{-2}$. From the substrate a Si doped n-type $3\mu m$ GaN buffer layer is grown, followed by an AlGaN cladding layer and an n-type GaN guiding layer. The active region is an undoped InGaN/GaN MQW structure, formed by three consecutive quantum wells. An undoped GaN guiding layer and a p-type AlGaN/GaN cladding/suppression layer cover the active region. Finally a Silicon Dioxide (SiO2) layer is placed in order to confine the current in the microstripe region. The laser diodes are chipped from the wafer and encapsulated in a TO-56 metallic can package, with a top aperture sealed by a semitransparent window. The nominal characteristics of the devices are reported in the table 3.1

Wavelenght range	405-410 nm
Threshold current @ 25°C	30 mA
Threshold current @ 70°C	40mA
Threshold current density @ 25°C	3.3 kA/cm^2
Slope Efficiency	1.6 W/A
V_{on} @ 70mA	4.3 V
Optical output @ 70mA	65 mW

Table 3.1: Nominal characteristics of Blu-Ray laser diodes.

3.2 Preliminary analysis of degradation modes

In order to comprehend the degradation modes that take place during the ageing of the LD devices an initial device has been stressed at nominal conditions and analyzed in order to extrapolate the degradation kinetics during ageing. The device has been stressed at constant optical power (APC- Automatic Power Control) of 65mW at a temperature of 70°C for 10h. Electrical, optical and capacitance measurement has been carried out at RT on the sample named E14. Stress was carried out using our LDC3916 laser driver, and has been stopped at fixed time intervals for the evaluation of the parameters of the devices.

3.2.1 Results

Electrical measurements allow to analyze effects on modifications of conduction mechanisms during device degradation. More detail on time dependence of Vf modifications during stress can be extracted by the analysis of the behavior of LD E14. The I-V curves of the device showed a forward voltage decrease during the initial 10 hours of stress, as described in Fig. 3.2 and Fig. 3.3. These modifications could be ascribed to a temporary increase of the effective doping concentration enhanced by carrier flow, and/or to the modifications of the properties of the contacts during the initial hours of operation of the devices, see also comments on the C-V measurements [37] [38] [11].

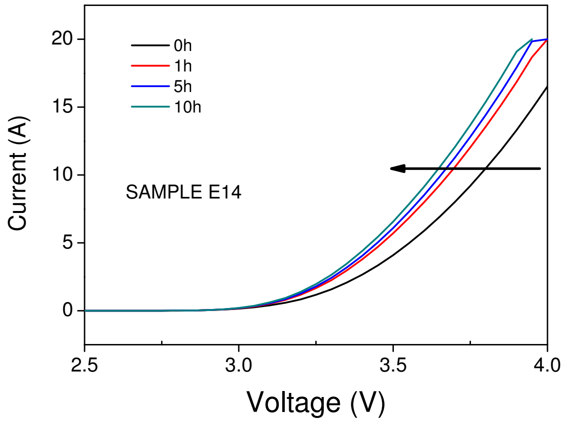

Figure 3.2: Current-Voltage measurements on LD E14 during ageing.

Optical measurements carried out on sample E14 indicated that during the initial 10 hours of stress the threshold current increases as presented in Fig. 3.4 while almost no differences are detected in slope efficiency. At each step of the ageing stress, the threshold current has been evaluated by means of linear fitting of the L-I curves in the optical power range between 1-4 mW. Analyzing the kinetics a monotonic can be observed (Fig. 3.5). Data can be fitted supposing square-root dependence of Ith increase on stress time, as already reported in literature. If confirmed on longer time scales, this dependence would suggest that Ith degradation is driven by a diffusion process, as indicated in previous reports [37] [38] [11] [39]. However, data obtained on a short scale stress are not sufficient. For this reason the next of the thesis has been a complete medium therm characterization of the device degradation kinetic at different driving conditions.

According to previous measurements sub-threshold emission was not significantly affected by the initial 10 hours of stress. Analysis carried out on LD E14, showed that 10 hours of stress can induce a slight decrease of sub-threshold emission, indicating that

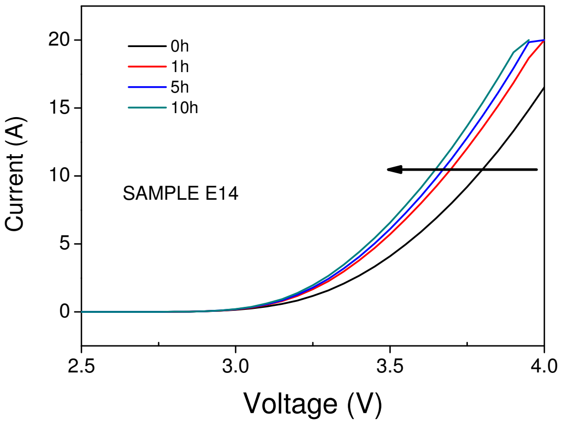

Figure 3.3: Kinetic of forward voltage at 70mA on LD E14 during ageing.

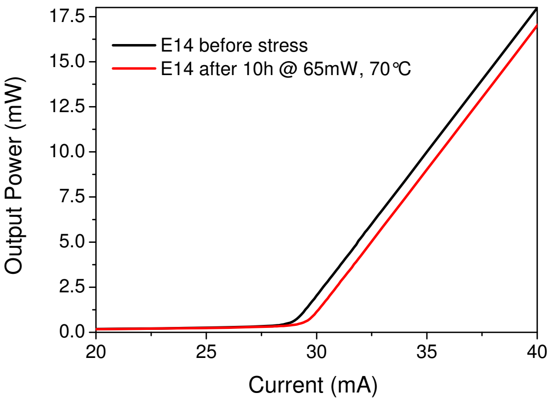

Figure 3.4: L-I plot of LD E14 measured before and after 10h stress.

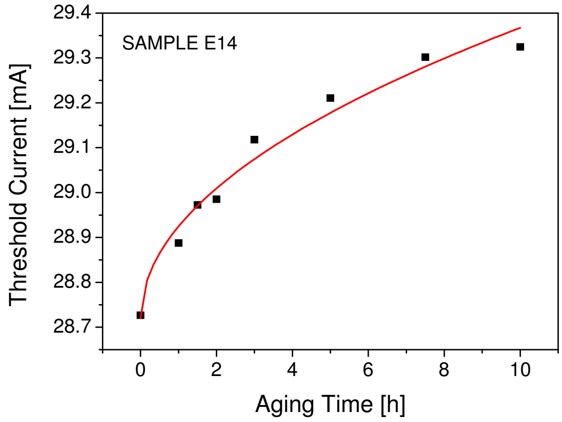

Figure 3.5: Kinetic of threshold current increase on LD E14 during ageing.

an increase of non-radiative recombination rate possibly takes place as a consequence of stress in these devices (Fig. 3.6, in order to confirm this hypothesis during the Ph.D period several in deep tests have been carried out to obtain a complete set of data to be analyzed also for longer stress times.

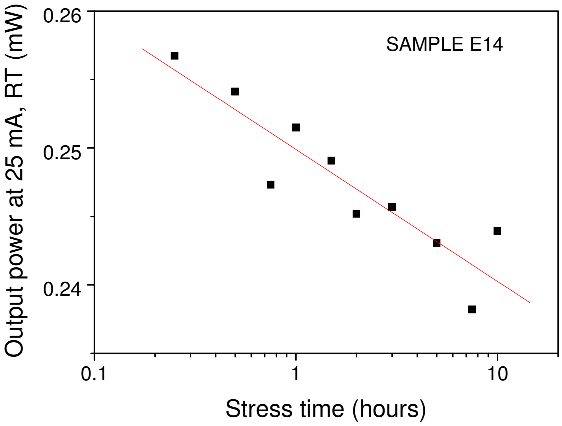

Figure 3.6: Kinetic of sub-threshold OP measured at 25mA on LD E14 during ageing.

Capacitance measurements In order to better understand the degradation modes the analysis of the effects of stress on capacitance is a powerful methode. Details on the capacitance variation during stress has been obtained by the measurements carried out on LD E14 during the 10 hours stress. Results are described in the following.

As presented in Fig. 3.7 the initial 10 hours of stress did not induce significant variation of the C-V characteristics measured at 10 kHz: this indicates stable behavior of the charge distribution close to the active region (step region in C-V curves). On the other hand, modifications were detected in C-V measurements carried out at 1

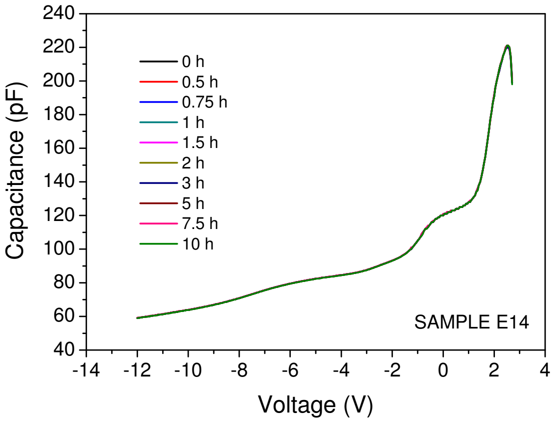

Figure 3.7: Capacitance vs Voltage measurement of LD E14 during ageing, measured at 10kHz (left) and 1MHz (right).

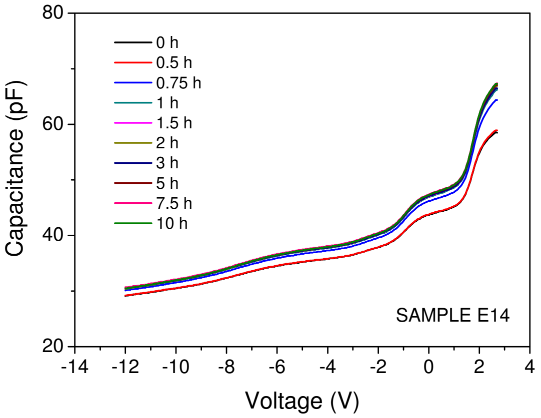

Figure 3.8: Kinetic of sub-threshold OP measured at 25mA on LD E14 during ageing.

MHz: a capacitance increase, mostly concentrated during the initial part of the stress test (initial 2 hours), was detected (Fig. 3.9). C-f measurements (Fig. 3.10) carried out during stress indicate that this slight capacitance increase can be detected only at high frequency levels (>300 kHz), suggesting that these changes can be related to modifications involving shallow levels and/or devices surface.

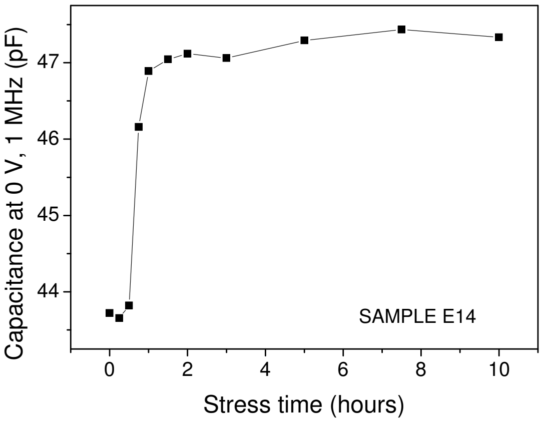

Figure 3.9: Kinetic of sub-threshold OP measured at 25mA on LD E14 during ageing.

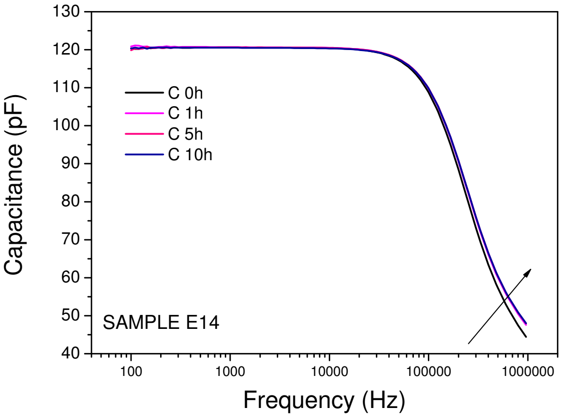

Figure 3.10: Catacitance vs Frequency measured at 0V of LD E14 during ageing.

In general a capacitance increase can be related to (i) an increase of the active charge concentration in the active region, or (ii) to modifications of the properties of the contacts that can slightly change the results of the impedance measurements. Both the effects could be ascribed to modifications in the properties of the p-type dopant, due to a localized increase of effective acceptor concentration during the beginning of the stress (which could be also related to the forward voltage decrease detected by means of the I-V measurements). In order to confirm this speculation, a more detailed analysis has been carried out in the following.

3.2.2 Analysis of the impurity diffusion hypothesis

From the results presented above it is possible to understand that the threshold current increase and the sub-threshold emission have similar kinetics (time evolution) thus suggests that the increase of the non-radiative recombination centers is responsible for both the phenomena. If this hypothesis is veryfied the variations of threshold current can be therefore used as a parameter for analyzing devices degradation. Both the Ith increase and the sub-threshold optical power decrease have been found to be linearly depend on the square root of stress time: this suggests that degradation is dominated by a diffusion process. By means of analytical fitting of the degradation curves, we estimated the characteristic coefficient for the diffusing impurity. Results are explained in the following. We have analyzed the electrical and optical behavior of laser diodes during stress at 65 mW OP, 70 °C, monitoring the variation of optical power vs current (L-I) curves, threshold current, slope efficiency and current vs voltage (I-V) curves of the LD E17. To better understand the phenomena the device E17 has been stressed for a 100h period.

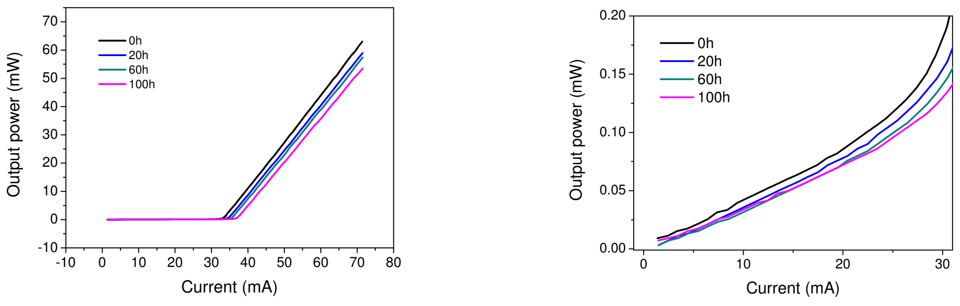

(a) (b)

Figure 3.11: L-I measurement of LD E17 during ageing, on the right a detail of subthreshold OP.

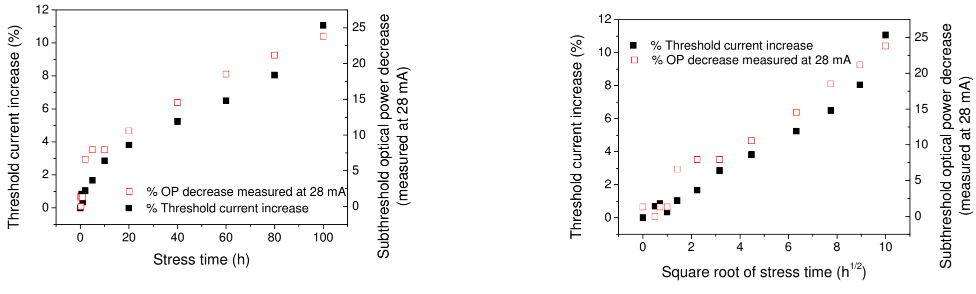

(a) (b)

Figure 3.12: Threshold current and subthreshold OP kinetics in (a) linear and (b) sqaure root of time x scale.

Results indicate that the threshold current increase 3.12 and the sub-threshold emission decrease have similar kinetic, indicating a correlation.

The following consideration can be given:

- Both the parameters (OP and Ith) are related to the spontaneous emission lifetime 3.1, that is related to the radiative (B in eqn. 3.1) and non-radiative (A in eqn. 3) recombination coefficients [40], [26];
- The non-radiative recombination coefficient is related to concentration of trap states inside the active layer (single-trap approximation, eqn. 3.2), that is supposed to increase during stress;
- No change is expected after stress in the radiative emission rate B;
- Both the parameters have a linear dependence on the square-root of time, indicating that possibly a diffusion process is responsible for devices degradation.

We can make the hypothesis that the Ith increase and the sub-threshold emission decrease are related to the diffusion of an impurity that generates trap states in the active layer, thus increasing the non-radiative recombination rate A (eqn. 3.2), determining an Ith increase proportional to the increase of the trap concentration 3.4.

$$\frac{1}{\tau} = A + BN \tag{3.1}$$

$$A = N_{trap}\nu_{th}\sigma \tag{3.2}$$

$$I_{th} \propto \frac{qV}{\eta_i\tau}\Delta A n_{th} = \frac{qV}{\eta_i\tau}\left(A + Bn_{th}\right)n_{th} \tag{3.3}$$

$$\Delta I_{th} \propto \frac{qV}{\eta_i\tau}\Delta A n_{th} \propto \Delta N_{trap} \tag{3.4}$$

Several authors have already demonstrated that APC stress of laser diodes can determine the increase of the threshold current with a square-root of the ageing time. In particular Tomiya, Marona and Furitsh [25], [34], [32] suggested that the impurity responsible for trap generation and optical degradation is magnesium, diffusing from the p-side of the diodes to the active layer. Since the degradation kinetics that we have measured have a linear dependence on the square-root of ageing time, it is possible to calculate the characteristic coefficient for the diffusing impurity, thus understanding its nature.

In the hypothesis that an impurity diffuses from the p-side (n-side) of the diode for a pure-thermal diffusion regime, it can be considered that the concentration itself is constant in the region in which the diffusion starts (see Fig. 3.13 and Fig. 3.14). In this case, after stress the impurity diffuses towards the active layer, and its concentration C depends on the position x according to an erfc function, as described by:

$$C(x,t) = C_{sup} erfc\frac{x}{2\sqrt{Dt}} \tag{3.5}$$

As we have stated above, in the hypothesis that (i) both Ith increase and sub-threshold emission decrease are related to the increase of concentration of one trap-level in the active layer; (ii) the generation of this non-radiative trap level is related to the diffusion of one impurity from the p-side (n-side) of the diodes toward the MQW

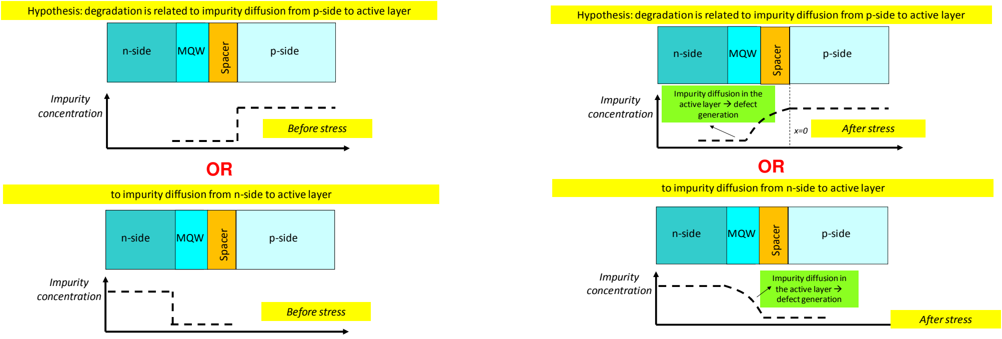

(a) (b)

Figure 3.13: Sketch of the degradation process. a) before stress, impurity concentration (in the p or n-side) is constant. b) stress induces the diffusion of one impurity specie from the p-side (above) or n-side (below) towards the active layer.

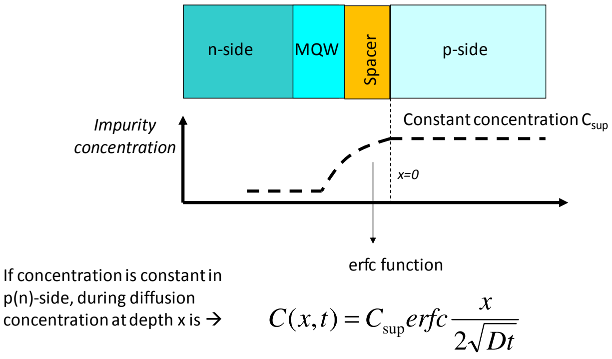

Figure 3.14: The concentration of the diffused species has an Erfc distribution in the cited hypothesis.

region; (iii) after stress the concentration of the diffusing impurity can be described by 3.5; both the Ith increase and the sub-threshold emission decrease can therefore be considered to be directly related to the total amount of impurity diffused in the active region (over a total length L_d), as expressed by:

$$\Delta I_{th} \approx \Delta OP_{sub} \approx \Delta N_{diff} \approx \int_0^{Ld} K \cdot erfc \frac{x}{2\sqrt{Dt}dx} \tag{3.6}$$

Therefore, by fitting the Ith and OP degradation curves by means of (3.6) it is possible to evaluate the diffusion coefficient D, provided that an hypothesis on the diffusion length covered by the process is made. According to the schematic structure of the LDs given by the manufacturer, the Ith degradation curves have been fitted supposing a diffusion length in the range 10-140 nm, that can account for diffusion from both the p-side and the n-side of the diodes). Fitting the I_th increase kinetic by means of (3.6) it is possible to evalute the diffusion coefficient D, see Fig. 3.15). Provided that an hypothesis on the diffusion length covered by the process is made. According to the schematic structure of the LDs, we have fitted the Ith degradation curves supposing a diffusion length in the range 10-140 nm, that can account for diffusion from both the p-side and the n-side of the diodes respectively.

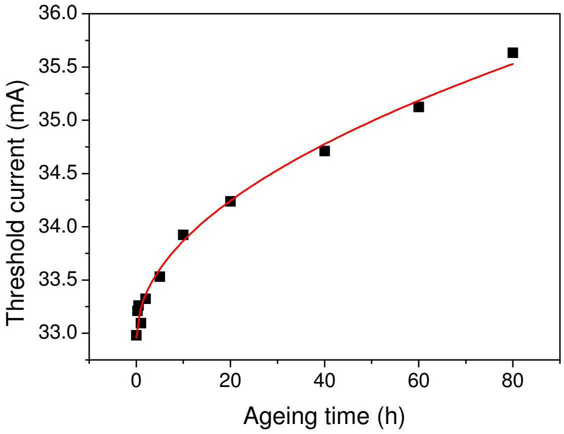

Figure 3.15: Erfc fitting of Ith increase during ageing.

As a result we have found that diffusion constant of "defect/impurity involved in degradation" is in the range $D \approx 1.7x10^{19}cm2s - 1$ at 85 °C (stress temperature estimated considering the thermal resistance and case temperature) as presented in table 3.2. Considering literature data (referred to bulk material and pure-thermally activated diffusion on table 3.3), this constant is too high to be related to magnesium, and indicates that hydrogen can be involved in diffusion process, this if diffusion in our LDs is a pure thermally activated process (the data on hydrogen refer also to field-driven hydrogen movement). However, the assumption of "pure-thermal diffusion in bulk material" is not verified, as described in the following, and therefore the impurity responsible for devices degradation is not univocally identified.

As a result of these calculations, we have found that:

1. The process involved in the degradation mechanisms is ascribable to a diffusion one;
2. It is possible to evaluate the diffusion coefficient of the impurity involved in the degradation process;
3. However further work must be done to accurately identify which impurity is responsible for degradation (SIMS, C-V and DLTS analysis on specific test structures).

Diffusion layer	Diffusion width	Diffusion constant obtained from fitting
n-type	10 nm	1.610^{-19}
p-type	140 nm	710^{-19}

Table 3.2: Tabulation of diffusion obtained from fitting on LD E17.

Diffusive specie	D_0	E_a	A 85 °C	Reference
Hydrogen (H^+)	1.210^{-3}	1.23	5.910^{-21} cm^2s^{-1}	[10]
Hydrogen (H^+)	2.410^{-5}	0.96	7.4410^{-19} cm^2s^{-1}	[10]
Magnesium	1.910^{-12}	1.3	9.6710^{-31} cm^2s^{-1}	[41]
Si (with AlN layer)	6.510^{-11}	0.89	1.9510^{-23} cm^2s^{-1}	[42]
Si (without AlN layer)	9.110^{-11}	1.55	1.4110^{-29} cm^2s^{-1}	[42]
Si on p-GaN	1.010^{-7}	2.2	4.4110^{-38} cm^2s^{-1}	[43]
Nitrogen Vacancy	1.010^{-13}	4.1	2.0210^{-71} cm^2s^{-1}	[44]
Interstitial Gallium	1.010^{-13}	0.9	2.1710^{-26} cm^2s^{-1}	[44]

Table 3.3: Reference data of impurity diffusion that can be involved in LD degradation.

In the next sections, the dependence of degradation rate on the most important stress parameters will be analyzed. We will show that diffusion is not a pure-thermal effect, demonstrating that degradation is related to an electro-thermal migration of the impurity with the diffusion parameter calculated in this section.

3.3 Analysis of the effects of the operating conditions on LD degradation

The analysis of the effects of different driving conditions like: current, optical field and temperature on LD degradation has been the crucial point of the PhD work on LD reliability. As a matter of fact during the last years several authors have analyzed the degradation of InGaN-based LDs during constant current or constant optical power stress. It has been shown that stress determines the increase of the threshold current of the devices [33] [32] according to the square-root of the stress time [34]. Degradation has been ascribed to the worsening of the properties of the active layer, possibly due to point defects [25] and/or to modifications of the properties of the acceptor dopant [35]. The studies quoted above gave a significant improvement to the understanding of LDs degradation. However, they did not provide a detailed description of the role of the different driving forces in determining the failure of the devices. The aim of this section is to fill this gap, providing a characterization of the role of driving conditions in the degradation of the devices. By means of a set of stress tests carried out under different current, temperatures and optical field levels.

3.3.1 Purpose of operating condition dependent degradation

The aim of this section is to understand:

- if degradation process is thermally activated (as it should be if a diffusion process is involved), i.e. if an increase in stress temperature can determine an increase of the degradation rate;
- if degradation takes place also in a pure thermal stress (storage at high temperature with no bias applied to the junction);
- If the optical field play a role in determining/accelerating degradation kinetics;
- If the injected current play also a role in the observed degradation processes.

3.3.2 Definition of stress conditions

Samples have been aged under different stress conditions. Each stress test carried out within this work had a duration of 100 hours. For each set of stressed devices, we have keep constant one stress parameter (i.e. temperature, or OP level, or current level), and varied the other parameters, in order to understand how the individual parameter affect degradation kinetics. Details on stress conditions are listed in the following.

- Fixed optical power (65 mW), several stress temperatures
    - 65mW, 50°C
    - 65mW, 60°C
    - 65mW, 70°C
    - 65mW, 80°C

- Fixed temperature (70°C), several OP
    - 45mW, 70° C
    - 55mW, 70° C
    - 65mW, 70° C
    - 75mW, 70° C
- Fixed temperature (70° C), several current levels
    - 20mA, 70° C
    - 25mA, 70° C
    - 30mA, 70° C
    - 40mA, 70° C
    - 50mA, 70° C
    - 60mA, 70° C
    - 70mA, 70° C
    - 80mA, 70° C
- Fixed current (70° C), several temperature levels:
    - 70mA, 30° C
    - 70mA, 50° C
    - 70mA, 70° C
- Fixed high temperature (180° C), several current levels:
    - no bias, 180° C
    - no bias, 180° C

3.3.3 Effects of temperature

The first goal of this analysis was to analyze the role of temperature in determining the degradation rate of lasers aged at fixed optical power level (65 mW APC). Temperature is considered the major accelerating factor in solid state electronics degradation kinetics. A temperature greater than RT can be used to obtain accelerated stress analysis. It is therefore crucial to understand the activation energy of the degradation process. For this analysis, four devices have been stressed at the same OP level (65 mW) and different temperatures in the range 50-80 °C. As described in the previous section, threshold current increase and sub-threshold emission have similar kinetics during stress. For this reason, in this study we consider Ith as the parameter to be constantly monitored during stress. Results indicate that stress induces an increase of the threshold current of the devices proportional to the square root of time. Fig. 3.16 reports the plot of the several degradation kinetics obtained from different temperature stresses. as already described in the previous section. Fig. 3.16 (b) shows the same diagram in log-log scale. Straight lines are linear fittings of these degradation curves: as can be noticed, curves related to devices aged at different temperature levels have the same log-log slope (about 0.44, approximately square root of time), indicating that the I_th increase depends on a power (about 1/2) of stress time. Therefore, the degradation curves in Fig. 3.16 can be fitted according to:

$$I = I_0 + D\sqrt{t} \tag{3.7}$$

where the Degradation parameter (prefactor) D can be used as an expression of the degradation rate. Fig. 3.17 shows that this parameter depends on stress temperature, for the same optical power stress level, and this indicates that temperature plays a role in determining devices degradation. Note that the values of parameter D have been obtained by fitting the I_{th} degradation curves using 3.7.

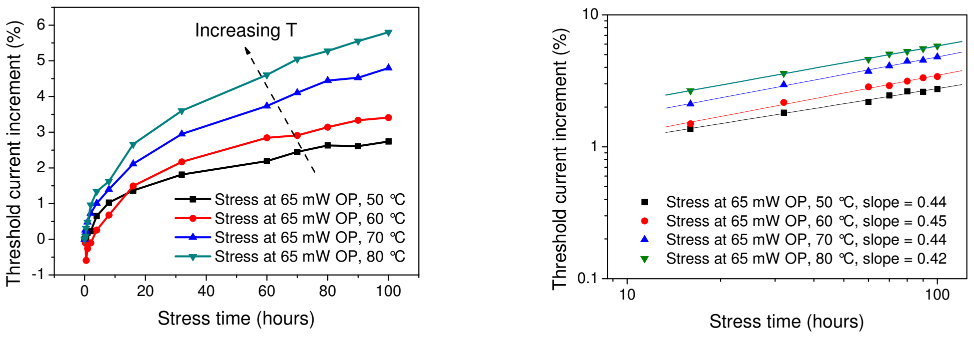

(a) (b)

Figure 3.16: Ith increase during ageing at different temperatures.

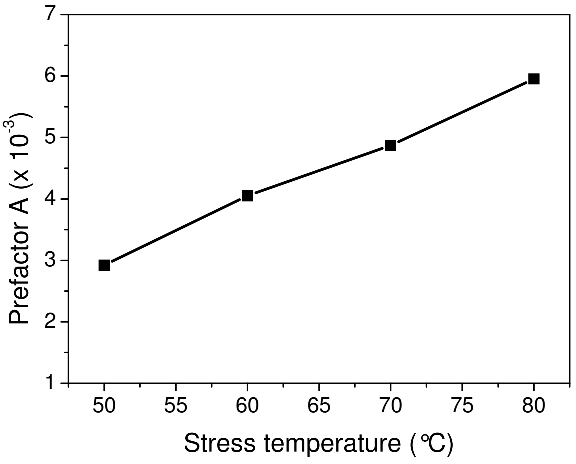

Figure 3.17: Prefactor D obtained from fitting after 100h of stress at different ageing temperatures.

To further study the effects of operating LD temperature stresses at fixed driving current and different temperatures have been performed. Anticipating the next section, it has been discovered that the effects of Optical Field is not to be considered as the major degradation cause. Therefore since in the previous stresses OP was constant but driving current was varying with temperature (increasing with temperature, and approximately with a swing from 72 to 85 mA) cannot be considered accurate enough for a detailed study. For further details on temperature effects on degradation it is therefore necessary to keep driving current constant. Results, presented in Fig. 3.18 indicate that increasing the temperature from 30 to 70 ° C has the effect to increase the degradation rate.

After 100h the degradation increased from 2.7% to 4% .

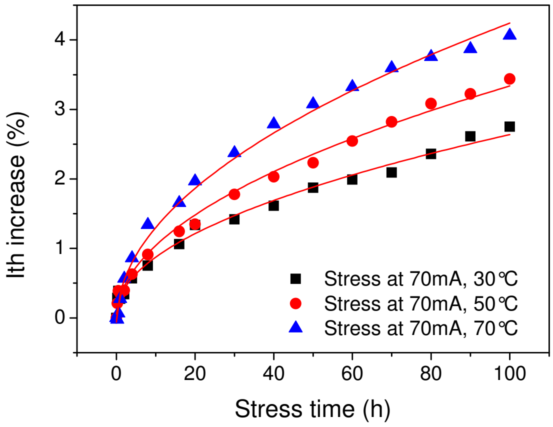

Figure 3.18: I_{th} increase kinetics from stresses at fixed current level and different ageing temperatures.

To quantify the effects of temperature on LD degradation kinetic it is possible to extrapolate the activation energy from the graph presented in Fig. 3.18. The Arrhenius plot has been caluclated evaluating the time to failure at 2.5% increase of the threshold current for the three different ageing temperatures. Results are presented in Fig. 3.19. The degradation process was found to have an activation energy of Ea = 250 meV (failure criterion = 2.5 % increase in Ith during stress at 70 mA). This value is similar to the 0.32 eV reported by Ikeda et al. [45] and Asano et al. [46] while the samples analyzed by Nakamura [47] and Kneissl et al. [30] demonstrated a slightly higher activation energy (0.5 eV). The low value of the activation energy found indicates that an increase in operating temperature determines only a limited increase in the degradation rate.

To better understand the role of temperature in determining devices degradation, we have also carried out stress tests at a high temperature (180 °C). These stress has been carried out inside an oven with no bias, in order to understand if temperature alone is able to induce degradation on LD devices with no applied bias. As a result, we have found that pure thermal storage (no applied bias) does not induce a significant degradation of the characteristics of the LDs (see Fig. 3.20), even for high stress temperature levels. Analyzing the obtained results it is possible to observe that:

1. Temperature alone does not induce a strong degradation (see Fig. 3.20 (b));

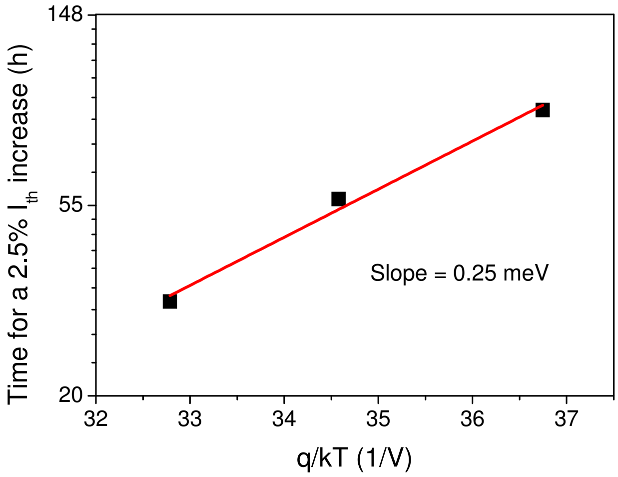

Figure 3.19: Arrhenius plot for the Time to failure at 2.5% of I_{th} at different temperatures.

2. No decrease of OP_sub is observed in comparison with current activated degradation Fig. 3.21 (a);

3. The degradation has a different kinetic from the one produced by LD stressed with current flow, Fig. 3.21 (b).

Therefore we can conclude that current and/or optical field are expected to play a key role in determining the Ith degradation, while temperature alone does not induce a strong degradation and only acts as an accelerating factor.

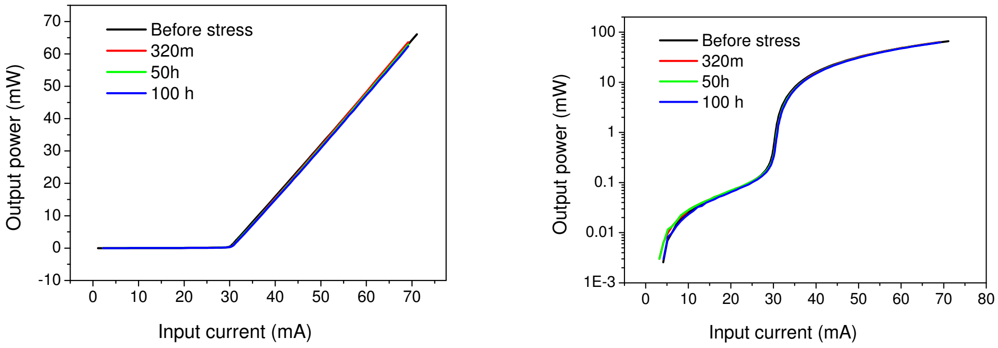

(a) (b)

Figure 3.20: L-I measurement (a) in linear and (b) in lig scale during ageing of sample X01 stressed at 180°C with no bias.

3.3.4 Role of Optical Field

The effects of optical field has been analyzed by means of APC stressed, where the OP emitted from the device has been measured by means of a photodiode and driving current has been adjusted to keep OP constant. The impact of stress at different optical

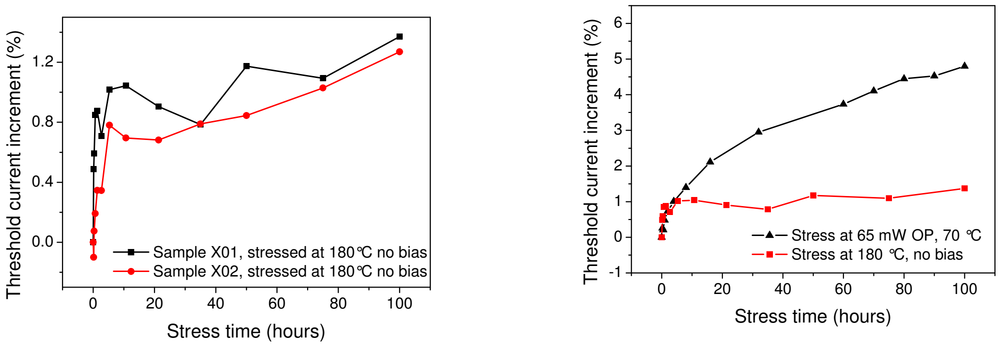

(a) (b)

Figure 3.21: I_{th} kinetics of (a) pure thermal stress, (b) compared to current activated stress.

power levels (in the range 45-75 mW), for the same temperature level (70 °C), with the aim of understanding if optical field plays a significant role in determining degradation rate. The OP range used for this analysis has been selected in order to reduce the differences in forward current during between the stressed LDs. Results are shown in the following.

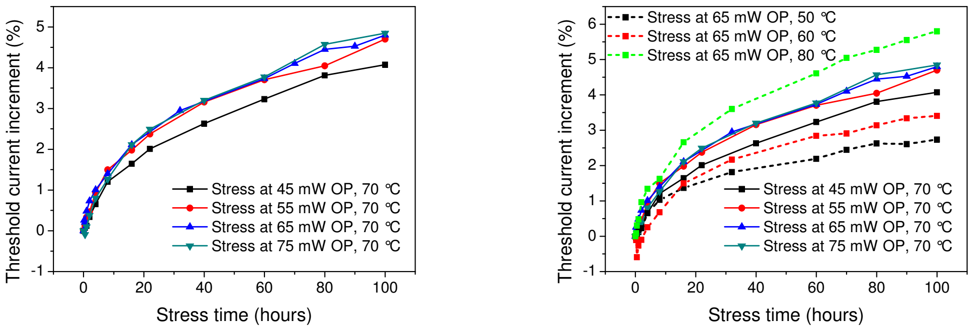

(a) (b)

Figure 3.22: I_{th} kinetics of (a) stress at different OP, (b) compared to temperature activated stress.

As can be noticed, increasing stress OP level did not imply a significant increase of degradation rate (see Fig. 3.22). The variation due to an increase of optical field was significantly lower than what determined by an increase of operating temperature. This fact is expressed by Figure 20, that shows the threshold current increase measured on both (i)samples aged at constant OP level (65 mW), different temperatures (50-80 °C) and (ii) samples aged at fixed temperature (70 °C), different OP levels (45-75 mW). This result indicates that degradation rate is not strongly related to optical power level, and that above threshold the variations of the optical field have only a minor impact on degradation kinetics. In order to achieve a more quantitative description of the dependence of degradation rate (prefactor D in (3.7)) on optical field, we have fitted the Ith degradation curves according to (3.7). Results are shown in Fig. 3.23, that shows the variation of degradation rate as a consequence of (i) a temperature increase (for stress at fixed OP level) and (ii) an optical power increase (for stress at fixed temperature level). Once again, it is confirmed that significant modifications of the degradation rate can be obtained increasing operating temperature, while a variation in optical power (keeping constant the device operating temperature) has only minor effects.

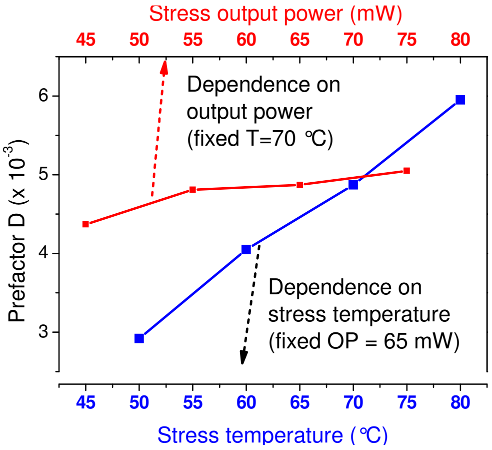

Figure 3.23: Dependance of I_{th} increase as a function of OP and temperature .

3.3.5 Effects of Driving Current

The results described above indicate that devices degradation is related to a diffusion process. This process is not purely thermally-activated, since it is necessary to apply bias to the devices to have a significant degradation. Furthermore, it has been shown that increasing junction temperature is an effective way to accelerate LDs degradation, even for the same optical power level. On the other hand, pure thermal stress (high temperatures, no bias applied to the lasers) was found to induce only a slight increase of threshold current. Therefore, optical degradation of the LDs can be attributed to an electro-thermal migration effect. In order to understand which is the role of carrier flow in determining degradation kinetics, and which is the relation between stress current and degradation rate, we have carried out stress tests at fixed temperature level (70 °C) and several input current levels (20, 25, 30, 40, 50 ,60 70 mA ACC). Results are shown in the following. In particular, Fig. 3.24 shows the threshold current increase measured on the devices aged at different current levels, for the same temperature (70 °C). The increase of stress current implies the increase of the degradation rate, as shown also in Fig. 3.25. For Istress<40 mA, prefactor D (see eqn. 3.7) the degradation rate is quite limited and has a linear dependence on stress current level. This slope slightly decreases as stress current is increased above 40 mA, however showing a large degradation rate.

In Fig. 3.25 we also show the optical power vs input current (L-I) curve measured on one untreated sample at the stress temperature (70 °C). It is easily recognizable that at 70 °C the lasing threshold is 40 mA: this is exactly the current level that determines

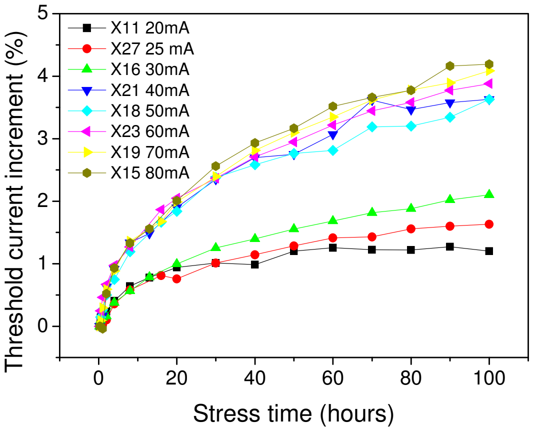

Figure 3.24: Dependance of I_{th} increase for LD aged at different driving current and 70° C.

the change of the slope of the prefactor D vs stress current curve. We think that the decrease of the slope of this diagram can be ascribed to the fact that:

1. above threshold carriers density is saturated, and therefore an increase in injected carrier does not imply a strong increase of degradation rate (in the case that the degradation is proportional to carriers density);

2. the degradation starts from native defects, and therefore at high current levels degradation rate can be limited by the concentration of already existing defects (this explanation however is less probable, since we do not observe a real saturation);

3. above threshold, the important optical field in the cavity can vary degradation process kinetics, above threshold much of the injected electrical power is converted in optical output, thus reducing the ratio of joule effect heating.

Results described in this section confirm the important role of driving current in determining the degradation of the properties of the lasers. In particular, it is shown that even under lasing threshold (I<40 mA), i.e. for low optical field, ACC stress can induce devices degradation. The dependence of the degradation rate on stress temperature is roughly linear: this can be explained considering current as a driving force for devices degradation, and carrier flow-induced defects generation as the physical process behind degradation.

3.3.6 Summary of activation parameters

To summarize the results, the degradation prefactor D has been plotted as a function of the three different ageing parameters analyzed in the previous sections: temperatures, optical field and current.

Fig. 3.26 shows that the degradation rate has a significant dependence on stress current and temperature levels; the mechanism responsible for LD degradation is therefore assumed to be electrothermally activated. The activation energy of temperature

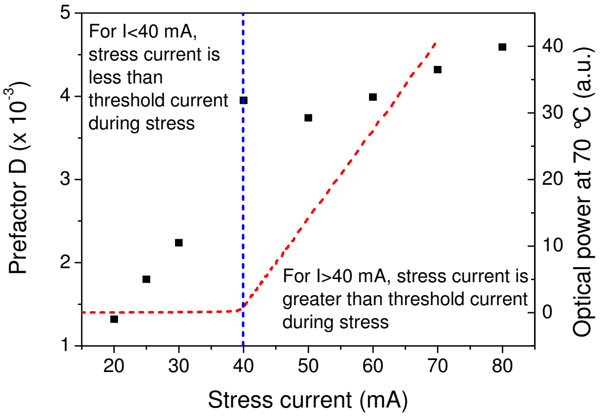

Figure 3.25: Correlation between Degradation prefactor D and ageing current. All measurement are performed at 70 °C, the blue line correspond to threshold current at ageing temperature.

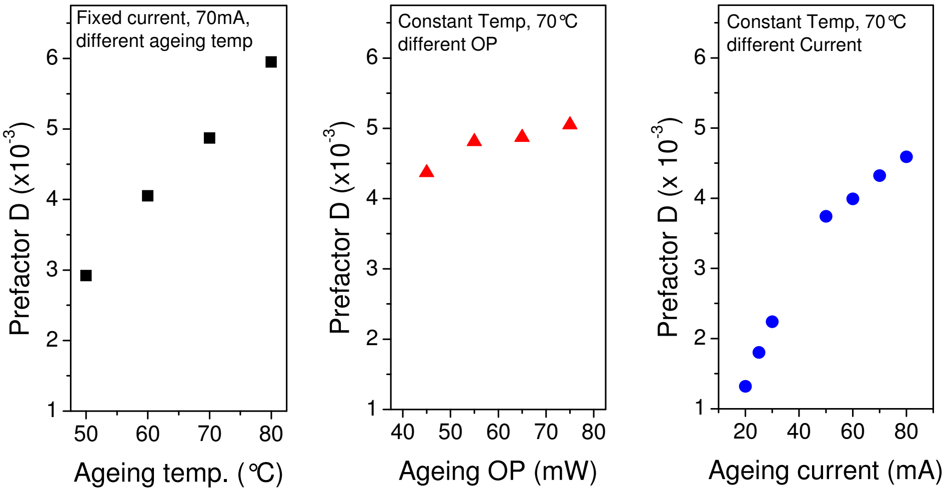

Figure 3.26: Correlation between Degradation prefactor D differing ageing driving forces: temperature, optical power and Current

in the case of an electrically biased device has been calculated in 0.250 meV. To obtain a significant degradation it is necessary that the devices are positively biased; pure thermal stress (high temperature, no bias) does not induce significant increase in the threshold current of the LDs. Finally it has been demonstrated that the effects of the Optical field is limited in the degradation kinetics.

3.4 Study of the non radiative lifetime during long term LD degradation

With the results presented in the previous section it has been demonstrated that degradation is related to an electro-thermally activated phenomena. Studying the correlation between threshold current increase and optical power in the subthreshold region during degradation, the hypothesis that non radiative lifetime change possibly related to an impurity diffusion phenomena has been formulated. On the other hand, only a slight decrease in the slope efficiency (SE) of the LDs was detected after stress (-5 %). This result suggests that stress induced only a limited variation in the mirror and internal losses and in the carrier injection efficiency [40] [33] [36] [26]. In fact, SE can be expressed as:

$$SE \approx \eta_{inj}\alpha_m/(\alpha_i + \alpha_m) \tag{3.8}$$

where η_i represents the carrier injection efficiency, and α_i and α_m represent the internal and mirror losses, respectively [40].

To defend this hypothesis a more detailed analysis has been carried out to extrapolate the non radiative lifetime during long term ageing of LD in different conditions. To determine the physical mechanism responsible for the threshold current increase, we have developed a method for the extensive analysis of the LŰI curves of the devices. According to the technique proposed in [48] , it is possible to evaluate the non-radiative recombination lifetime τ_{nr} by a detailed analysis of the LŰI curves of the devices in the subthreshold region.

3.4.1 Experimental Details and non radiative lifetime extrapolation theory

Several LD have been stressed at different driving currents in the range of 40-100mA and at the fixed case temperature of 75°C. The current has been considered, as previously described, the main degradation force involved in LD degradation. A method described by C. Van Opdorp [48] has been used in order to estimate the non radiative lifetime (τ_{nr}) of the devices. This method can be applied on packaged devices, contrarily to conventional methods based on Time-Resolved PL measurements. For this reason, this method is optimal for the investigation of material properties during ageing.

Considering the current flowing through the device splitted a leakage term (I_{leak}) and a recombination (I_{rec}) term we can write:

$$I = I_{Leak} + I_{Rec} \tag{3.9}$$

We can therefore introduce the injection efficiency, or the ratio between the recombination current I_{rec} and the total current entering the device I:

$$\eta inj = \frac{I_{Rec}}{I} \tag{3.10}$$

Considering then electron and hole densities comparable inside the QWs we will obtain $n = p$, therefore the recombination term in the subthreshold region, where almost only spontaneous emission occurs, is a third order polynomial accounting for radiative (An), non radiative (Bn^2) and Auger recombination (Cn^3) [5]. It can be expressed as:

$$I_{Rec} = qV\left(An + Bn^2 + Cn^3\right) \tag{3.11}$$

Where q is the electron charge and V is the active region volume. Examining the third term and considering that Auger term C is in the order of 10-30 cm6/s [49] while n^3 is still moderate being our analysis focused on low densities currents (the following analysis is carrier out in the sub-threshold region); we can conclude that Cn^3 term can be considered negligible with respect to An and Bn^2. The non radiative Einstein constant A can also be expressed as the inverse of the non radiative recombination lifetime τ_{nr}. Expliciting the above mentioned terms we obtain:

$$\frac{I_{Rec}}{q} = \frac{I\eta_{inj}}{q} = V\left(An + Bn^2\right) = V\left(\frac{1}{\tau_{nr}}n + Bn^2\right) \tag{3.12}$$

To continue the analysis it is necessary to consider the extraction of photon from the QW region in order to correlate the output optical power with the injected current. This can be easily accomplished defining the following variables and using as reference fig. 3.27:

- η_{ext} : external efficiency, number of extracted photons for carrier entering the device $\left(\frac{P_{out}/h\nu}{I/q}\right)$;
- $h\nu$ energy of the emitted photon;
- $P_{int} = VBn^2$: internal optical power in the QW region
- P_{out} : output emitted optical power;
- $E = P_{out}/P_{int}$: extraction efficiency

Combining the eqn (3.11) with the previous definition,and considering that:

$$\frac{1}{\eta_{int}} = \frac{I/q}{P_{int}/(h\nu)} = \frac{1}{\eta_{inj}} + \frac{1}{\eta_{inj}B\tau_{nr}n} \tag{3.13}$$

it is possible to obtain the following equation:

$$\frac{1}{\eta_{ext}} = \frac{1}{E\eta_{inj}} + \frac{1}{\tau_{nr}\eta_{inj}}\sqrt{\frac{V}{EB}}\sqrt{\frac{h\nu}{P_{out}}} \tag{3.14}$$

Equation 3.14 is the pivot of the analysis carried out in this section. As a matter of fact by means of 3.14 it is possible to extrapolate the non radiative lifetime τ_{nr}.

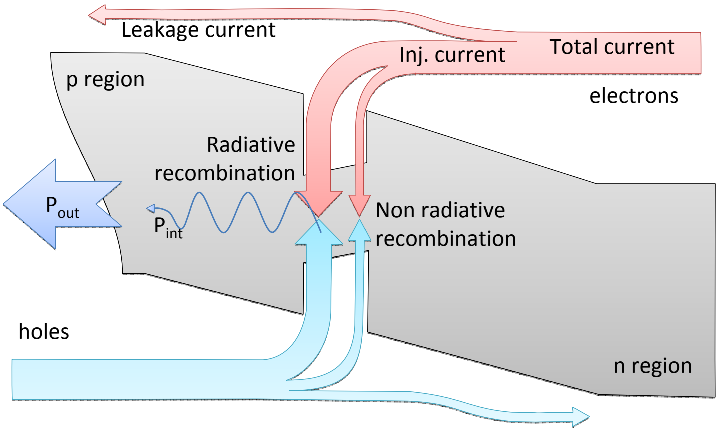

Figure 3.27: Schematic representation of carrier flow distribution and optical field in the LD structure.

It sufficient to plot $1/\eta_{ext}$ versus $\sqrt{h\nu/P_out}$, the slope of such a graph, that in the following will be referred as "$1/\eta_{ext}$ plot" is proportional to the non radiative recombination lifetime. The plot can be drawn from an high resolution L-I measurement of the sub-threshold region of a LD. To obtain these plots it is necessary to perform an high resolution measurement at low current densities. Thus the measurement setup used is based on an HP4155A semiconductor parameter analyzer and a large area high sensitivity photodiode. To ensure repeatability and avoid self heating the devices, during measurement, have been housed in thermo-controlled fixture at a constant current of 25°C. An example of the measurement and relative $1/\eta_ext$ plot of an LD is reported

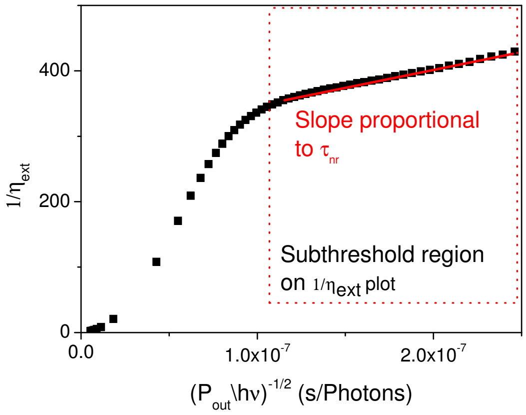

Figure 3.28: $1/\eta_{ext}$ plot of an LD, the plot report the subthreshold region, and the relative slope porportional to τ_{nr}.

in Fig. 3.28; the area in the subthreshold region of the LD is the one considered for this analysis and is enlightened in the plot. From this area, as described above, it is possible to extrapolate the non radiative lifetime τ_{nr} calculating the slope with a linear fit. The intercept on the y axis is instead proportional to the first addendum of the last term of equation 3.14.

The straight line indicates that the model of vanOdorp and Śt Hooft can be effectively applied to InGaN-based LDs, as previously demonstrated for AlGaAs-based LDs. The measurement described above will in the following be compared with the LD threshold current measured with a similar setup. The values of τ_{nr} estimated by the method proposed in this work are in the range 5Ũ20 ns, and these results are consistent with previous studies [50]. It is worth noticing that the two measurements of these parameters are not correlated, as a matter of fact, they are performed in different LD working regions, involving different physical mechanisms (i.e. spontaneous and stimulated recombination).

3.4.2 Results

As presented in Fig. 3.29 the degradation kinetic of the LD after a long term stress (2000h) confirms the square root of time behavior of the threshold current, thus confirming the hypothesis that the degradation is related to a diffusion process. Results also indicate a clear effect of the ageing current on the degradation kinetic: no change in the degradation shape is detected, while the ageing current has a substantial impact on the degradation prefactor D (see as reference equation 3.6).

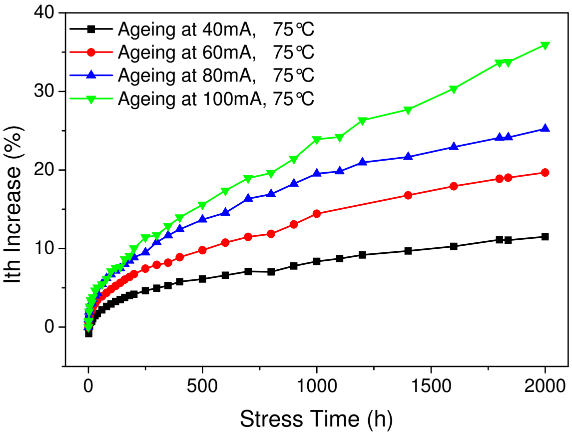

Figure 3.29: Threshold current kinetic of LD stressed at different ageing currents.

The results obtained from non-radiative recombination lifetime extrapolation (referring to eqn. 3.14) are presented in Fig. 3.28. As shown, the slope of the straight line below threshold increases after ageing, suggesting that stress induces the decrease in τ_{nr}. The obtained result reveals that the density of defects working as NRCs does increase during ageing. Fig. 3.28 also shows that the y intercept of the straight line increases, which points to a decrease in extraction efficiency after ageing as discussed above.

Different current driving conditions are compared. A clear decrease in τ_{nr} during stress is observable. The kinetics are similar to those of Fig. 3.29 sustaining the hypothesis that the Ith and τ_{nr} physics mechanisms are correlated.

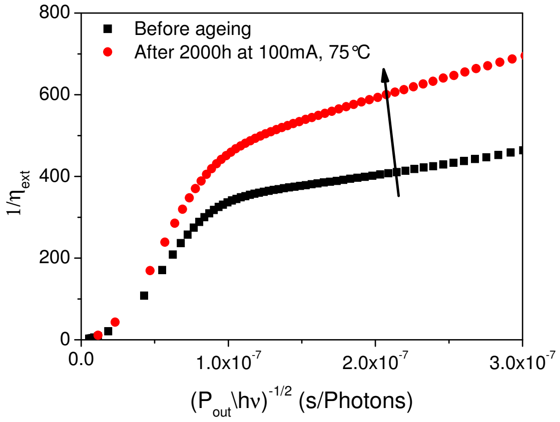

Figure 3.30: $1/\eta_{ext}$ plot of an LD before and after ageing the blue lines represent the sub-threshold region area.

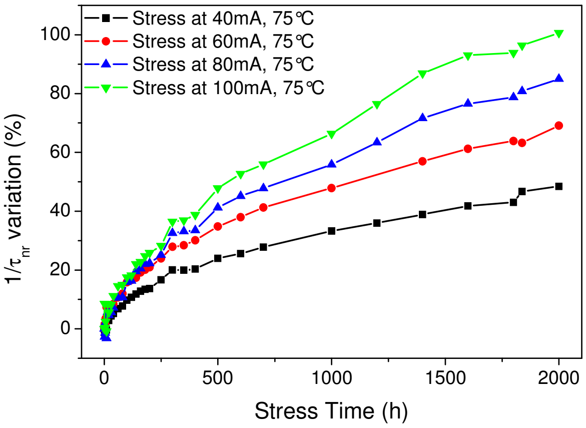

Figure 3.31: Threshold current kinetic of LD stressed at different ageing currents.

The correlation of τ_{nr} and I_{th} supports the hypothesis of non-radiative lifetime increase to be responsible for device degradation, this result can easily be explained since it is possible to express the threshold condition as [40]:

$$I_{th} \approx n_{th} \left(A + B n_{th} \right) \tag{3.15}$$

Describing the dependence of the threshold current on the non-radiative recombination rate A and on the radiative recombination rate B. As can be understood, an increase in the nonradiative recombination rate can induce an increase in the threshold current of the devices.

To provide a more detailed description of the correlation between the variation of these two parameters, in Fig. 3.32, we have plotted the variation of the nonradiative recombination rate $A = 1/\tau_{nr}$ versus the increase in I_{th} measured at each stage of the stress tests. This diagram indicates a linear correlation between the variation of the two parameters.

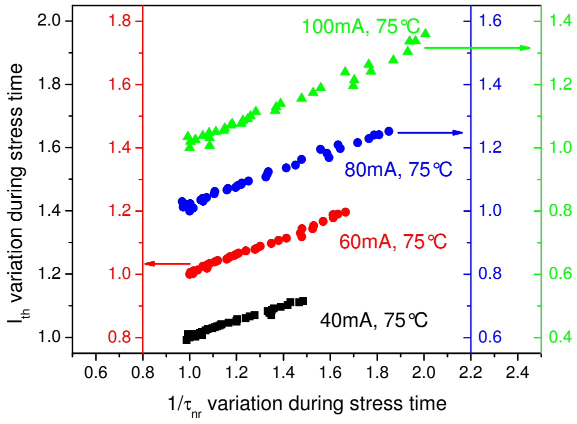

Figure 3.32: Correlation between $1/\tau_{nr}$ and I_{th} for different currents.

To verify the correlation between the I_{th} increase and the t_{nr} decrease a wide current stress range has been adopted and to understand how the stress current level can influence the degradation kinetics, we have stressed a set of devices at different current levels (in the range between 4.4 kA/cm^2 to 11.1 kA/cm^2, close to the lasing threshold, and 11.1 kA/cm^2, close to the nominal operating conditions). The results are summarized in Fig. 3.32, which shows the decrease in the non-radiative recombination lifetime measured during stress at four different current levels: a higher stress current level determines a more prominent decrease of τ_{nr}. The plot describes the correlation between the threshold current increase (on the horizontal axis) and the increase in the non-radiative recombination rate A (on the vertical axis) measured on a set of samples aged at different current levels for 2000 h. Every dot is the correlation at a different ageing time. In order to make the graph clear the four y axis has been shifted one with respect to the other. Moreover, observing that the slope of the I_{th} - $1/\tau_{nr}$ correlation does not change slope for different temperatures, it can be concluded that the degradation mechanism is the same for the different current operating conditions. From the plot of Fig. 3.33 the degradation of LD is therefore strictly correlated to the increase of the non-radiative recombination for a wide range of ageing currents.

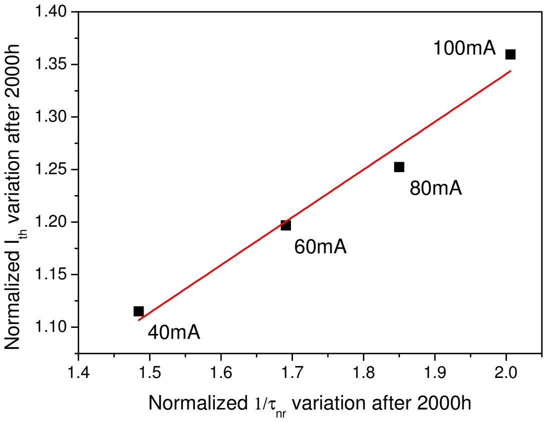

Figure 3.33: Linearity of degradation parameters as a function of stress current level.

The almost linear dependence between the two parameters confirms the important correlation between the increase in the non-radiative recombination rate and the threshold current increase. Finally Fig. 3.33 demonstrate that the entity of the degradation has a linear dependence on the stress current level: this result confirms that current plays a significant role in determining the degradation of the LDs.

On the other hand, since 1) the activation energy of the degradation process is quite low (0.25 eV) and 2) increasing the stress current from 4.4 to 11.1 kA/cm^2 determines only a limited increase (15 ° C) in the junction temperature, temperature is thought to play only a limited role in determining the variation of the degradation kinetics.

Chapter 4

Reliability of InGaN LED-like samples

This chapter is strictly correlated to the previous one, by means of special LED-Like samples it has been possible to better study the effects of degradation on the epitaxial structure of LD devices. The effects of ageing have been studied on LD mainly by means of Optical measurements. Capacitance and Electrical measurements are to be considered affected by a structure issue: the aged region is in fact different from the measurement region. This can be easily explained with the gain guided carrier confinement mode, during degradation the LD are in lasing condition and the carriers are highly confined under the ridge region, while during measurement the injected carriers are several order of magnitude lower, thus spreading all over the QW region and not confined only under the ridge. In order to study the effect of degradation on the active region by means of electrical and capacitance measurement we need to actually stress all the region. This has been obtained with the so called LED-Like structures: a LED device with a p-contact area of 75x200 μm, the same epitaxial structure of the LD and no carrier confinement region.

4.1 Introduction

The aim of the work described in this section is to analyze the effects of stress at different driving currents on LED-LIKE devices. In this section we will show that a stress at a current of 600mA (with a temperature of 75 °C, current density = 4 kA/cm^2) can induce a significant decrease of LED optical output power. In particular, device degradation is more prominent at low measuring current densities. This result suggests that stress induces an increase in defect density that can determine an increase in non radiative recombination rate. The degradation kinetics have been found to be proportional to the square root of time. This is also compatible with the degradation kinetics of laser diode devices. The analysis of the electrical characteristics of the LED-LIKE devices indicated that stress can induce (i) a clear increase in leakage current and (ii) a sudden decrease in the generation/recombination (G/R) current components after the first stress step, followed by a gradual increase. The increase in G/R components detected after stress is strongly correlated to the decrease in optical power, as shown in detail in the following.

4.2 Experimental details

We have analyzed the electrical and optical behavior of LED-like devices during stress at different currents and temperatures. During stress, we have monitored the variation of the optical power vs current (L-I) curves, of the current vs voltage (I-V) curves and capacitance versus voltage and frequency. The stresses have been initially carried out using our LDC3916 laser driver, that has been stopped at fixed time intervals for the evaluation of the parameters of the devices. However, we have observed that the maximum current levels that can be reached by our LD driver (500 mA) is not sufficient to induce a significant degradation of the LED-LIKE devices: therefore, we have decided to carry out the stress tests by means of a Keithley 2612 Source-meter (capable of up to 1.5A). In order to achieve a good evaluation of the stress kinetics, two devices (devices L20 and L24) were stressed without removing them from the fixture (good repeatability of the optical measurements). The optical parameters of device L20 were measured directly with the PD connected to a power meter. On the other hand, the optical characteristics of device L24 were measured by means of a spectrometer (Ocean Optics USB4000), in order to evaluate the spectral shift during device degradation. To increase accuracy, electrical an optical measurement of L20 and L24 has been performed at controlled temperature of 25 °C by means of TEC system. Even if we have stressed a number of samples under different conditions, in the following we will mostly refer to devices L20 and L24, since the degradation kinetics of these devices have been evaluated with high accuracy (in-situ stress, without removing the samples from the stress fixtures for the total duration of the experiments).

4.3 Results-Optical measurements

Fig. 4.1(a) and Figure 4.2(b) show the variation of LI curves during stress at 600mA, 75 ° C for devices L20 and L24 respectively. As can be noticed, stress induced a decrease in the optical power emitted by the devices. We have also normalized the LI measurements with respect to the initial values, in order to obtain the results presented in Figure 4.2(b) and 4.2(b) (these curves report the plot of P(t)/P(t=0), where P represents the optical power emitted by the devices). Plotting the variation of the optical power at a fixed current during degradation we obtain the plot reported in Fig. 7.6(a) and 7.8 (b)respectively for devices L20 and L24. As can be noticed, stress induced a decrease in optical power, which is more prominent when measured at low current levels. Plotting the inverse of the degradation (P(t=0)/P(t), where P represents the optical power emitted by the devices) we obtain picture 7.9 (a) and 7.9 (b). As can be noticed, the variation of P(t=0)/P(t) is proportional to the square root of time. This is confirmed by the log plot of Fig. 7.11(a) and 7.11(b) where the slope is ≈ 0.5 for different currents. The inverse of the degradation has been used in order to correlate the degradation of LED-like devices with previous experiments on laser diodes where the threshold current has been used to monitor degradation. The following consideration has been formulated considering the Auger term Cn^3 negligible. For the Laser Diodes we had considered the variation of I_{th} as a good estimator of the non radiative recombination, because it is proportional to the density of traps:

$$\frac{1}{\tau} = A + Bn \tag{4.1}$$

$$A = N_{trap}\nu_{th}\sigma \tag{4.2}$$

$$I_{th} \approx \frac{qV}{\eta_i \tau} n_{th} = \frac{qV}{\eta_i} \left(A + Bn_{th}\right) n_{th} \tag{4.3}$$

$$\Delta I_{th} \approx \frac{qV}{\eta_i} \delta A n_{th} \approx \Delta N_{trap} \tag{4.4}$$

In the case of LED-like we should consider the degradation as a decrease of efficiency, therefore we can state:

$$P_{out} \approx Bn^2 \tag{4.5}$$

$$I = \frac{qV}{\eta_i} \left(An + Bn^2\right) \tag{4.6}$$

$$\eta_{ext} \approx \frac{P_{out}}{I} \approx \frac{Bn^2}{An + Bn^2} \tag{4.7}$$

$$\frac{1}{\eta_{ext}} \approx \frac{An + Bn^2}{Bn^2} = \frac{A}{Bn} + 1 \tag{4.8}$$

Therefore (if the product Bn is not changing as a consequence of stress) it is reasonable to think that the inverse of the degradation rate is proportional to the non-radiative recombination rate, as already demonstrated for the laser diodes. As stated above, we have stressed several devices at different current/temperature levels: devices L20 and L24, stressed at high current densities, showed a significant degradation, as reported above. On the other hand, devices stressed at lower current densities showed no strong optical degradation. However, observing the relative output power at different stress steps using a semilog scale for the current axis, a clear decrease of the OP is noticeable in the low current region. This has to be related with the increase in non-radiative recombination. Several observation can be given:

- The degradation of the LED-like samples has a square-root dependence on stress time, and this result is in agreement with previous findings on laser diodes (degradation related to a diffusion process),

- The degradation is more prominent at low measuring current levels. This result suggests that stress induces an increase in the non-radiative recombination in the active layer of the devices,

- Degradation is electrically activated. A significant degradation can be achieved only for stress current densities greater than $3-4kA/cm^2$(comparable to the stress current densities used for the laser diodes).

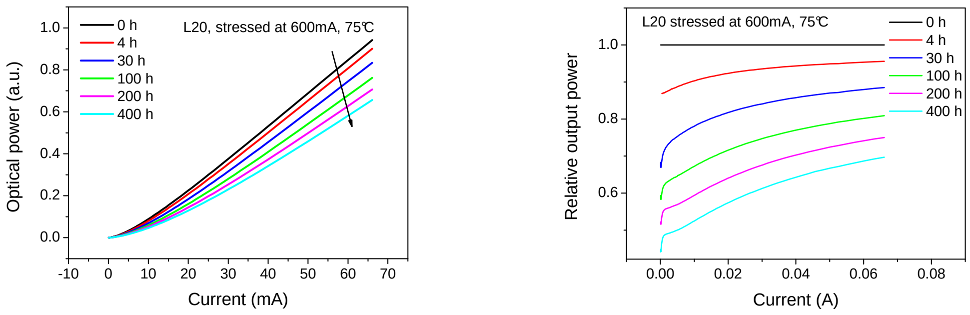

(a) (b)

Figure 4.1: (a) L20 and (b) L24 Optical power Vs Current measurement during device degradation L20 Optical power Vs Current measurement during device degradation.

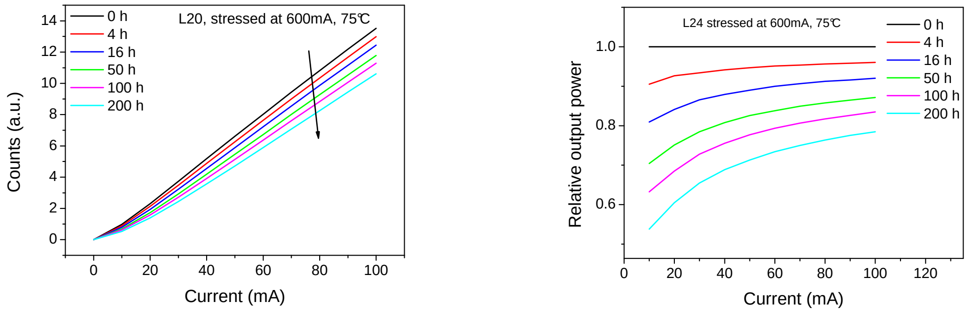

(a) (b)

Figure 4.2: (a) L20 and (b) L24 relative OP variation during device degradation at different current.

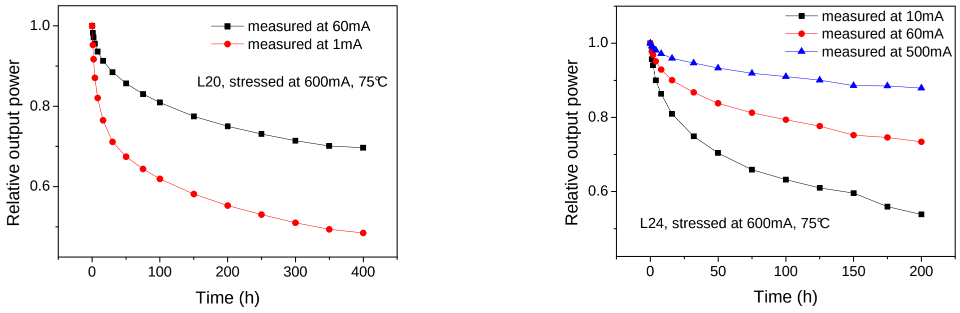

(a) (b)

Figure 4.3: (a) L20 and (b) L24 OP decrease during device degradation.

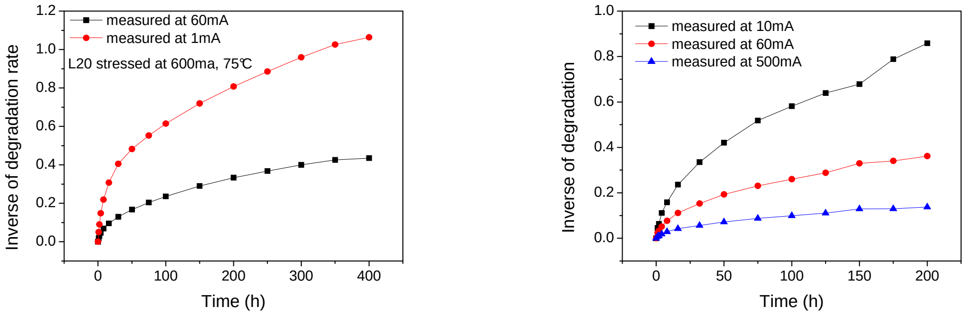

(a) (b)

Figure 4.4: (a) L20 and (b) L24 inverse of degradation during device lifetime.

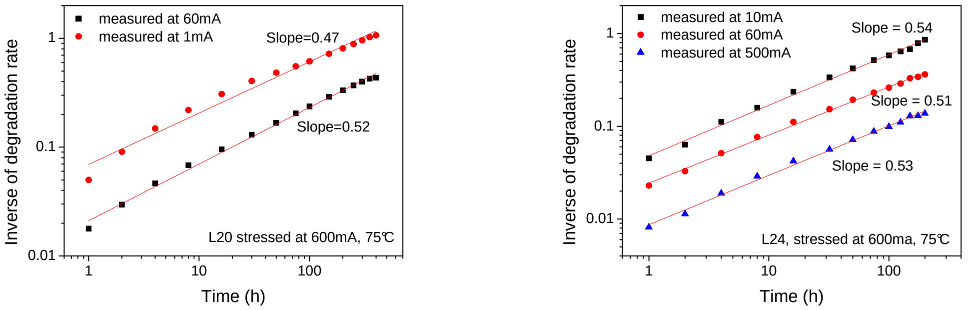

(a) (b)

Figure 4.5: (a) L20 and (b) L24 Log-Plot of OP decrease vs stress time.

4.4 Results-Electrical measurements

In fig. 4.6 we report the results of the electrical measurements carried out on devices L20 and L24 during stress time. Results indicate that stress induced a general increase in leakage current both for reverse and forward voltages, and significant variations in the generation/recombination current components. For both devices, we see that:

1. the first step of stress induced an abrupt decrease of the G/R current (evaluated at +2.6V, approximately in the center of G/R zone, as can be seen from fig. 4.6). This effect is very rapid, and can be related to an initial annealing of the active region/contact layers induced by the high density of flowing current. However, this steep decrease in device current is not correlated to significant modifications in the optical properties of the devices

2. After the initial decrease, the G/R current components of devices L20 and L24 suffered a gradual increase. This increase is significantly slower than the initial decrease. It has been monitored, by plotting the current at +2.6 V (where the G/R current is dominating) which is reported in Fig. 4.7 (a) and (b). As can be noticed, the generation/recombination current increases with the square-root of stress time (as we have found for the optical power decrease).

This result suggests that these variations in the electrical characteristics of the samples can be a signature of some modifications taking place in the active layer. In fig. 4.8 we report a plot of the inverse of OP decrease vs the variation in G/R current detected during stress. A correlation between the variation of the two parameters is found, and some consideration can be given, by considering that:

- The optical power decrease is related to an increase in the non-radiative recombination rate

- The optical power decrease is strongly correlated to modifications in the electrical characteristics of the samples (increase in G/R components)

- Both parameters vary with the square-root of stress time

These results suggest that stress can determine the increase in the non-radiative recombination rate, due to the generation/propagation of defects in the active layer of the samples. As a result, the G/R components of the LED-LIKE samples can show a certain increase. The results from stress performed at lower current densities are shown in fig. 4.10 and fig. 4.11; the plots report the relative output power at different stress times with respect to the initial OP for different driving currents (in log scale). As can be noticed a decrease of efficiency at low current level is detectable, thus confirming the hypothesis of non-radiative recombination rate increase. The results of stress on current voltage characteristic have been reported in Figures 4.11.

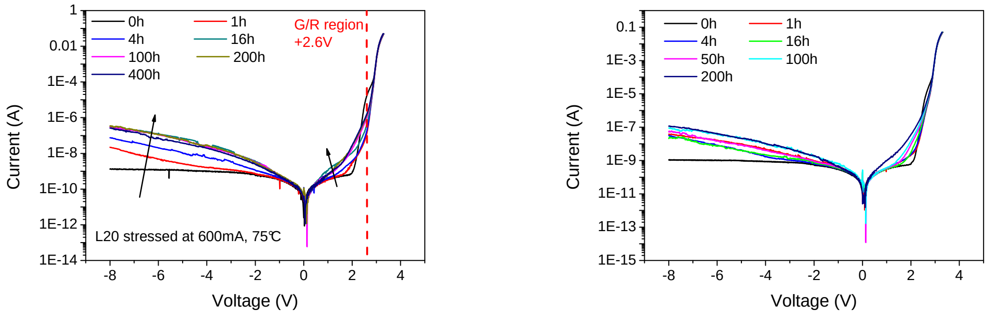

(a) (b)

Figure 4.6: (a) L20 and (b) L24 Electrical characteristic during device degradation.

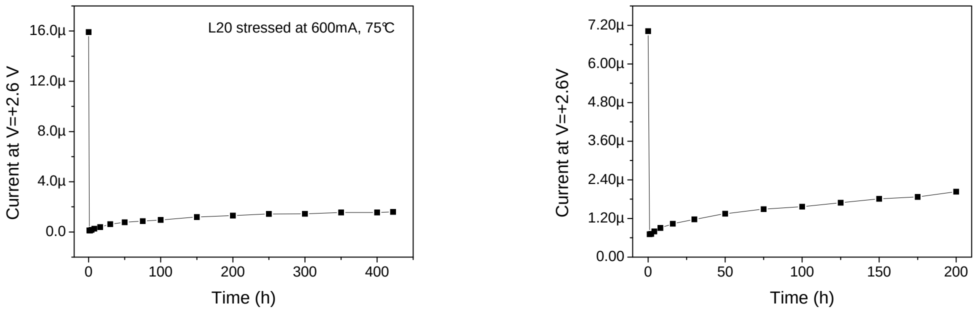

(a) (b)

Figure 4.7: (a) L20 and (b) L24 Kinetic of variation of current at 2.6V during device degradation

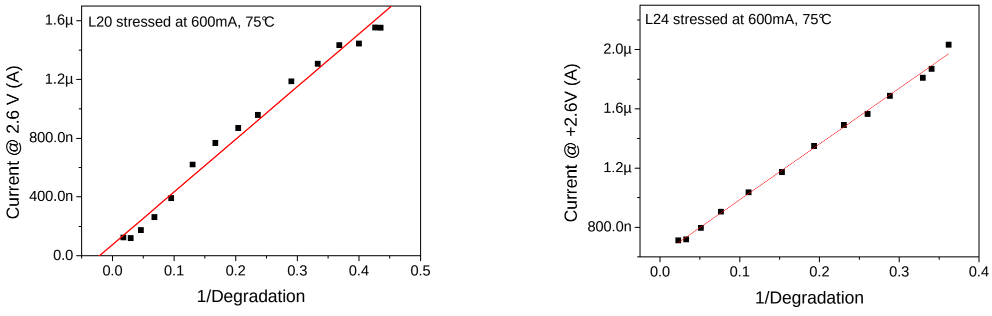

(a) (b)

Figure 4.8: (a) L20 and (b) L24 Correlation of OP decrease with increase of current at 2.6V.

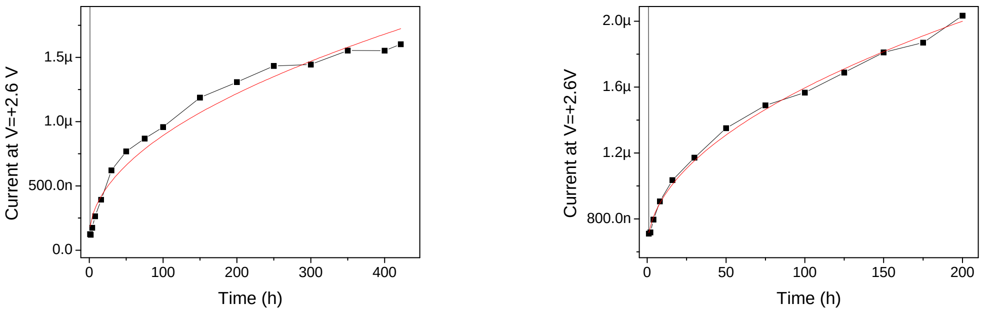

(a)

(b)

Figure 4.9: (a) L09 and (b) L10 Variation of G/R current at 2.6V with square root of time fitting.

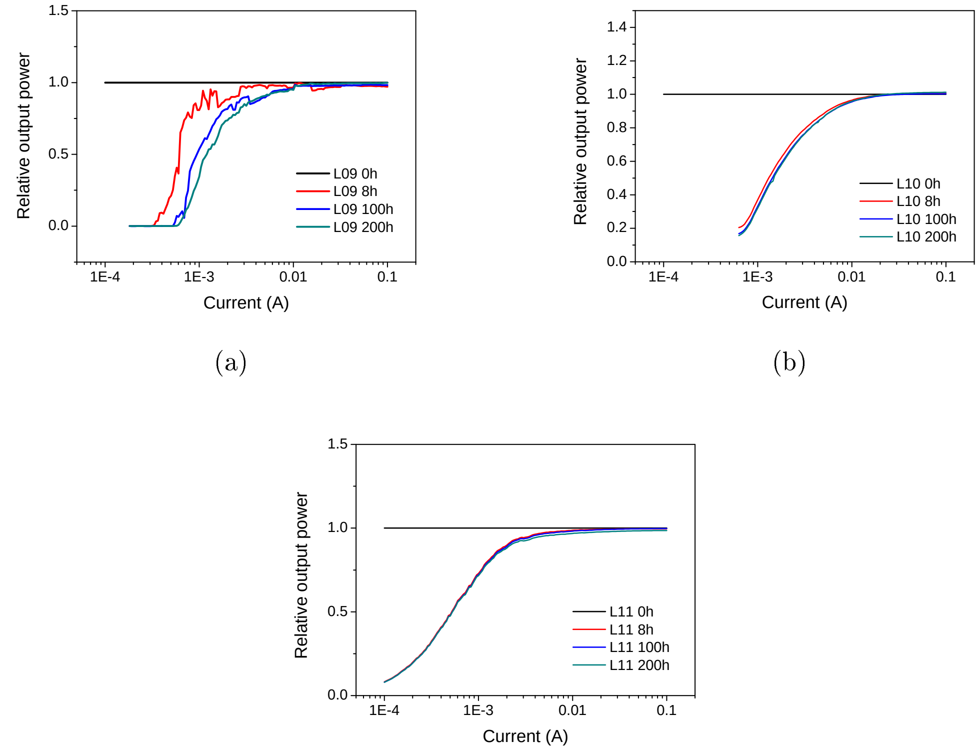

(a)

(b)

(c)

Figure 4.10: (a) L09, (b) L10 and (c) L11 relative OP variation during device degradation at different current.

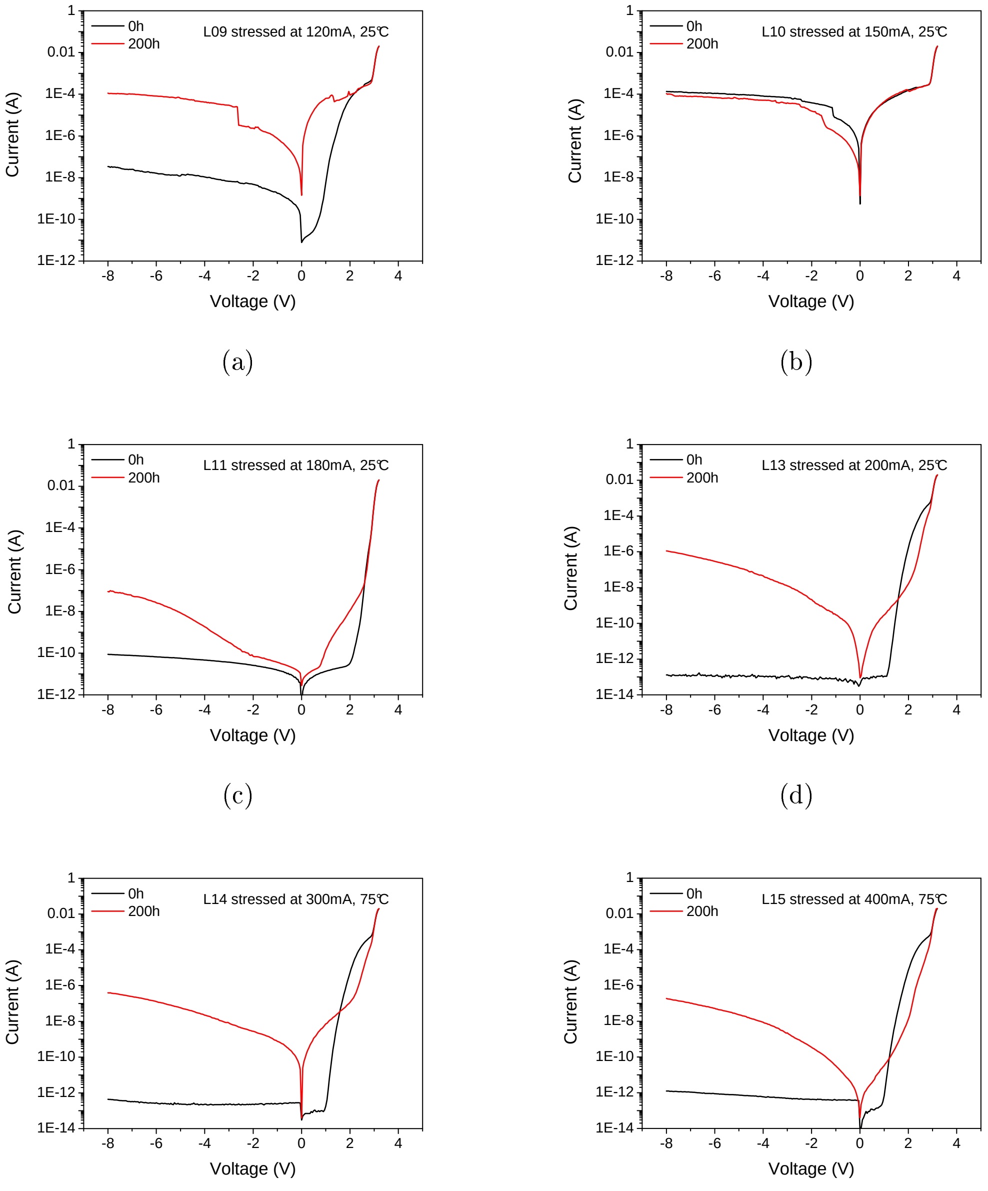

(a) (b)

(c) (d)

(e) (f)

Figure 4.11: (a) L09, (b) L10, (c) L11, (d) L13, (e) L14 and (f) L15 relative IV variation during degradation.

4.5 Analysis of the LED-like capacitance variation during degradation

4.5.1 Introduction

In this section we have analyzed the effects of stress on capacitance characteristics of the devices, in particular C-V measurement. Results indicate that:

1. After stress, C-V curves showed a shift of the maximum capacitance towards higher voltage levels. This phenomenon is probably related to the global decrease of G/R current of the devices in the forward polarization region (see Magenta arrow in Fig. 4.12))
2. The C-V curves of some of the devices show a significant (and semi-rigid) shift towards higher capacitance levels. This shift is visible in the whole analyzed voltage region (see blue arrows in Fig. 4.12)
3. Stress does not induce modifications in the apparent charge profile of the devices.

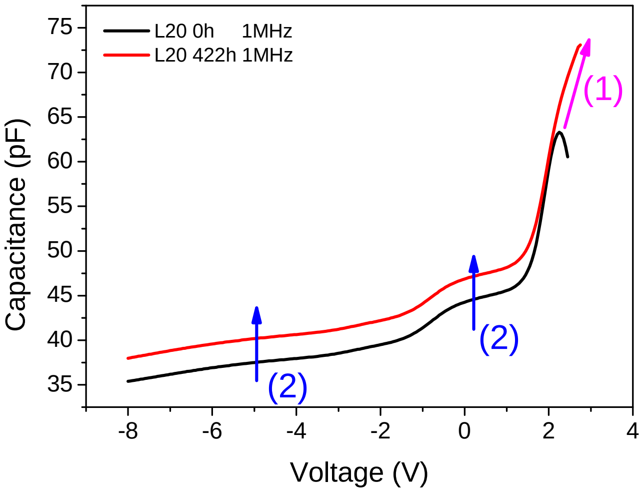

Figure 4.12: Illustration of effects of stress on capacitance characteristics.

4.5.2 Experimental details

All the capacitance measurement have been carried out by means of HP4284a LCR meter. Devices have been measured at room temperature. Measurements were carried out using the parallel Cp-Gp model, measurement have been performed in range -8V +2.8V at three frequencies: 300 Hz, 10 kHz, 1 MHz. C-V data were used for the extrapolation of the apparent charge profiles, using $\epsilon = 9.5$, and area=75 x 200 μm^2 as parameters. This procedure has an intrinsic approximation, since charge profiles are calculated under the assumption that one side of the junction (p) is heavily doped with respect to the other one (n). It is worth noticing that this assumption introduces an approximation in the determination of the apparent depths and levels, since the charge concentration at the p-side is not infinite, and the space charge region (SCR) extends both at the p and at the n side. Capacitance versus frequency measurements have also been performed with the same setup in frequency range of 100Hz - 1MHz at a voltage of 0V. C-f measurement are also coupled with conductance-frequency G-f measurement, in particular G/f vs f plot will allow us to evaluate the trap frequency peak response, as proposed by Barbolla et al. [1]. For the capacitance analysis L20 and L24 devices have only been measured before and after the stress and not during degradation because they have been subjected to automatic stress-measurement procedure in order to improve the repeatability of the electrical and optical measurements. The other devices have been subjected to C-V measurement after each stress test.

4.5.3 Results

Measurement performed at 10kHz - Results from C-V measurements performed at 10kHz on L20 and L24 before and after stress (422h and 200h respectively) showed no significant variations in the reverse bias region, while it can be detected an increase in capacitance in the high-voltage region ($V > 2$ V) for both devices. In particular after the stress the L20 and L24 C-V curves show an increase and a shift toward higher voltages of the maximum measured capacitance (Figure 27 and Figure 33). The maximum of the C-V curves (occurring at a critical voltage V_c close to 2 V before stress) represents the point where current conduction becomes significant, and inductive effects determine a sudden decrease of the measured capacitance value. Beyond the critical voltage V_c , the junction (depletion-related) capacitance cannot be measured anymore. After stress, we have measured an increase in the critical voltage V_c: this effect can be correlated to the fact that the initial steps of stress induced a decrease in the generation-recombination current components, with subsequent reduction of the parasitic inductive effects responsible for the decrease in measured capacitance beyond V_c. However, this effect seems not to be correlated to the decrease in the optical power emitted by the devices, and therefore cannot provide information on the degradation process. The charge density shows no substantial variation after the devices degradation (Figure 28 and 34). The effect detected in the C-V curve and already described is noticeable in the zone close to the junction (forward polarization region) were after the stress the extrapolated curve extends to higher carrier density values. It can also be noticed a certain dispersion of the apparent doping profile curve at 422h, related to the increase in the leakage current of the device in the reverse bias region thus affecting the measurement which result more noisy.

Measurement performed at 1MHz - L20 and L24 has also been measured before and after the stress at a frequency of 1MHz. Results show a global increase in the capacitance in the whole analyzed voltage range (Figure 29 and 35). This phenomenon is verified for both devices, but more evident for L20 which has been subjected to longer degradation experiment. The effect is noticeable also in the charge density vs. voltage plot (Figure 30 and 36) where an increase in apparent charge is detected after the degradation. The capacitance increase is almost constant at every voltage, as we can see from Figure 63 and Figure 64 where the device capacitance after the degradation has been shifted by a constant value and the obtained CV characteristic overlaps with the untreated device CV curve. The confirmation of the increase in The kinetic of this phenomenon is analyzed by means of device L15, which has been subjected to 400mA, 75°C stress. The kinetics reported in Figure 65 confirm the hypothesis of capacitance increase during degradation, even if the measurement is affected by some noise.

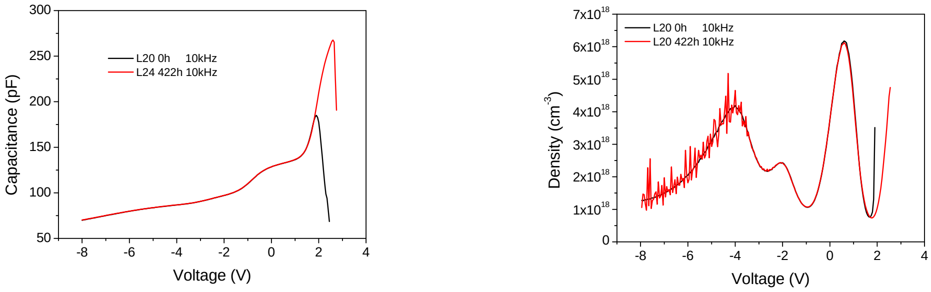

(a) (b)

Figure 4.13: (a) CV plot of L20 before and after degradation at 10kHz, (b) Apparent charge concentration in L20 before and after stress at 10kHz.

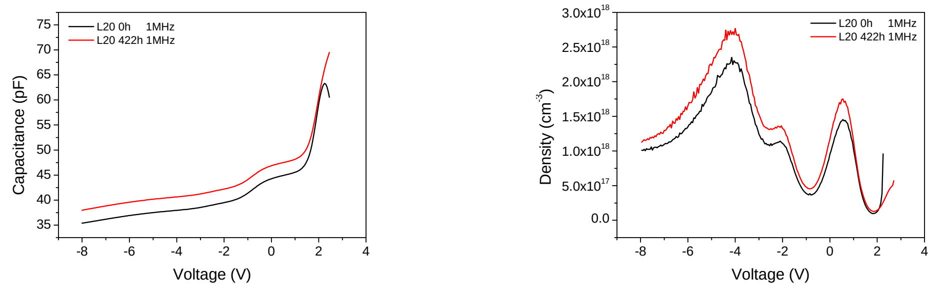

(a) (b)

Figure 4.14: (a) CV plot of L20 before and after degradation at 1MHz, (b) Apparent charge concentration in L20 before and after stress at 1MHz.

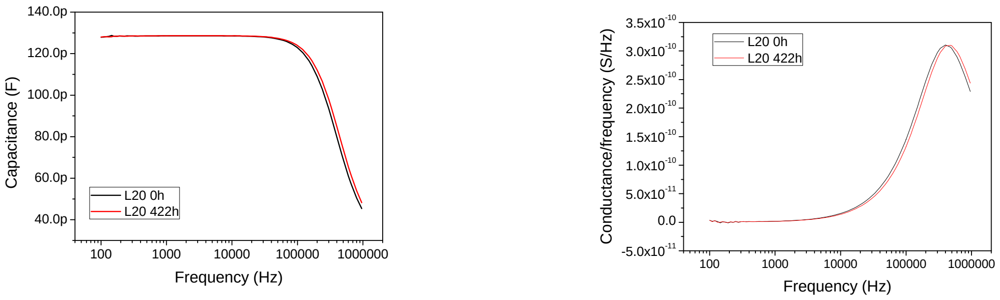

(a) (b)

Figure 4.15: (a) Cf plot of L20 before and after degradation, (b) G/f vs f plot of l20 before and after degradation.

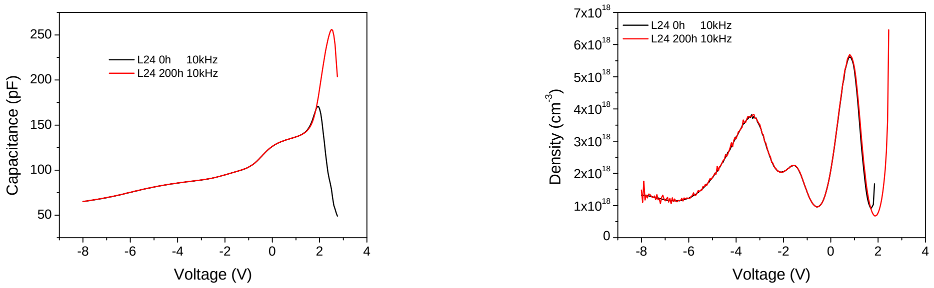

(a) (b)

Figure 4.16: (a) CV plot of L24 before and after degradation at 10kHz, (b) Apparent charge concentration in L24 before and after stress at 10kHz.

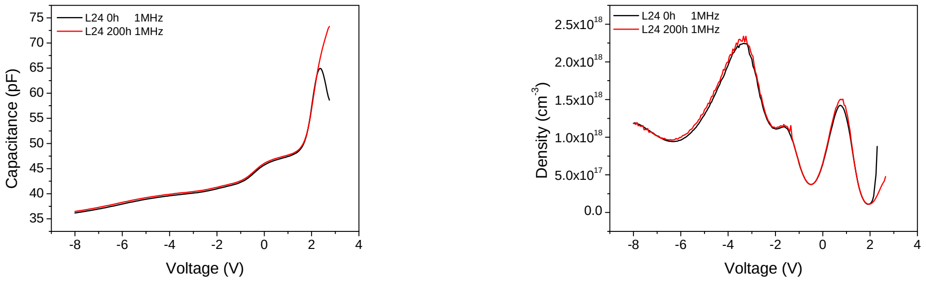

(a) (b)

Figure 4.17: (a) CV plot of L24 before and after degradation at 1MHz, (b) Apparent charge concentration in L24 before and after stress at 1MHz.

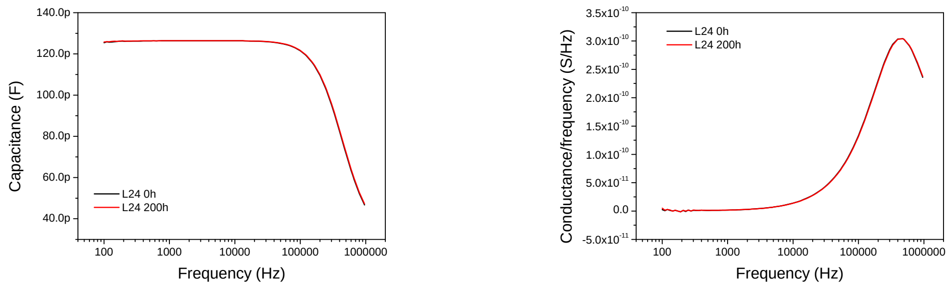

(a) (b)

Figure 4.18: (a) Cf plot of L20 before and after degradation, (b) G/f vs f plot of l20 before and after degradation.

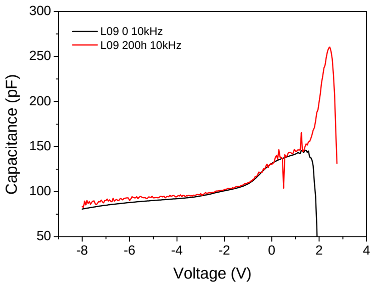

The Apparent charge concentration
in L09 at 10kHz is too noisy
To have any significance

(a) (b)

Figure 4.19: (a) CV plot of L09 before and after degradation at 10kHz, (b) Apparent charge concentration in L09 before and after stress at 10kHz.

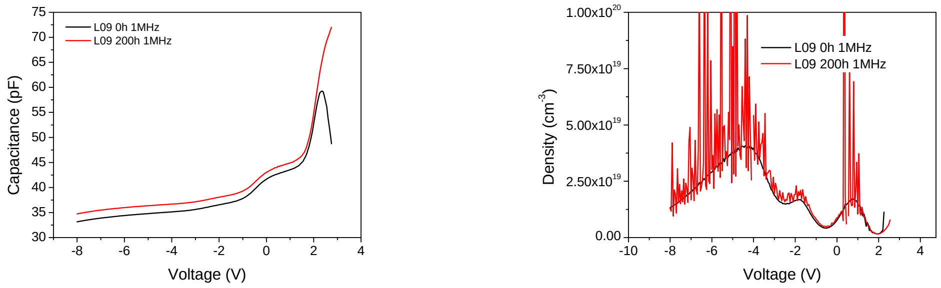

(a) (b)

Figure 4.20: (a) CV plot of L09 before and after degradation at 1MHz (b) Apparent charge concentration in L09 before and after stress at 1MHz.

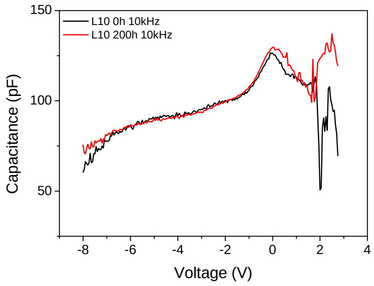

The Apparent charge concentration
in L10 at 10kHz is too noisy
To have any significance

(a) (b)

Figure 4.21: (a) CV plot of L10 before and after degradation at 10kHz (b) Apparent charge concentration in L10 before and after stress at 10kHz.

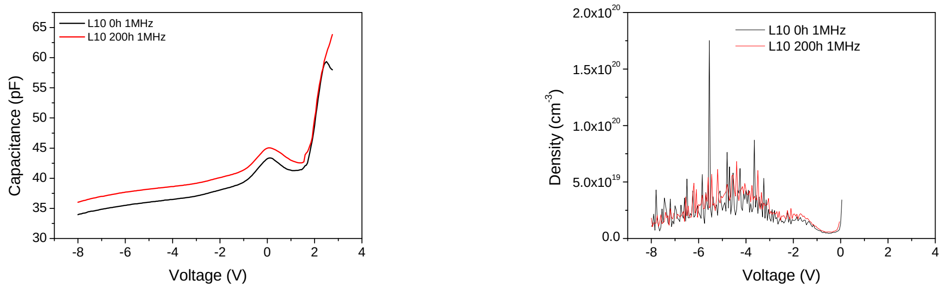

(a) (b)

Figure 4.22: (a) CV plot of L10 before and after degradation at 1MHz b) Apparent charge concentration in L10 before and after stress at 1MHz.

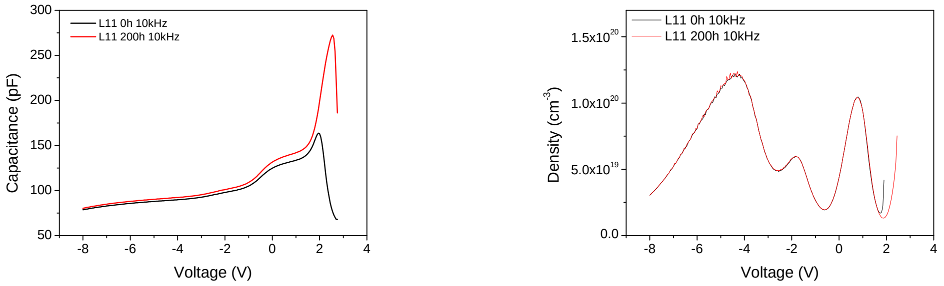

(a) (b)

Figure 4.23: (a) CV plot of L11 before and after degradation at 10kHz, b) Apparent charge concentration in L11 before and after stress at 10kHz.

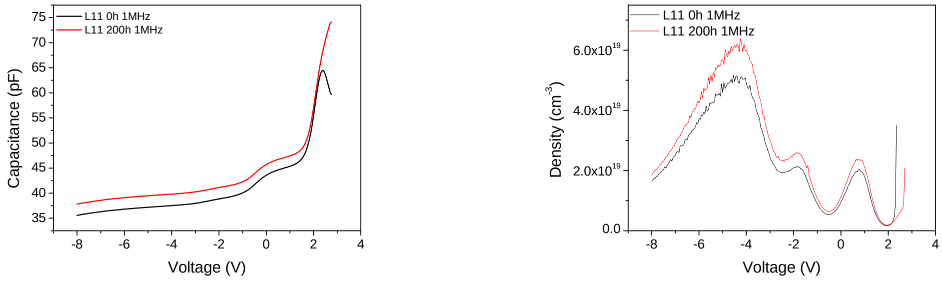

(a) (b)

Figure 4.24: (a) CV plot of L11 before and after degradation at 1MHz, b) Apparent charge concentration in L11 before and after stress at 1MHz.

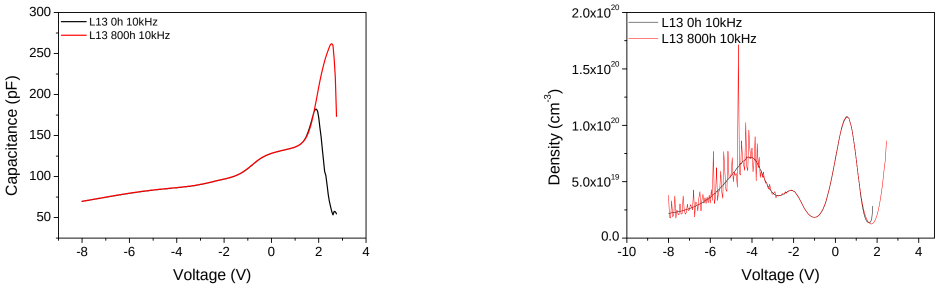

(a) (b)

Figure 4.25: (a) CV plot of L13 before and after degradation at 10kHz b) Apparent charge concentration in L13 before and after stress at 10kHz.

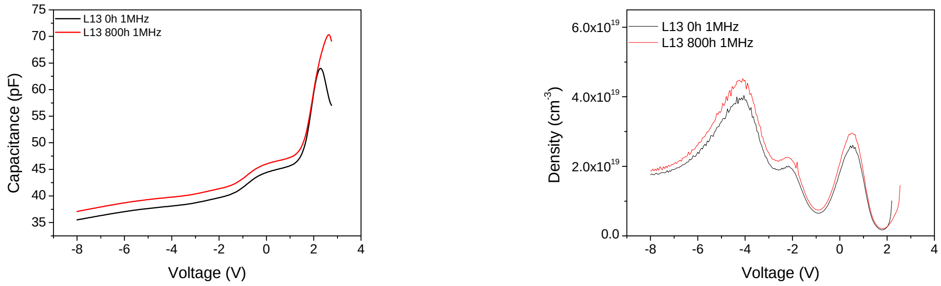

(a) (b)

Figure 4.26: (a) CV plot of L13 before and after degradation at 1MHz b) Apparent charge concentration in L13 before and after stress at 1MHz.

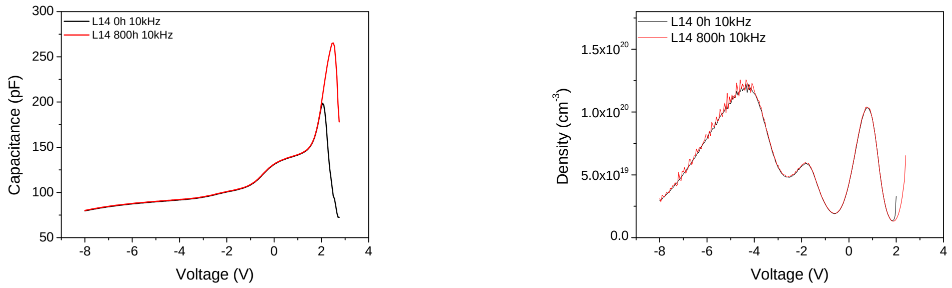

(a) (b)

Figure 4.27: (a) CV plot of L14 before and after degradation at 10kHz, b) Apparent charge concentration in L14 before and after stress at 10kHz.

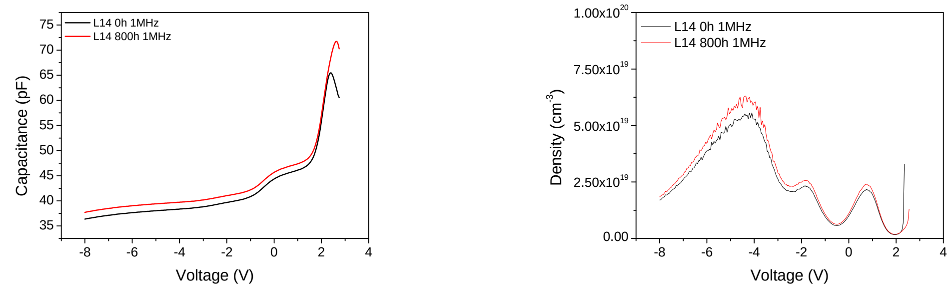

(a) (b)

Figure 4.28: (a) CV plot of L14 before and after degradation at 1MHz, b) Apparent charge concentration in L14 before and after stress at 1MHz.

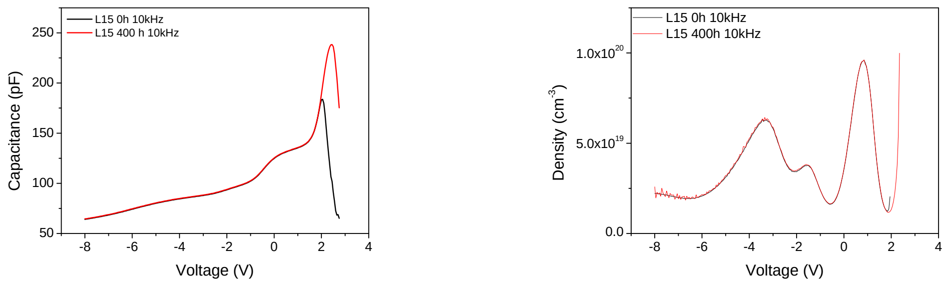

(a) (b)

Figure 4.29: (a) CV plot of L15 before and after degradation at 10kHz, b) Apparent charge concentration in L15 before and after stress at 10kHz.

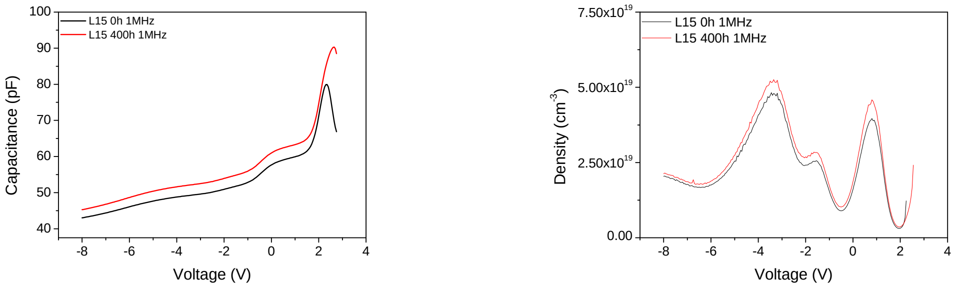

(a) (b)

Figure 4.30: (a) CV plot of L15 before and after degradation at 1MHz, b) Apparent charge concentration in L15 before and after stress at 1MHz.

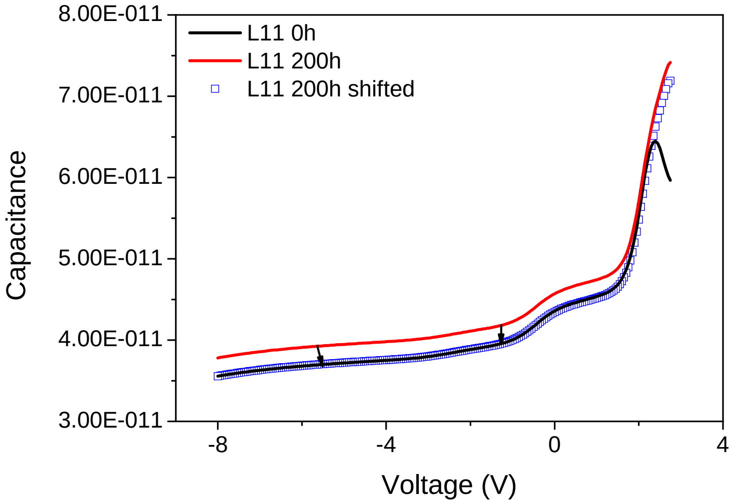

Figure 4.31: Shifting the L11 CV curve after degradation by a fixed value we obtain the 0h CV curve.

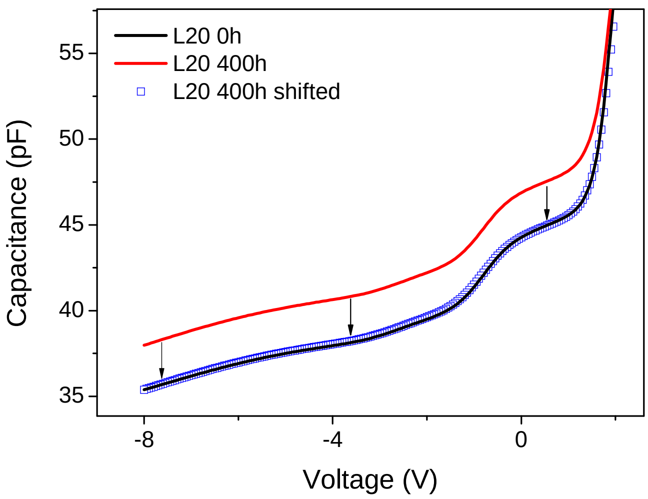

Figure 4.32: Shifting the L20 CV curve after degradation by a fixed value we obtain the 0h CV curve.

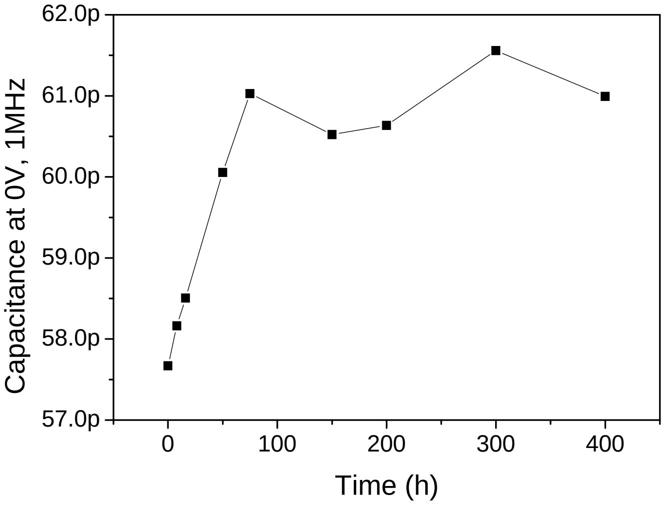

Figure 4.33: Capacitance variation during degradation for L15.

A possible explanation of the increase in device capacitance could be related to the intrinsic approximation due to CPG model. A pn diode consist of a junction capacitance C, a junction conductance G, and a series resistance Rs, as shown in Fig. 4.34 (a). The series resistance depends on the bulk wafer resistivity and on the contact resistances. The LCR meter assume the device to be equal to a specific simplified model, in our case CPG (Capacitance Parallel Conductance) shown in 4.34 (b). Comparing the two circuits we can determine the C_p and G_p approximations as follow:

$$C_p = \frac{C}{(1+R_sG)^2 + (\omega R_sC)^2} \tag{4.9}$$

$$G_p = \frac{G(1+R_sG) + R_s(\omega C)^2}{(1+R_sG)^2 + (\omega R_sC)^2} \tag{4.10}$$

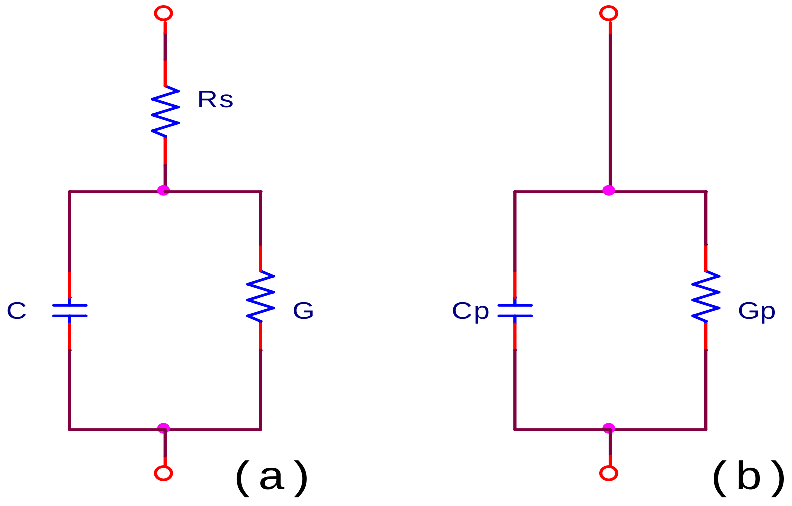

Figure 4.34: (a) pn junction model and (b) CPG equivalent model.

A variation in Rs parameter could therefore imply a variation in apparent Cp parameter. During degradation we have detected a decrease in L20 device series resistance (4.35) and this variation could be responsible for the capacitance variation induced by stress. This hypothesis does not find confirmation, as a matter of fact not only the kinetic of the two parameter are different, but some simulation carried out to detect the possible effects of a variation in series resistance reject the hypothesis. The simulations have been carried out by means of Pspice simulation tool, the simulations have been performed on the simplified circuit reported in Fig. 4.34 (a). The capacitance and the parallel resistance has been extrapolated from CV measurement on L20 at 1MHz, the series resistance has been considered as a simulation variable. The CPG model (Fig. 4.34 (b)) has then be applied to the equivalent impedance extrapolated from simulations. Results presented in Fig. 4.36 show that in order to obtain a capacitance variation compatible with those detected after the degradation at 1MHz the variation in Rs should be in the order of hundreds of ohm.

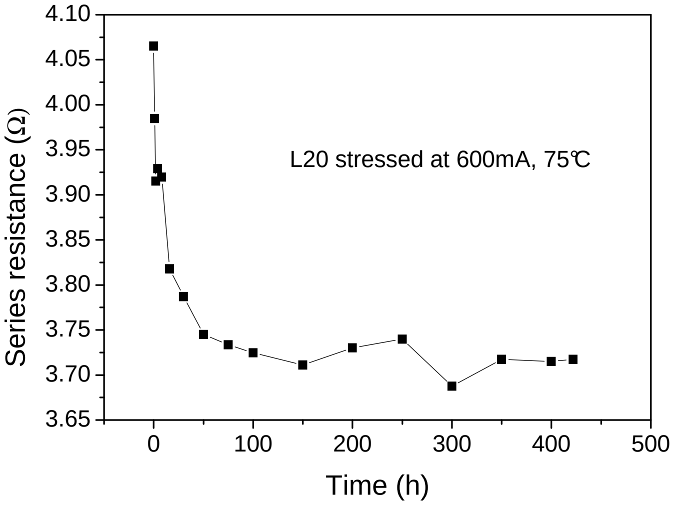

Figure 4.35: L20 series resistance variation during device degradation.

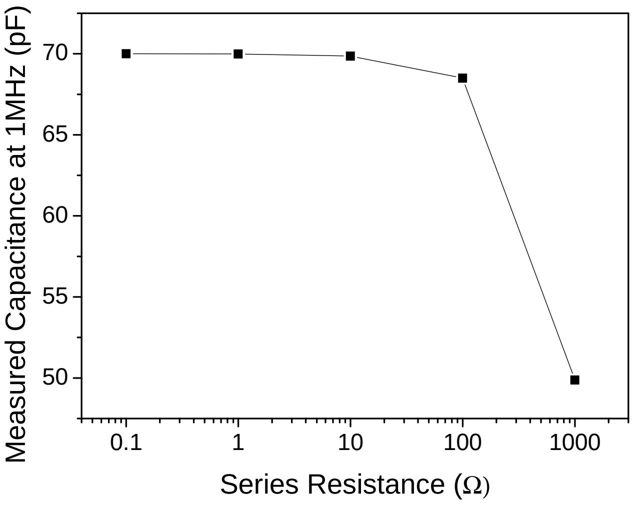

Figure 4.36: Simulation of Cp variation at 1MHz as a function of series resistance Rs.

4.6 Analysis of the spectral variations during LED-like degradation:

4.6.1 Introduction

In a recent article published by APL, Muller et al. [51], Osram OS, studied the burn-in mechanism in InGaN 450nm LD. In this study a direct correlation between short term aging and spreading effects is suggested. In particular the study of the spectral variation indicated such conclusion. In order to understand if a similar effect takes place also in Panasonic devices, we have submitted one LED-like device, L24, to automatic stress (600mA, 75°C) procedure where optical measurement were performed by means of a spectrometer. Results indicate that only a slight variation in peak wavelength emission is detected after 200h of stress. Comparing the results with those proposed by Muller indicate that the hypothesis of current spreading does not apply to LED-like devices.

4.6.2 Experimental details

The EL measurement have been performed by means of Ocean Optics USB4000 spectrometer, to increase measurement stability the LED-like temperature has been fixed to 25° C by means of TEC fixture system. The measurement have been performed in the range 10-500mA.

4.6.3 Results:

Figure 69 through 72 compare the results proposed by Muller et al. (from here defined as "OS LD") and results obtained on LED-like devices. Comparing the effects of the degradation on the two different devices it is evident that:

- The two devices have a strongly different lifetime, about ten hours for the OS LDs, while the lifetime is greater than several hundred hour for LED-like devices produced by Panasonic
- It is possible to determine that the two degradation kinetics have a different behavior. In fact, the OS LDs degradation kinetic can be easily fitted with an exponential curve, while the LED-like degradation process is instead proportional to the square root of time.
- The peak wavelength variation does almost not occur in LED-like devices, only 0.2 nm variation is detected, while OS LDs suffer a strong blue shift (approximately 8nm) during degradation related to QCSE and screening from electric fields.

From the above discussion we can conclude that the hypothesis proposed by Muller of degradation related to current spreading during ageing thus reducing the carrier density for a given current is not applicable to LED-like devices. The degradation kinetics detected by OSRAM have very fast kinetics, and can be correlated to a poor quality of the materials: this kind of degradation process (exponential kinetics) seems to be completely absent in the LED-LIKE devices produced by Panasonic. The hypothesis of non-radiative lifetime increase related to an impurity diffusion process still remains the principal degradation process for LED-like devices.

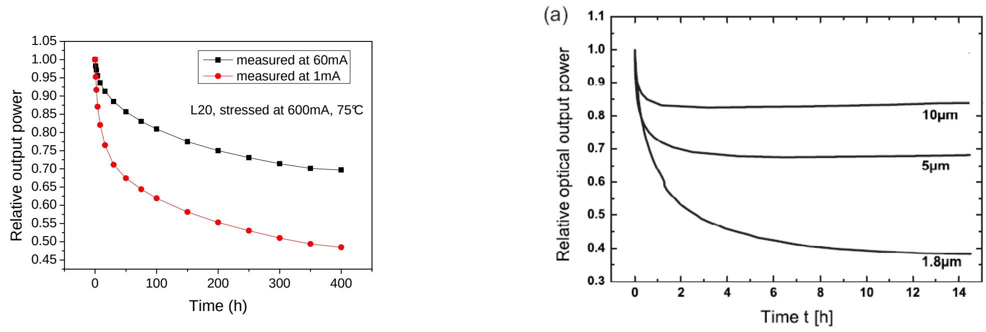

(a) (b)

Figure 4.37: (a) Panasonic L20 and (b) OS LD degradation kinetics.

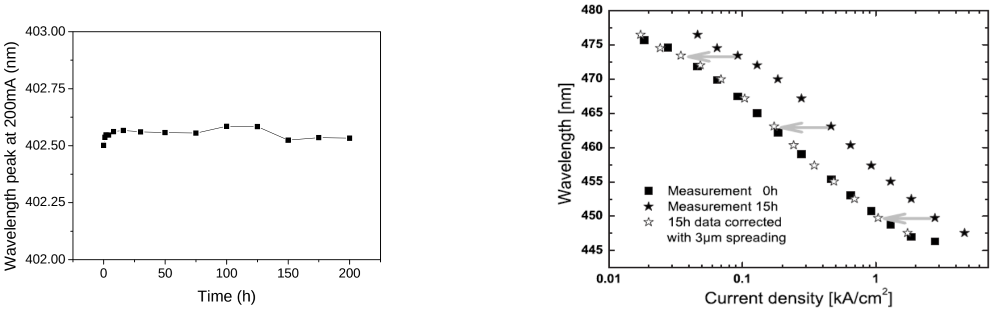

(a) (b)

Figure 4.38: (a) L24 wavelength variation during device ageing measured at 200mA and (b) Osram 450nm LD Wavelength variation in during device ageing, enlightened is the variation at 200mA.

4.6.4 Conclusions

With this report we have summarized the recent research activities carried out on the LED-LIKE samples. The activity consists in a set of characterization and stress experiments, aimed at understanding the possible correlation between the degradation of LED-LIKE and laser samples.

The measurements and tests previously described demonstrate that:

- Stress can induce the degradation of the optical characteristics of LED-LIKE devices. Degradation is more prominent at low measuring current levels, and this result suggests that the OP decrease is due to the increase in non-radiative recombination

- The degradation kinetics have a square-root dependence on stress time. This result is consistent with our previous findings on laser diodes, and suggests that degradation is correlated to a diffusion process

- The defect-related (generation-recombination) components of the I-V curves show an abrupt decrease during the initial stage of the stress tests (not correlated to any modifications in the optical parameters), followed by a gradual increase according to the square-root of stress time. The gradual variation in the G/R components of the I-V curves is strongly correlated to the decrease in output power

- The capacitance-voltage curves of the devices show modifications after stress. In particular we have detected: (i) a shift of the critical voltage towards higher levels, possibly due to the decrease in the generation-recombination components detected after stress; (ii) an increase in junction capacitance in the whole analyzed voltage region, possibly correlated to modifications in the electrical characteristics of the samples; (iii) no strong modifications in the apparent charge profiles

- Devices do not show any significant wavelength shift after stress. This result suggests that no significant variation of the carrier density is taking place as a consequence of stress: the fast degradation mechanism proposed by OSRAM seems not to be present in the devices produced by Panasonic

On the stressed devices, we are also carrying out DLTS characterization. Unfortunately, the amplitude of the DLTS signal is pretty low, and we are adjusting our system in order to achieve more resolution and reliable result. This has implied a certain delay in the measurements: details on this will be provided in the near future.

Chapter 5

Reliability of AlGaN Deep Ultra Violet LEDs

5.1 Introduction

The several applications of Ultraviolet light are of great importance both in scientific and industrial fields, particularly interesting is the high energy Deep UltraViolet (DUV) spectrum. At the moment the only commercial systems used to obtain UV light are based on low pressure mercury lamp. Unfortunately these systems are also affected by several drawbacks such as: pollution of Hg, high operating voltage, low efficiency and limited lifetime. A viable solution arises from Light Emitting Diode (LED) technology. LEDs emitting in the Deep-Ultraviolet (DUV) spectral region with a spectral peak down to 237nm have been subjected to great development over the last few years: important efforts have been done in order to improve the performance of AlGaN-based DUV LEDs. These devices are expected to find application in the lighting field, in the next-generation water/air purification systems and in a wide spectrum of biomedical systems. The growth of this kind of devices is critical, due to the high aluminum content of the active region, and to the difficulty of growing optically efficient AlGaN layers on sapphire substrates, with low-dislocation densities. The poor reliability of DUV LEDs is a critical aspect that still slows the adoption of these devices into mass applications. Some preliminary results on the degradation of AlGaN-based LEDs have been already reported [52] and several factors have been shown to limit the performance of such devices, such as the poor electrical conductivity of the AlGaN layers, structural defects that can propagate to the active region [53], and the deep-levels assisted radiative recombination [54], that significantly reduces carriers injection towards the QWs. Up to now no extensive analysis on the gradual and catastrophic degradation of these devices and on the role of current and temperature in determining the optical power decrease has been published up to now. The aim of the work reported in this section is: (i) to give a description of the parametric and catastrophic degradation of AlGaN-based DUV-LEDs, and (ii) to analyze the role of current and temperature in determining the degradation kinetics.

5.2 Determination of degradation kinetics

5.2.1 Experimental details

The analysis has been carried out on DUV LEDs produced by Sensor Electronic Technology, Inc. The structure consists of an n-AlGaN:Si cladding layer, an AlGaN multiple-QW (MQW) layer, a p-AlGaN cladding layer, and a p-AlInGaN contact layer. Details on the device structure can be found in [55]. The analyzed devices had emission wavelengths equal to 280-295 nm (series UV1 and UV2, respectively), depending on the aluminum molar fraction in QWs. We have submitted the devices to an extensive optical characterization at room temperature (RT) by means of EL measurements. The aim of this preliminary analysis was to understand the radiative processes responsible for the device emission, both for what concerns the main emission peak (UV) and the secondary spectral bands related to deep levels, already reported in the literature [56], [57]. This kind of analysis has provided information on how the different radiative mechanisms compete for the recombination of electronŨhole pairs. The LEDs have then been submitted to constant-current stress at the nominal current of 20 mA. At each stage of the aging tests, a complete electrical and optical characterization has been carried out, with the aim of achieving a good understanding of the degradation process. Adopted characterization techniques include current-voltage (I-V), capacitance-voltage (C-V), integrated OP, and EL measurements. The results of this analysis are summarized in the following.

5.2.2 Spectral Features before stress

The spectral profiles of untreated samples consist of an asymmetric main UV emission centered at about 4.46 eV (278 nm) and 4.20 eV (295 nm) for the two series of analyzed devices (UV1 and UV2), respectively. The full-width at half-maximum varies between 10 and 15 nm and is in accordance with previously reported values [57], as shown in Fig. 5.1 for one LED emitting at 278 nm.

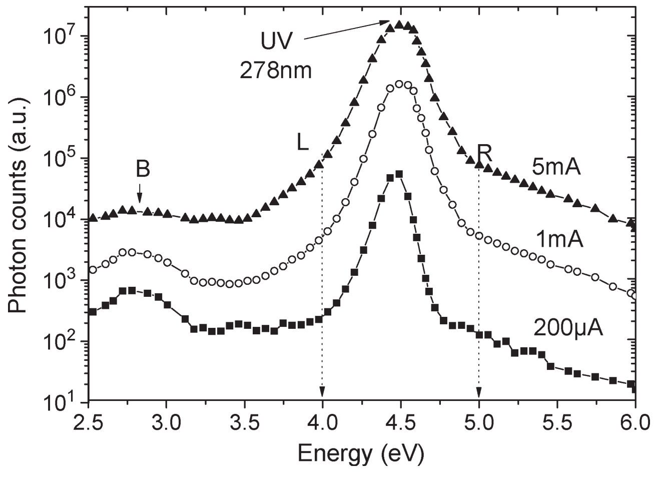

Figure 5.1: EL spectra of one LED with emission at 278-nm UV line measured at three different current levels.

The spectra of the analyzed devices showed interesting features: For both the series of LEDs, we have detected the following: 1) a shoulder superimposed to the high-energy side of the main peak (at about 5 eV in Fig. 5.1, referred to as R band), likely related to the radiative emission from n-AlGaN layers, and 2) an emission band in the spectral range below 4 eV (band B in Fig. 5.1), previously attributed to radiative recombination through defects [56]and [57]. Electrons and holes injected into the LED active region only partially give light through the main band-to-band (UV) radiative recombination process. In fact, at the same time, several other processes contribute to carrier recombination, including nonradiative recombination, radiative recombination through deep levels, electron/hole trapping, and carrier leakage out of the active region [56], [58]. Among these mechanisms, the relative weight of band-to-band and deep-level-assisted transitions establishes the power-law dependence of the luminescence intensity-versus-current (L-I) curves [56]. If the trap-assisted processes are negligible, the intensities of the UV band (I_{UV}) and the B-band (I_B) show a linear ($I_{UV} \approx I$) and a sub-linear ($I_B \approx I^{1/2}$) dependence on injected current (I) respectively. On the other hand, if the trap-related mechanisms become significant, the current laws are quadratic ($I_{UV} \approx I^2$) and linear ($I_B \approx I$), respectively. Following this model, we describe here the optical behavior of the LEDs emitting at 278 nm (LED UV1, with higher energy separation between UV and deep-level emission bands) and the factors affecting UV emission in as-received and aged samples.

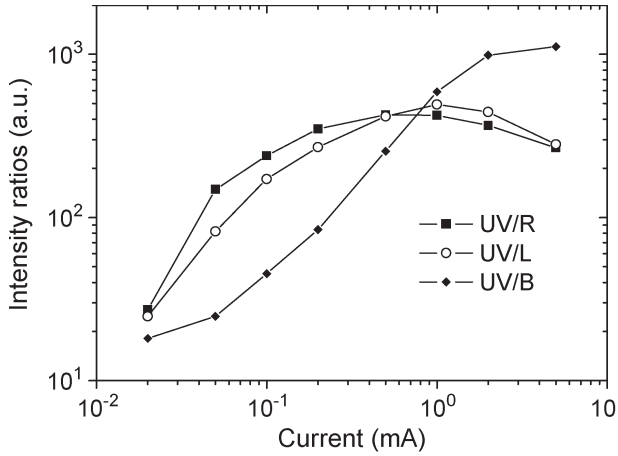

Figure 5.2: Ratios between intensities of UV emission and R and L bands as a function of current for one LED emitting at 278 nm.

First, the effects of carrier overflow in the active region can be evaluated by analyzing the intensity ratios I_{UV}/I_L and I_{UV}/I_R between the UV emission peak and each of two shoulders L and R, respectively, related to trap-assisted emission in the p-AlGaN and to radiative recombination in n-AlGaN. In Fig. 5.2, the ratios are shown as a function of current: Both the ratios present a well-marked maximum at about 0.5 mA (R band) and 1 mA (L band), suggesting an increasing escape rate of carrier from the active layers at higher current levels. On the other hand, the ratio I_{UV}/I_B between UV and B intensities (shown in Fig. 5.2) shows an increasing trend up to a saturation at high currents. In Fig. 5.3, we show the dependence of the intensity of the radiative emission bands on driving current. As can be noticed, the intensity of the UV emission has a quadratic dependence on injected current ($I_{UV} \approx I^2$), whereas the deep-level band B varies linearly with current ($I_B\ I$). On the basis of previous works [56], this fact indicates that trap-related recombination is relevant with respect to band-to-band recombination and that it significantly affects the intensity-current relation. Even if the performance of the analyzed LEDs is competitive for commercial application, these results indicate that there is still room for improvement of the optical characteristics of the devices, by reducing the contribution of trap-related recombination with respect to NBE emission, until reaching linear dependence of the UV intensity on applied current.

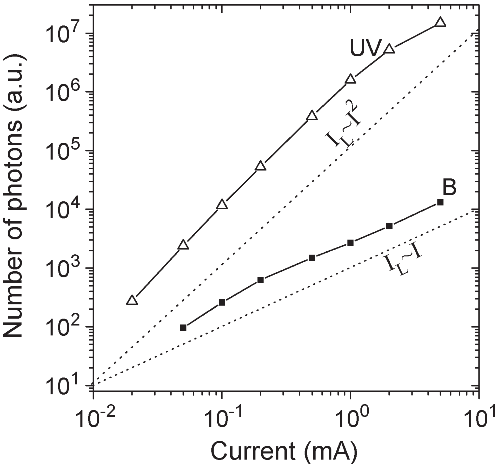

Figure 5.3: Emission intensities for UV and B spectral components as a function of current for one LED emitting at 278 nm. Dotted lines show power law $I_L \approx I^P$, where P = 2 and P = 1.

A more detailed investigation of low-energy emission bands has been carried out over a wide current range (from 20 μA to 5 mA). The results are shown in Fig. 5.4 (a), where we have plotted the EL spectra measured on one LED at different current levels, normalized to the maximum of the UV emission. No blue shift of the main emission peak with increasing currents has been detected on the analyzed samples. This suggests that localization effects in the AlGaN layers are negligible [59]. Two wide emission bands (B1 centered at about 2.78 eV and B2 at 3.4 eV) are well resolved at currents below 200 μA. These bands are ascribable to the presence of two deep-level radiative recombination mechanisms within the active region. The validation of this hypothesis is given by considering that relative intensity of these bands increases on decreasing current. In fact, at high injection current levels, these parasitic radiative paths saturate, and their contribution to the overall emission becomes negligible with respect to the main UV peak. As a consequence, the normalized intensities of B1 and B2 [shown in Fig. 5.4(b)] decrease on increasing current following an almost inverse proportionality, suggesting a saturation of the related centers at high carrier densities.

5.2.3 Effects of Stress on DUV LEDs

Fig. 5.5 shows the optical-power-versus-input-current (L-I) curves measured before and during stress on one of the analyzed devices. Stress induced the decrease of the

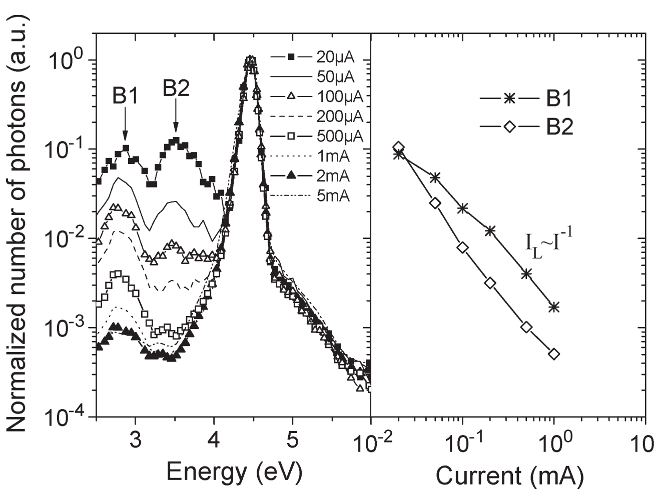

Figure 5.4: (a) EL spectra for one LED emitting at 278 nm (normalized to the intensity of UV emission) at different currents. (b) Normalized intensity of B1 and B2 bands as a function of current. Dotted line shows power law $I_L \approx I^P$, where P = -1.

optical power of the devices in the whole investigated current range. The kinetic of the OP decay can be understood from Fig. 5.6, showing the OP degradation measured at 10 mA during stress time. The OP decrease took place mostly during the initial 200 h of treatment, whereas the behavior of the devices was found to be quite stable in the remaining stress time.

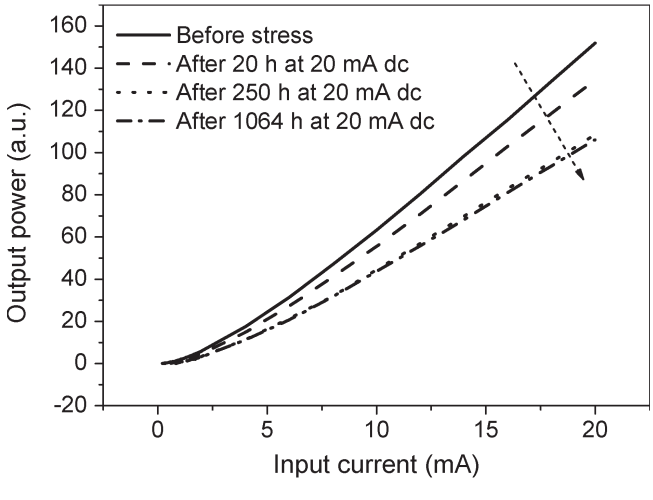

Figure 5.5: L-I curves measured before and after stress on one of the aged LEDs ($\lambda = 295nm$; stress at 20-mA dc).

In order to evaluate the entity of the optical-power decay at different measuring current levels, in Fig. fig:TDMR7, we show the L-I curves measured before and during stress (already shown in Fig. 5.5), normalized to the values obtained on the untreated sample. The OP decay was found to be more prominent at low measuring current levels: For a measuring current of 1 mA, the OP loss was around 60%, whereas at 20 mA, we detected only a 30 % OP decrease. This fact suggests that OP decrease is related to the generation of nonradiative centers, which reduce the internal quantum efficiency of the devices [58], [60]. At high current levels, these centers are saturated by the high flux of injected carriers, and therefore, optical-power loss is limited.

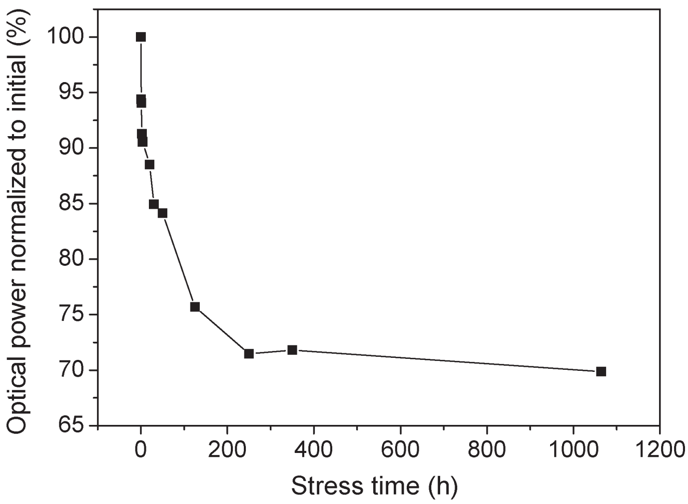

Figure 5.6: Optical-power decay measured at 10 mA on one of the aged LEDs ($\lambda = 295nm$; stress at 20-mA dc).

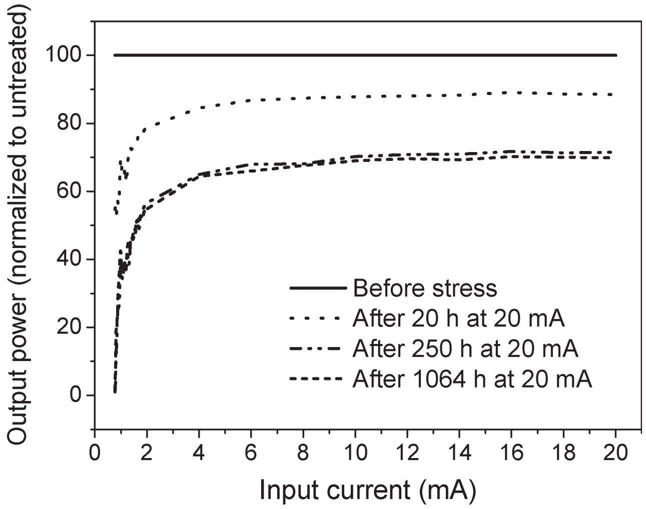

Figure 5.7: Normalized L-I curves measured before and after stress on one of the aged LEDs ($\lambda = 295nm$; stress at 20-mA dc).

The degradation of spectral profiles during stress is shown in Fig. 5.8. No significant variation of the spectral shape has been detected as a consequence of aging. This fact indicates that the decrease of the main UV peak is not related to the generation/increase of alternative radiative recombination paths and strengthens the hypothesis that OP loss is due to the increase of the nonradiative recombination rate. In order to better characterize the degradation process, we have carried out an extensive electrical characterization of the samples submitted to stress. DC aging did not induce significant modifications of the forward I-V curves of the devices, i.e., no significant increase of operating voltage has been detected after stress (see the semilogarithmic I-V curves in Fig. 5.8). On the other hand, the device current increased (ten times) both in the reverse- and low positive-bias regions, suggesting that stress induces the increase of the generation/recombination or tunneling components.

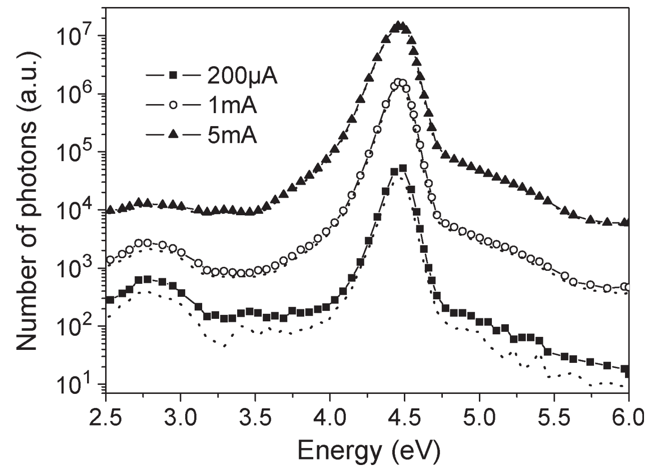

Figure 5.8: EL spectra of LED UV2 at three different currents (symbols) before aging and (dotted lines) after 200 h of aging.

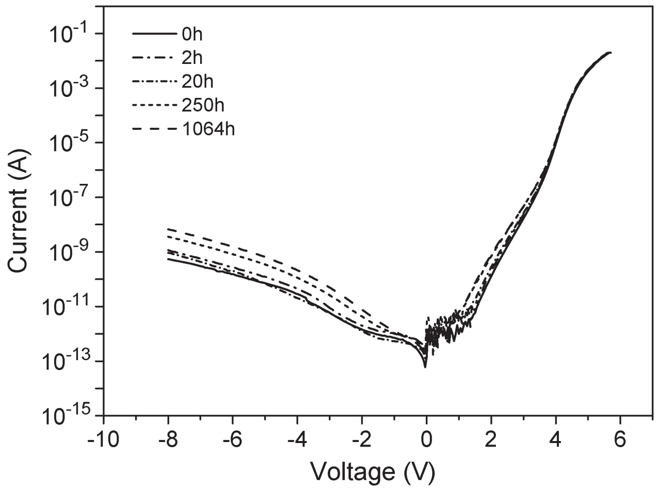

Figure 5.9: Current-voltage curves measured before and after stress on one of the aged LEDs ($\lambda = 295nm$; stress at 20-mA dc).

From the optical characterization of device degradation (Figs. 5.5-5.7), we have obtained pieces of evidence that OP decrease can be due to an increase of the nonradiative components in the active region. This process can be related to the propagation of defects toward the active region of the devices, taking place as a consequence of carrier flow. In order to find a correlation between degradation process and modifications of the properties of the active region, we have carried out capacitance-voltage characterization of the devices at each step of the aging tests. By C-V characterization, it is possible to extrapolate information on the apparent charge distribution (ACD) within the space-charge region (SCR) [61], [62] and [11] under the n+/p asymmetric junction approximation (see the schematic structure of the devices in [63]). Fig. 5.10 (bottom) shows the variation of the ACD profile with LED voltage. The solid line is referred to as the untreated sample: With increasing reverse bias, the SCR boundary is swept through the different layers constituting the active region. Peaks A and B (at -1 and -2.25 V, respectively) and valley C (at -4.32 V) in the ACD profile correspond to the charge-accumulation (heterointerfaces) and depletion points present in the active region, respectively [61], [62] and [11]. In particular, peak B represents the heterointerface in the active region which is closest to the bulk p-side, since it is the last peak detected, increasing reverse bias before the bulk region (region D and beyond, for reverse voltage below -7 V) [54].

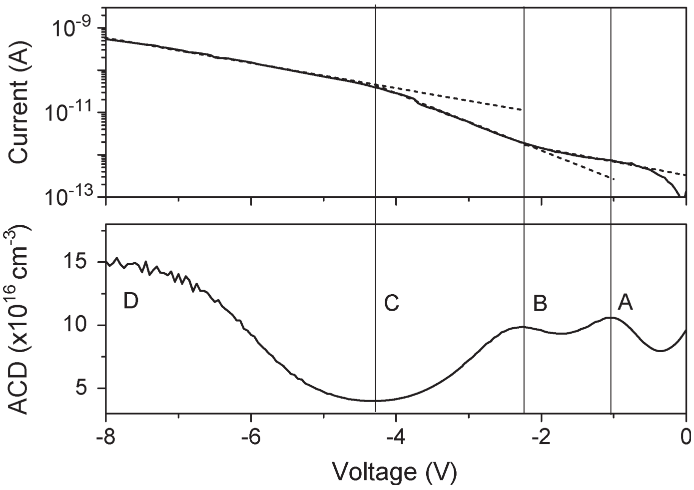

Figure 5.10: (Top) I-V curve measured before stress on one of the analyzed samples. (Bottom) ACD-profile-versus-voltage curves measured before stress on one of the analyzed devices ($\lambda = 295nm$; stress at 20-mA dc).

Fig. 5.10 shows also the comparison between the ACD profile (bottom) and the reverse-current characteristic (top), with varying reverse bias. It is shown that, when the SCR boundary crosses each of the accumulation and depletion points detected by ACD analysis, the slope of the semilogarithmic I-V curves changes. This fact indicates that reverse-current transport is strongly governed by the position of the SCR boundary in the active region and is in good agreement with previous results on InGaN LEDs [64].

Fig. 11 shows the variation of the ACD profile induced by stress at 20 mA. DC-bias aging induced the increase of the charge concentration, particularly close to peak B (the last heterointerface before the bulk side) and in region D (close to the bulk side). These changes take place mostly during the initial 250 h of treatment, just like the optical-power decrease. This fact suggests that the optical-power decrease and the modifications of the charge profile are correlated, and it is consistent with previous literature work on InGaN-based blue LEDs [54]. On the basis of the results shown in Figs. 5.5-5.7, degradation can be attributed to the increase of the nonradiative recombination rate, which is related to the worsening of the properties of the active layer of the devices. The ACD profiles measured during stress indicate that stress induces localized modifications of the charge distribution, which can be related to the generation of defective states on the basis of previous studies [54]. Therefore, while optical measurements indicate that stress is related to the increase of the nonradiative recombination components, capacitive analysis gives further insight in this degradation process, supporting the hypothesis that stress induces modification in the charge distribution in the active layer due to defect modifications [54]. As a result, we have found that OP degradation is correlated to the modification of the properties of the active layer of the LEDs, particularly in regions B (the last charge-accumulation point before the bulk) and D (close to the bulk).

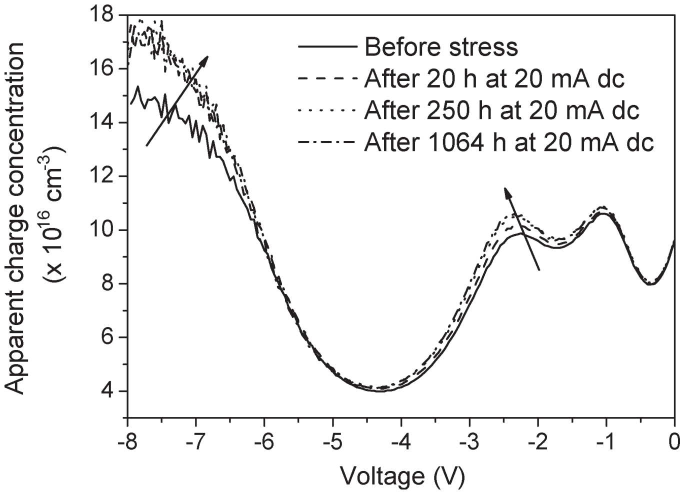

Figure 5.11: ACD-profile-versus-voltage curves measured before and after stress on one of the aged LEDs ($\lambda = 295nm$; stress at 20-mA dc).

5.2.4 Discussion

This Section presents the results of a detailed characterization of DUV-LED performance and reliability. The analysis on AlGaN-based LEDs emitting at 280 and 295 nm has been carried out by means of combined electrical and optical techniques. The optical characterization carried out before stress indicated that carrier recombination is strongly affected by the presence of radiative recombination paths, which are related to deep levels. The analysis of the contributions of the radiative emission peaks has provided information on how the different recombination mechanisms determine carrier dynamics in the active region, indicating that trap-assisted recombination plays an important role in defining optical efficiency of the LEDs. In order to analyze the reliability and degradation mechanisms for these LEDs, we have carried out stress tests under constant-current bias. During stress, the LEDs showed monotonic optical-power decrease: The OP degradation was found to be more prominent at low measuring current levels. This indicates that degradation is related to the generation of nonradiative recombination paths: At low measuring current levels, nonradiative processes can efficiently limit the internal quantum efficiency of the devices because they compete with radiative processes in determining carrier recombination. On the other hand, at higher measuring current levels, the nonradiative paths are saturated by the injected carriers, and most of the flowing electrons and holes can recombine radiatively: This determines a minor OP degradation at high measuring current levels. After stress, we have detected also an increase of LED current in the reverse- and low forward-bias regions, indicating that stress induces an increase of the tunneling and generation/recombination components. This effect is usually attributed to the generation of defects [65], [7]. The effect of stress on the properties of the active layer has been analyzed by means of C-V measurements.We have found that stress induces the increase of the ACD profiles, which can be ascribed to the modification of charge distribution in the active region. These changes can be related to the modification of the properties of trap states inside the active layer of the LEDs [54], which can result in an increase of the nonradiative recombination rate. After stress, we did not measure significant changes of the emission spectra of the devices, even for what concerns the deep-level emission peaks B1 and B2 (Fig. 5.8). This is a further confirmation of the nonradiative nature of the process responsible for the optical-power decrease because the characteristics of radiative processes are not modified by aging in the analyzed energy range (2.5-6 eV). In conclusion, we have presented here a study on DUV-LED performance and reliability. We have analyzed in detail the relation between the different radiative emission processes by evaluating the relative EL intensity of the three main emission bands of the LEDs. We have also presented an analysis of the mechanisms that limit the reliability of these devices during dc stress. In particular, we have shown that OP degradation can be ascribed to the increase of the nonradiative recombination rate. C-V analysis provided further information on the degradation process, indicating that, as a consequence of stress, the charge distribution in the active layer is modified, possibly due to the generation of defective states.

5.3 Effects of different driving condition on degradation kinetics

The aim of this section is (i) to give a description of the parametric and catastrophic degradation of AlGaN-based DUV-LEDs, and (ii) to analyze the role of current and temperature in determining the degradation kinetics. The analysis was carried out on a wide number of DUV-LEDs with similar characteristics, emitting at 310 nm, and fabricated by Sensor Electronic Technology, Inc. The results indicate that (i) gradual degradation is correlated to the increase in the non-radiative recombination in the active region of the devices; (ii) stress determines an increase in the defect-related current components of the LEDs, possibly due to an increase in the concentration of defects in the active region; (iii) stress determines an increase in the operating voltage of the LEDs and a decrease in junction capacitance; (iv) the degradation kinetics are strongly dependent on the stress current level, while operating temperature has only a limited impact on the degradation rate; (v) during stress the devices can show catastrophic degradation, due to the generation of parasitic conductive paths in parallel to the junction, in correspondence of the mesa borders.

5.3.1 Experimental Details

We have stressed a number of DUV LEDs under different stress conditions, as summarized in Table I. In particular, a set of devices was stressed at different temperature levels (between RT and 70 řC), with the same stress current level (20 mA dc, see rows B, C, D in Table I). Another set of devices was aged at different current levels (in the range 5-20 mA), with the same junction temperature Tj (ambient temperature was adjusted in order to have the same Tj for the different stressed devices, see rows B, E, F in Table I).

Sample	Current	Ambient Temperature	Junction Temperature
A	30 mA	RT	57 ° C
B	20 mA	RT	53 ° C
C	20 mA	50 ° C	76 ° C
D	20 mA	70 ° C	93 ° C
E	5 mA	49 ° C	53 ° C
F	10 mA	38 ° C	53 ° C
G	0 mA	53 ° C	53 ° C

Table 5.1: Stress conditions adopted for the reliability tests.

Thermal Characterization Tj was evaluated by means of the method proposed in [53]. This method is based Firstly the electrical characteristics of the devices have been biased with very short current pulses (as presented in Fig. 5.12. Characterization of the devices has been performed at different temperatures with a thermocontrolled oven. The result of this measurement has been plotted in fig. 5.13

Before carrying out the ageing tests, a careful analysis of devices thermal resistance has been carried out, as a matter of fact in order to perform isothermal stresses the junction temperature of the devices has to be carefully measured. Therefore, junction temperature has been evaluated by means of current-voltage thermal maps, using the method described by Xi and Schubert [53], [66] . A set of voltage measurements was carried out at different current (between 5 and 20 mA) and temperature (To between 35 and 85 °C) levels in a thermal chamber. The measurements were carried out using short current pulses in order to avoid devices self heating(as presented in Fig. 5.12). Figure 5.13 shows that for each measuring current (I) level the relation between the corresponding voltage and temperature is roughly linear, and can be expressed by means of

$$Vf = A + BT \tag{5.1}$$

where T is the ambient temperature, controlled by the oven, A and B are fitting parameters. The slopes of the curves in Figure 5.13 were therefore evaluated by means of linear fittings, and used as coefficients for junction temperature evaluation in the following analysis. The chamber temperature was subsequently fixed at 35 ° C, and the devices were biased for a fixed period (300 seconds) at each of the measuring current levels used before: during bias at fixed current, LEDs voltage decreased exponentially, due to junction self-heating. For the same driving current Im, a difference in forward voltage corresponds to a difference in devices operating temperature. Therefore, with

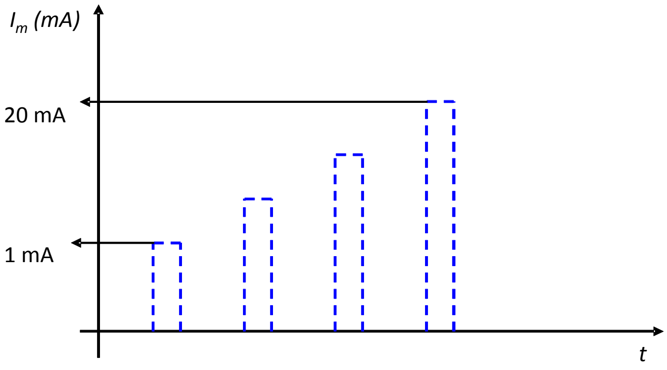

Figure 5.12: Schematic representation of the short pulses measurement.

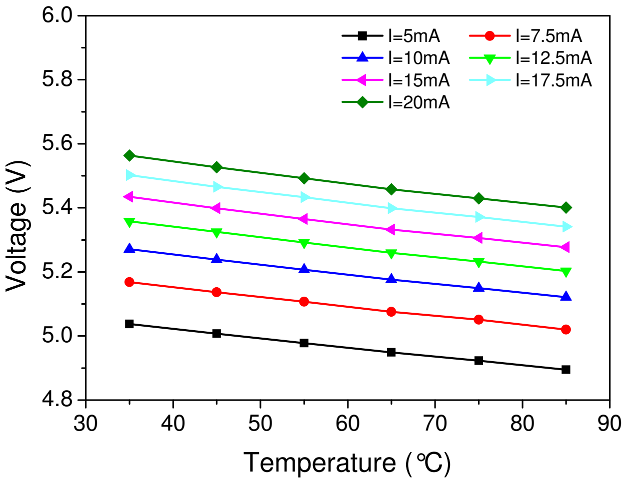

Figure 5.13: Thermal mapping of a DUV LED.

an exponenetial fitting, it is possible to obtain the final voltage value by means of an exponential decay fitting, as reported in Fig 5.14. It is therefore possible to obtain the final temperature from the calibration data previously described, and inverting equation 5.1.

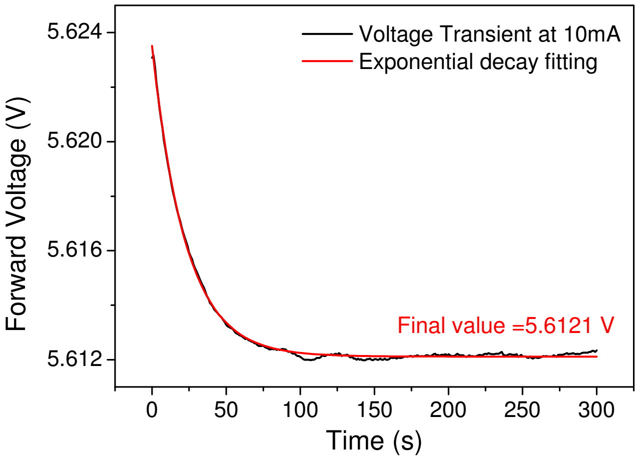

Figure 5.14: Thermal transient of a DUV LED.

From the final temperature reached by the junction during bias, we can evaluate the thermal resistance, by means of a T_j vs electrical power plot. The plot obtained for the DUV LEDs has been reported in Fig. 5.15. The measured thermal resistance value is 260 K/W.

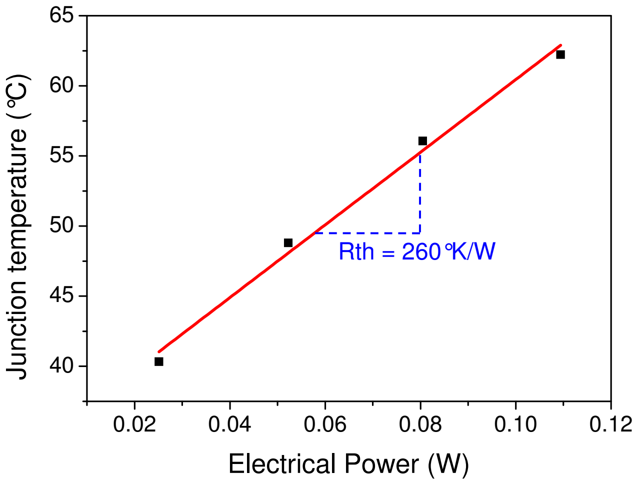

Figure 5.15: Thermal resistance evaluated from the thermal mapping procedure.

5.3.2 Results

In Fig. 5.16 we report the optical power (OP) vs current characteristics measured during stress time on one of the analyzed LEDs. In Figure 2 we report the optical power degradation measured at two different current levels on the same device. As can be noticed, stress induced a significant decrease in the efficiency of the samples, especially at low measuring current levels. This result suggests that stress determines the increase in the non-radiative recombination rate in the active region of the devices [6].

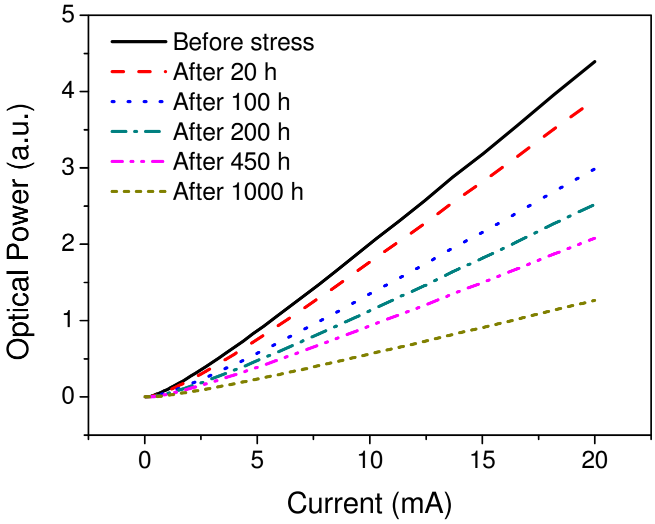

Figure 5.16: Optical power vs Current curves measured during stress on one of the analyzed samples (stress at 30 mA, RT).

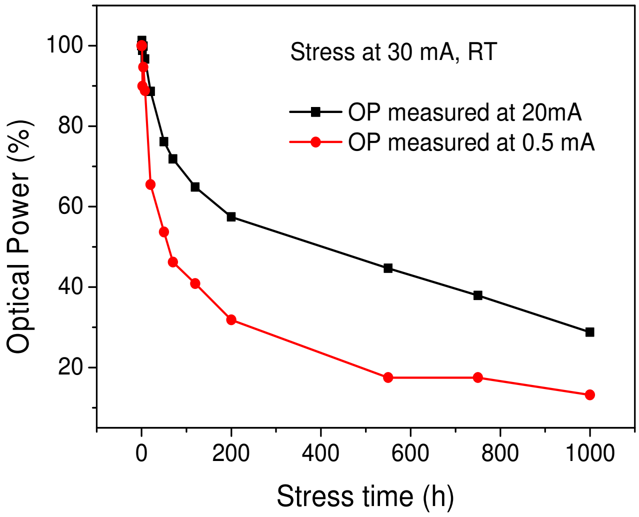

Figure 5.17: optical power degradation measured at different current levels during stress on one of the analyzed samples.

Stress was found to induce also an increase in the defect-related components of the current-voltage (I-V) characteristics of the samples (log scale in Figure 5.18), suggesting that degradation is correlated to the generation or propagation of lattice defects in the active region of the LEDs [54]. Considering the low current levels adopted for the stress tests, degradation can be ascribed to a sub-threshold defect generation process, as previously described in [38] . Stress was found to induce also an increase in the

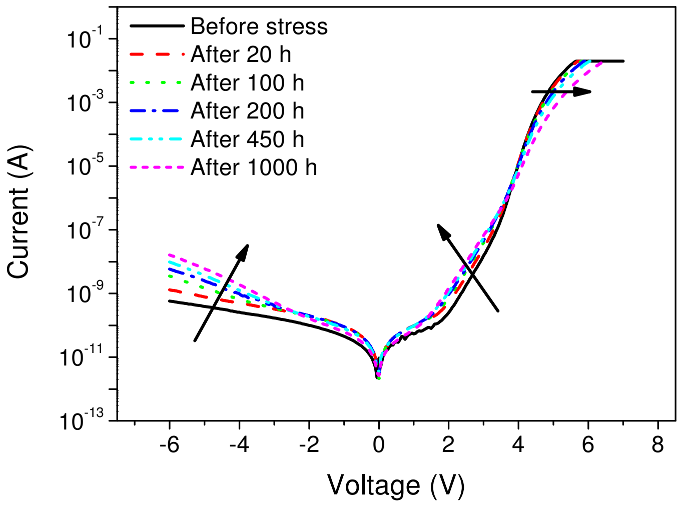

Figure 5.18: Current-voltage characteristics measured before and during stress on one of the analyzed samples (stress at 30 mA, RT, log scale).

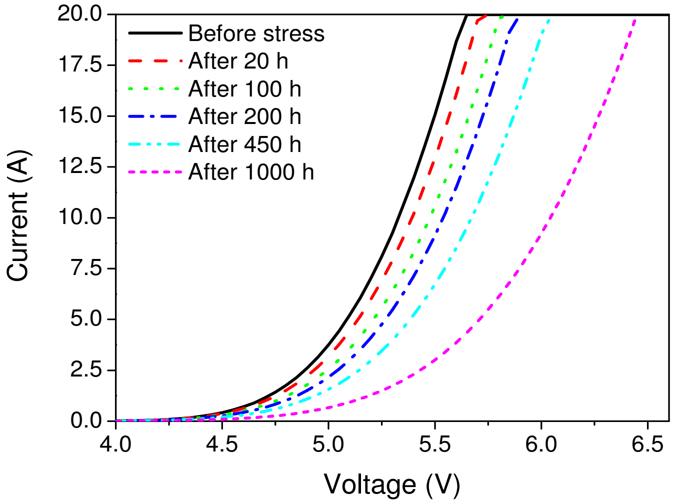

Figure 5.19: Current-voltage characteristics measured before and during stress on one of the analyzed samples (stress at 30 mA, RT, linear scale).

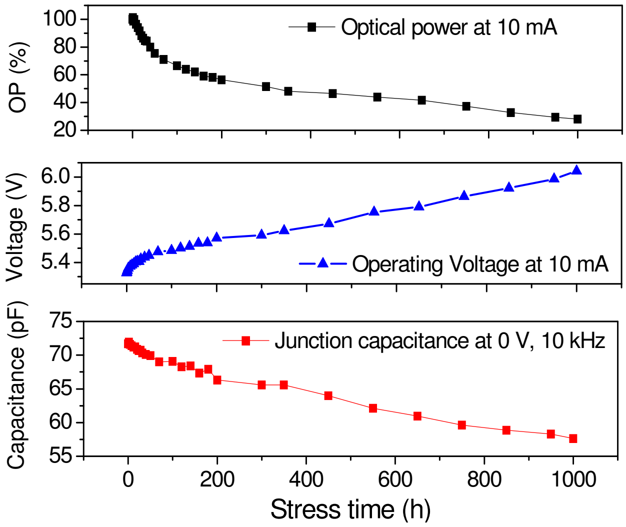

Figure 5.20: OP decrease, operating voltage increase and junction capacitance decrease measured on one of the analyzed devices during stress at 30 mA, RT.

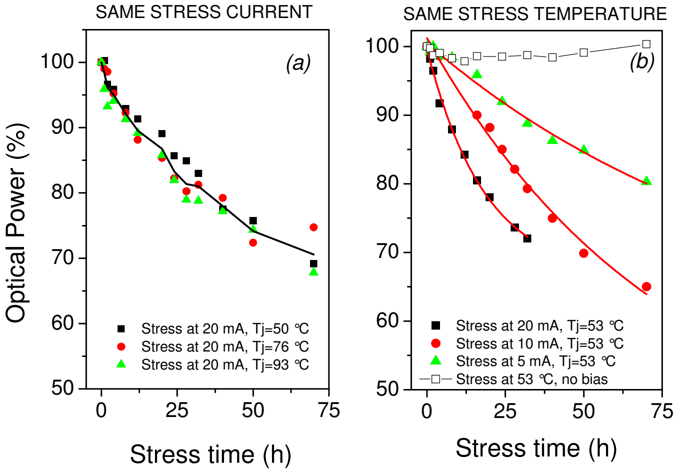

Figure 5.21: Optical power degradation measured during stress at (a) different temperature and (b) at different current levels.

operating voltage of the devices (Figure 5.19 and 5.21). This effect can be correlated to the worsening of the properties of the ohmic contacts of the LEDs [67], and/or to the increase in the resistivity of the neutral regions due to the partial compensation of the acceptor dopant by hydrogen (generation of Mg-H bonds) [68]. The operating voltage increase was found to be also correlated to a decrease in the junction capacitance (Figure 5.20), that can be a signature (i) of the decrease in the effective acceptor concentration at the p-side of the diodes due to the generation of Mg-H bonds [68], (ii) or of the degradation of the properties of the ohmic contacts of the LEDs [69].

Furthermore, we have demonstrated (5.21 (a)) that the degradation kinetics have only a weak dependence on the junction temperature level (for the same stress current, 20 mA), while they are strongly dependent on the stress current level (for the same junction temperature, 53 °C, Figure 6 (b)). In addition, pure thermal stress (carried out at 53 °C, i.e. the same junction temperature reached during dc stress in rows B, E, F in Table 5.1) did not determine a significant degradation of the devices (5.21 (b)). Therefore it is reasonable to think that degradation is not due to a purely thermal effect: results suggest that the degradation process is activated by the flow of current through the active region of the devices, that can activate a sub-threshold defect formation process as described in [54].

5.3.3 Catastrophic degradation

Finally, a number of devices showed catastrophic degradation, with sudden decrease in their optical output. After catastrophic degradation the LEDs behaved as short circuits (Fig. 5.22). By means of failure analysis we have demonstrated that catastrophic failure is due to the generation of short-circuit paths in parallel to the junction (Fig. 5.23). Such paths were found to be localized in correspondence of the borders of the devices: in these regions, the poor definition of the edges of the mesa (presence of tips, see Fig. 5.23) can result in a low robustness to high electrical fields, thus increasing the probability of catastrophic failure of the LEDs even at moderate bias levels.

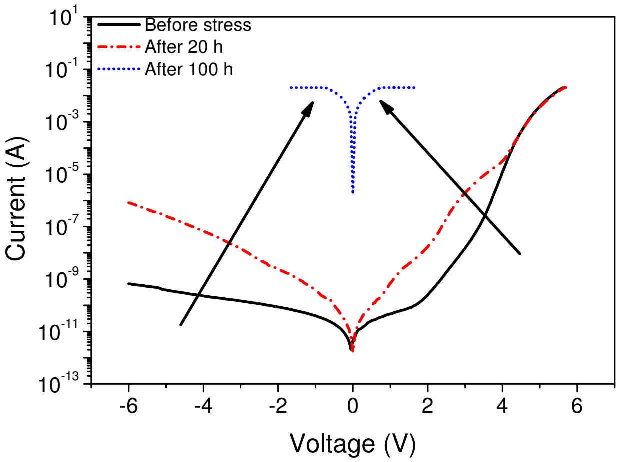

Figure 5.22: current-voltage characteristics measured before and after catastrophic failure on one of the analyzed devices. Catastrophic failure took place after 100 hours of stress.

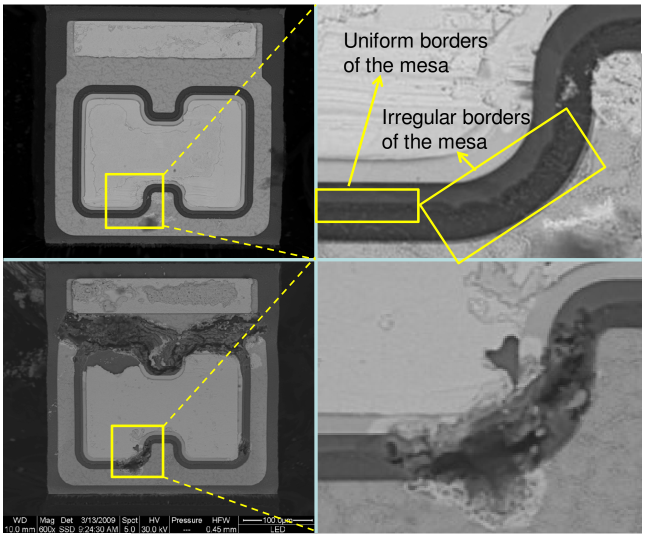

Figure 5.23: SEM images of two analyzed LEDs. Top: untreated LED. Bottom: LED with catastrophic failure. On the right-hand side we report a detail of the damaged area, showing a poor definition of the borders of the mesa.

Chapter 6

Reliability of InGaN Green LEDs

6.1 Introduction

Over the past few years, important results have been reached in the optimization of InGaN-light-emitting diode LED technology. White LEDs (based on blue InGaN LED chips) with efficiencies in excess of 150 lm/W [70] are currently available, and this result has cleared the way for the realization and diffusion of solid state lighting systems. While the technology of blue LEDs is reaching maturity, on the other hand significant research efforts must be done in order to optimize the performance of green LED chips. Such devices have an high indium content in the active region, with consequent low quality and high defectiveness of the multi quantum-well MQW layers: in fact, the miscibility gap of InGaN can induce the creation of indium clusters in the QW region, while the high temperatures used for the growth of the p-type material can lead to the degradation of the InGaN layers of the LEDs [71], [72].

Previous studies have demonstrated that the presence of defects in the active region of InGaN LEDs can limit the efficiency of the devices [73] and influence their electrical characteristics, determining a significant reverse-bias leakage current [74] Furthermore, preliminary reports [38] [75] have also demonstrated that InGaN LEDs can emit light when they are crossed by a reverse current: this phenomenon has been defined as Şbreakdown luminescence,Ť and has been correlated with the recombination of electron-hole pairs. Therefore, the electro-optical characteristics of InGaN LEDs can be strongly influenced by the quality of the material, and leakage current and reverse-bias luminescence can beŮin principleŮa signature of the presence of defects in the active region of the LEDs. However, in order to achieve a deeper understanding of the processes responsible for leakage current conduction and for breakdown luminescence in green LEDs, an accurate analysis of the electrical and optical properties of the devices must be carried out. Recent studies [76], [77], [78] have highlighted that blue and green LEDs grown on sapphire can be particularly susceptible to reverse bias stress and Electro-Static Discharge (ESD) events: the active region of these devices can be highly defective - due to the inherently high dislocation densities, and to the difficulty of growing uniform quantum-wells with high indium content - and this can result in a limited robustness to high electric field and/or reverse-current levels. Despite the importance of this topic, only little information is available on the origin of LED failure under reverse-bias operation and ESD events.

6.2 Study of the reverse conduction and luminescence

6.2.1 Aim

The goal of this work is to describe a combined electrical and optical investigation of the mechanisms responsible for leakage current and for reverse-bias luminescence in green-emitting LEDs. In particular, we show that (i) reversebias conduction is mainly related to tunneling; (ii) leakage current is strongly correlated with the presence of reversebias luminescence; (iii) emission microscopy represents an effective tool for the identification of the reverse-bias conduction paths in QW devices; (iv) breakdown luminescence can be correlated with the recombination of electron-hole pairs in the QW region of the devices. The analysis described in this paper has been carried out by means of currentvoltage- temperature, emission microscopy, electroluminescence EL, and photoluminescence PL measurements.

6.2.2 Experimental Details

The structure of the analyzed samples is based on the ThinGaN process (see [79] for details), that allows a high light extraction efficiency and excellent chip scalability. The devices were grown on a sapphire substrate: after growth, the structures were separated from the substrate and mounted in flip chip configuration on a conductive carrier. The active region structure consisted of a 5 μm n-doped GaN, a multi QW structure, emitting at 532 nm, with GaN barriers, a p-AlGaN electron barrier layer and a p-GaN contact layer. After chip preparation, the samples, with a $290x290\mu m^2$ area, were mounted on a TO18 package, for the subsequent characterization activity. The electrical characteristics of the samples were characterized in a wide temperature range, between 100 and 350K, by means of an Agilent B1500A Semiconductor Device Analyzer. An accurate control of device temperature was obtained by means of a closed-circuit helium cryostat. The breakdown luminescence of the LEDs was analyzed by means of an Hamamatsu PHEMOS 200 Light Emission Microscope (EMMI), while the EL characteristics of the devices were measured by means of a single photon counting technique by using suitable cooled photomultipliers. For the PL measurements we used a 405 nm laser diode as an excitation source, with an excitation power density equal to 50 W/cm2.

6.2.3 Characterization Results

In fig. 6.1, we report the reverse-bias current-voltage I-V curves measured at different temperature levels on one of the analyzed devices: the diagrams are plotted in log-log scale. As can be noticed, the I-V curves follow a power law $I \approx V^n$, with n in the range between 5.3 and 5.9, depending on temperature. A similar soft breakdown behavior was already observed for blue LEDs, and ascribed to the presence of structural defects (such as threading dislocations), in the thin InGaN active layers [80]. Furthermore, the slope of the reverse-bias I-V curves is nearly independent of temperature: this results indicates that the main conduction mechanism responsible for reverse-bias leakage is tunneling, which is a field dependentŮrather than a thermally activatedŮprocess [74], [80].

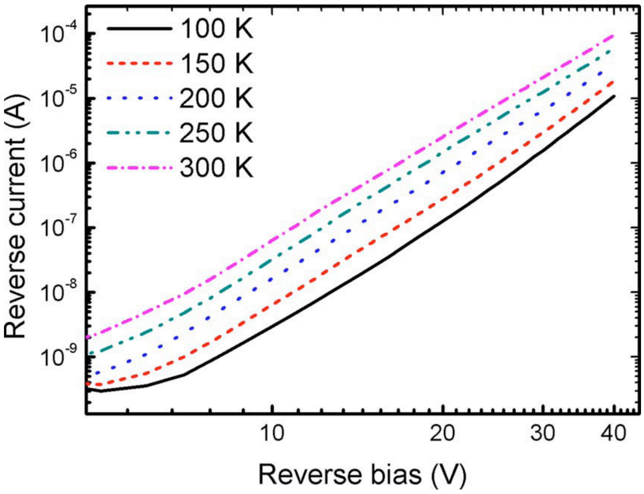

Figure 6.1: Reverse-bias current-voltage measurements carried out at different temperature levels on one of the analyzed devices.

As described above, one of the goals of this research work is to investigate the breakdown luminescence in InGaN-based LEDs. The emission microscopy measurements indicate that the LEDs can emit light when they are crossed by a reverse current. In particular we have found the following: (i) the intensity of breakdown luminescence has a nearly linear dependence on the reverse-bias current level, as presented in Fig. 6.2(a), thus indicating that reverse-bias luminescence is directly correlated with the flow of leakage current across the junction; (ii) the analysis of the reverse-bias light emission profiles indicate that breakdown luminescence is localized in a number of emissive spots, see Fig. 6.2(b).

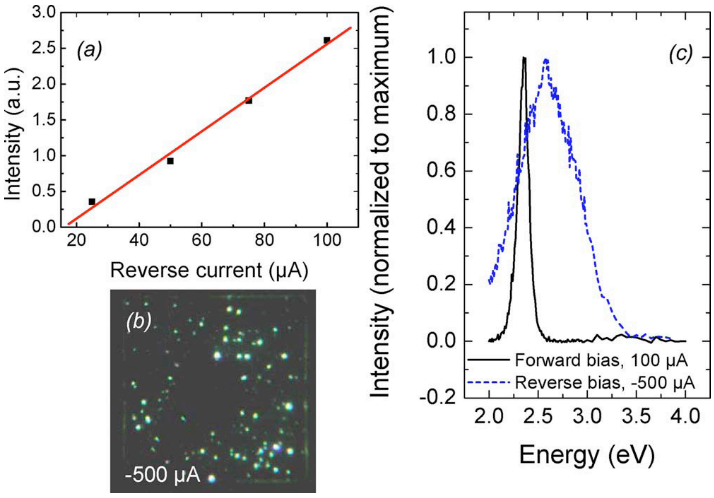

Figure 6.2: (a) Dependence of breakdown luminescence intensity on reverse-bias current. (b) EL micrograph of one sample under reverse bias conditions: several luminous spots are distributed randomly at device surface (at the center of the LED light emission is completely absent due to the presence of the thick bondpad). (c) EL spectra measured under forward and reverse bias on one of the analyzed LEDs

These spots correspond to preferential paths for leakage current conduction, and are possibly correlated with the presence of the structural defects responsible for reverse current [74], [80]. Therefore emission microscopy represents an efficient tool to characterize the distribution of leakage current over the junction area, and for the identification of the defective regions responsible for current conduction. In order to better understand the origin of reverse-bias luminescence, we analyzed the EL spectra of LEDs submitted to reverse-bias. In Fig. 6.2(c) we report the EL spectra measured at -500μA on one of the analyzed samples, and the comparison with the green forward-bias EL spectrum (centered around 2.36 eV). As can be noticed, reverse-bias luminescence has a broad emission band, peaked around 2.58 eV, i.e., in the blue spectral region. This result suggests that the reverse-bias emission originates from the recombination of the carriers injected by tunneling in the QW region. The blueshift of breakdown emission with respect to forward-bias luminescence can be explained by the partial compensation of the quantum confined stark effect (QCSE). In fact, green LEDs have QWs with an high indium content, and suffer from high QCSE, that can determine a significant redshift of the emission wavelength due to the separation of the electron-hole wave functions. This QCSE can be compensated by applying an external negative voltage, as described in [81]. A possible explanation for reverse-bias conduction and emission processes can therefore be the following: under reverse-bias, the presence of structural defects can determine the localized tunneling of charged carriers toward the QWs, with subsequent recombination. The high negative voltage applied to the device can significantly compensate the internal fields, and determine a blueshift of reverse-bias emission with respect to the case of forward-bias. In order to give a more quantitative description of the luminescence behavior of the LEDs under reverse-bias, we have carried out a set of PL measurements at different negative junction voltage levels.

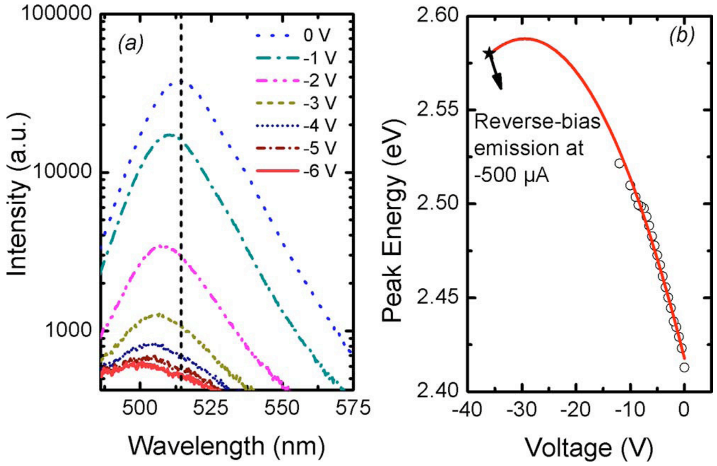

Figure 6.3: (a) PL spectra measured on one of the analyzed LEDs at different bias levels. (b) Variation of the PL emission energy (open circles) with increasing reverse-bias. The black star represents the peak energy of the reverse-bias EL spectrum shown in Fig. 6.2(c). Solid line is a guide to the eye, obtained as a parabolic fit of the experimental data as described in Refs. [82] and [83]

In Fig. 6.3(a) we report the PL spectra measured at different bias levels on one of the analyzed LEDs: as can be noticed, an increase in the reverse bias induces a shift of the emission peak toward higher energies due to the compensation of the internal fields. In Fig. 6.3(b) (open circles) we report the variation of the energy of the PL peak with the applied reverse bias: increasing reverse voltage from 0 to 12 V determines an increase in the emission energy from 2.41 to 2.52 eV. This result indicates that the peak energy of the luminescence peak can be significantly influenced by the applied bias, and supports the hypothesis that the blue shift between reverse-bias emission black star in Fig. 6.3(b) (and forward-bias luminescence can be explained by the compensation of the internal fields. Unfortunately, with increasing reverse bias the overall PL intensity decreases, due to the loss of the photogenerated carriers [84] [85]. As a consequence, PL emission could not be measured for reverse bias levels in excess of 12 V, and close to the voltage levels reached during reverse-bias emission (around -35 V). However, the measurements described in Fig. 6.3 can be sufficient for a first-order evaluation of the entity of the blueshift of the emission wavelength under reverse-bias conditions.

On the basis of a recent report [86], a second hypothesis can be made to explain the blueshift between reverse-bias and forward-bias emission: the GaN-based LEDs analyzed within this work are grown on a sapphire substrate, and therefore have an high density of Threading Dislocations, decorated by V-shaped pits. On the sidewalls of V-shaped pits, the thickness of the QWs can be significantly lower with respect to nondefective regions. For this reason, in proximity of V-pits the effective bandgap of the QWs can be significantly larger with respect to nondefective regions, with subsequent better overlapping f the electron and hole wave functions. Defective regions represent preferential (and localized) paths for tunneling: under reverse-bias, carriers injected by tunneling in the proximity of V-pits can therefore recombine with an higher transition energy with respect to forward-bias emission. Both mechanisms described above (compensation due to negative applied bias and presence of localized defects) can induce a partial compensation of the QCSE, and result in a blueshift between forward and reverse-bias luminescence. Further analysis is being carried out on InGaN material samples and devices, with the aim of distinguishing between the two cited hypothesis for the explanation of the blueshift between reverse and forward-bias luminescence.

6.2.4 Discussion

The results described above suggest that reverse-bias current conduction is generated by the tunneling of charged carriers through structural defects. The carriers injected in the QW region can undergo radiative recombination, thus generating a light emission. The reverse-bias emission spectrum has a peak in the blue spectral region, possibly due to a strong compensation of the internal fields. On the other hand, the large spectral width of the reverse-bias emission can be explained considering (i) that carrier injection and recombination recombination can be assisted by defect states [75] and/or (ii) that the presence of structural defects can induce localized fluctuations in the properties of the QWs. Both these factors can induce a significant variability of the energy of the emitted radiation, and the broadening of the reverse-bias emission peak.

In summary, with this work we have described an analysis of the electrical and optical characteristics of green In-GaN LEDs under reverse-bias. The results of this analysis indicate that tunneling is the most important conduction mechanism responsible for reverse-bias leakage. Furthermore, we have demonstrated that the flow of reverse current can generate a bluish light emission, possibly due to the recombination of carriers in the QW region. Reverse-bias emission is localized on a number of spots, possibly correlated with the presence of preferential paths for leakage current conduction, that can be efficiently identified by means of emission microscopy.

6.3 Reliability study of Green LEDs subjected to reverse bias

The aim of this section is to describe a detailed investigation of the factors that limit the robustness of InGaNbased LEDs towards reverse-bias operation and ESD events. The results described in the following indicate that: (i) reverse current conduction occurs by tunnelling through localized structural defects; (ii) reverse-bias tunnelling determines radiative recombination (reverse-bias luminescence, RBL), due to the injection of carriers in the quantum-well (QW) region; (iii) reverse-bias stress can induce the degradation of the electrical characteristics of the LEDs, due to the generation/propagation of point defects in proximity of preexisting defective regions; (iv) reverse-bias degradation is induced by hot carriers, and the degradation rate is proportional to the stress current level; (v) ESD failures are determined by the shortening of the junction in proximity of one of the structural defects responsible for leakage current conduction.

6.3.1 Experimental Details

The analysis was carried out on green LEDs emitting at 2.33 eV (532 nm), based on multi-quantum well. Device structure consists in a 5 ìm GaN:Si buffer layer grown on sapphire, an active region containing green InGaN/GaNMQWs, a p-AlGaN electron barrier layer and a p-GaN contact layer. A number of devices with uniform characteristics (and an area of 290x290 μm^2) was submitted to reverse-bias stress tests and to reverse-bias ESD events. Reverse-bias stress tests were carried out by applying a constant current or a constant voltage to the devices. During stress time, devices were repeatedly characterized by means of electrical (current-voltage) and optical (emission microscopy, optical power) measurements, in order to achieve information on the degradation process. ESD tests were carried out by a Transmission Line Pulser - Time Domain Reflectometer (TLPTDR): this system can simulate ESD events by generating 100 ns pulses with increasing voltage amplitude. The analysis described within this paper were carried out on a statistically relevant number of samples (>50 samples). Analyzed devices showed reproducible behavior: in the following, we report results obtained on representative samples.

6.3.2 Results of reliability test

Also in this case, as presented in previous part of this chapter we have performed an L-I measurement to measure the optical emission of the LEDs when subjected to reverse bias. In Figure 2 we report the results of emission microscopy measurements carried out before stress on one of the analyzed samples. EMMI measurements indicate that the LEDs can emit light when submitted to reverse-bias. The intensity of Reverse-Bias Luminescence (RBL) was found to be proportional to the reverse current density

(Figure 6.4), and localized on a number of emissive spots randomly distributed on device area (see the inset of Figure 6.4). These spots correspond to the presence of preferential paths responsible for leakage current conduction, correlated to the presence of structural defects [80], [75].

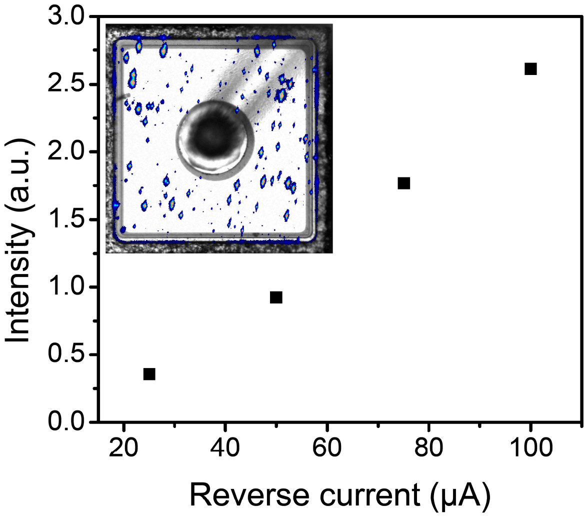

Figure 6.4: Dependence of the intensity of reverse-bias luminescence on the reverse-current level. Inset: false color emission microscopy image, showing the distribution of reverse-bias luminescence on device area

The results described in this section indicate that reverse current conduction does not take place on the whole device area, but only on localized leakage paths. These paths - related to the presence of structural defects - can represent weak regions with respect to reverse-bias stress or ESD events. In fact, under reverse-bias conditions, they can be crossed by a significant reverse current density, that can generate both gradual and catastrophic degradation. This is described in detail in the following.

After the electro-optical characterization described above, devices were submitted to stress under reverse-bias conditions: a set of LEDs was submitted to stress test under constant (negative) current, while another set of samples was submitted to stress test under constant (negative) voltage. In Figure 6.5 we report the reverse-bias emission vs voltage characteristics measured on one of the analyzed devices before and after stress at -1 mA dc (960 minutes).

As can be noticed, stress induced a significant increase in the reverse-bias luminescence signal. Furthermore, an increase in the reverse-current of the LEDs was also detected after stress (see the I-V curves in Figure 6.6). Since both reverse-bias luminescence and reverse current are related to the presence of structural defects, these results suggest that stress determined the generation/propagation of defects in the active layer of the devices.

On the other hand, stress did not significantly modify the optical characteristics of the LEDs in the forward-bias region: in Figure 6.7 we report the (forward bias) Light Output vs Injected Current (L-I) characteristics of one sample, as measured before and after stress at -1 mA dc (960 minutes). No significant optical power degradation can be measured as a consequence of stress. During stress time, reverse current and RBL were found to increase with similar kinetics (Figure 6.8 and 6.9), indicating a correlation.

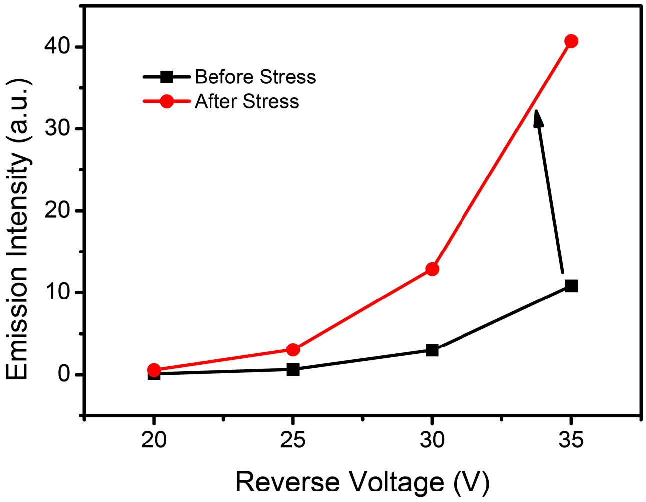

Figure 6.5: Reverse-bias luminescence vs voltage characteristics measured on one of the analyzed samples before and after stress stress at -1 mA dc (960 minutes)

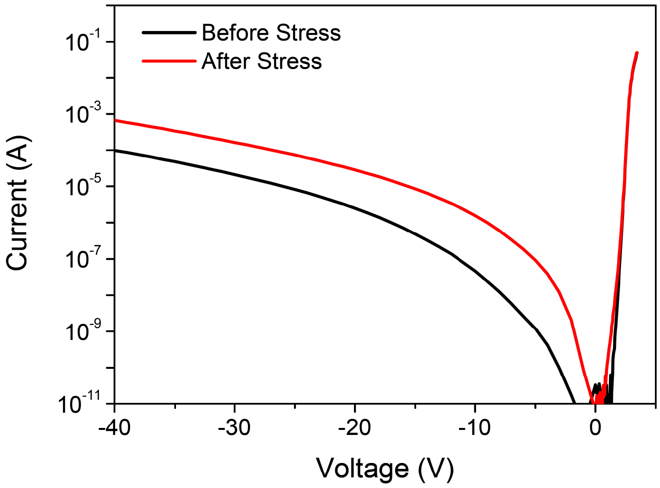

Figure 6.6: Current-voltage characteristics measured on one of the analyzed samples before and after stress at -1 mA dc (960 minutes)

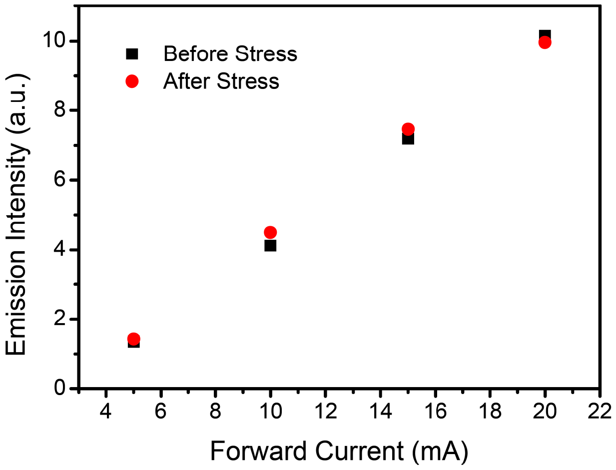

Figure 6.7: Forward-bias optical power vs injected current characteristics measured on one of the analyzed samples, before and after stress at -1 mA dc

Both parameters increased with a t^k dependence on time (see Figure 6.9), with k in the range 0.2-0.3 depending on the analyzed sample.

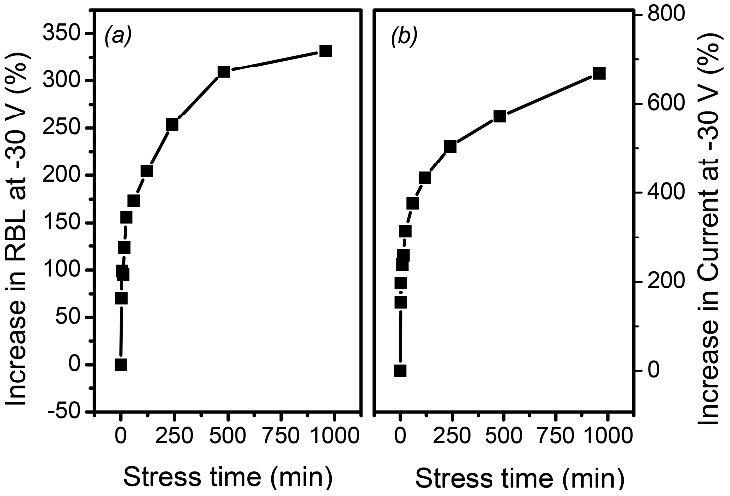

Figure 6.8: (a) increase in reverse-bias luminescence measured (at -30 V) during stress at -1 mA dc, on one of the analyzed samples. (b) increase in reverse current measured (at -30 V) during stress at -1 mA dc, on one of the analyzed samples

The results described above indicate that reverse-bias stress can induce a significant degradation of the electrical and optical characteristics of GaN-based LEDs. Stress mainly influences the reverse-bias characteristics of the devices, and in particular induces an increase in reverse-leakage current, corresponding to a decrease in the breakdown voltage. In order to better understand the origin of the degradation process, and how the degradation kinetics depend on the different driving forces (electric field and reverse-current), we carried out ageing tests under different stress conditions. In particular, a set of LEDs was submitted to stress at constant (negative) voltage, while another set of devices was stressed under constant (negative) current. Several stress

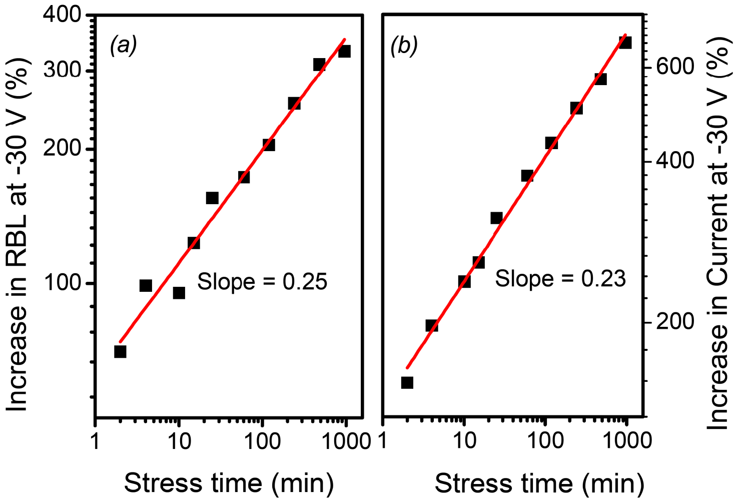

Figure 6.9: (a) increase in reverse-bias luminescence measured (at -30 V) during stress at -1 mA dc, on one of the analyzed samples (log-log scale). (b) increase in reverse-current measured (at -30 V) during stress at -1 mA dc, on one of the analyzed samples (log-log scale)

voltage and current levels were used to study the dependence of the degradation kinetics on the electric field and on the reverse-current level. In Figure 6.10 we report the current vs voltage characteristics measured (before and after stress) on a set of devices aged at different constant voltage levels. As can be noticed, moderate stress voltage levels (V<30 V) did not determine any strong degradation (i.e. any significant increase in reverse-leakage current) of the devices. On the other hand, an increase in the stress voltage beyond 30 V was found to determine a significant increase in the degradation rate. Figure 6.11 reports the current-voltage characteristics measured (before and after stress) on a set of devices aged at different constant current levels.

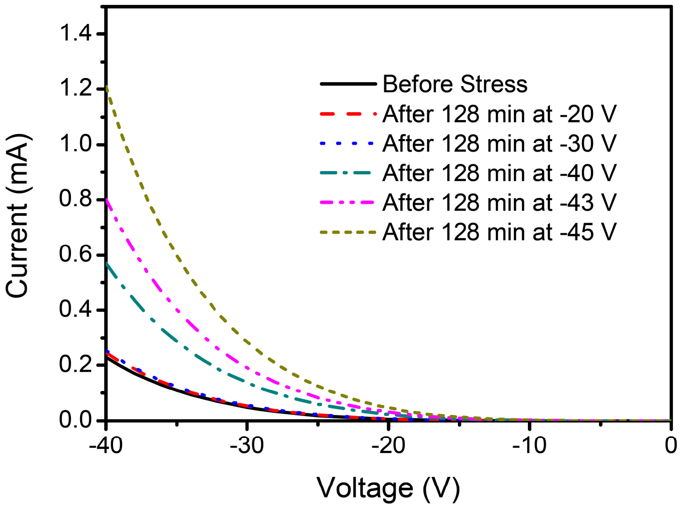

Figure 6.10: current vs voltage characteristics measured before and after stress at different voltage levels

As can be noticed, an increase in stress current level was found to determine an increase in the degradation rate for the analyzed devices. Figure 6.12 reports the de-

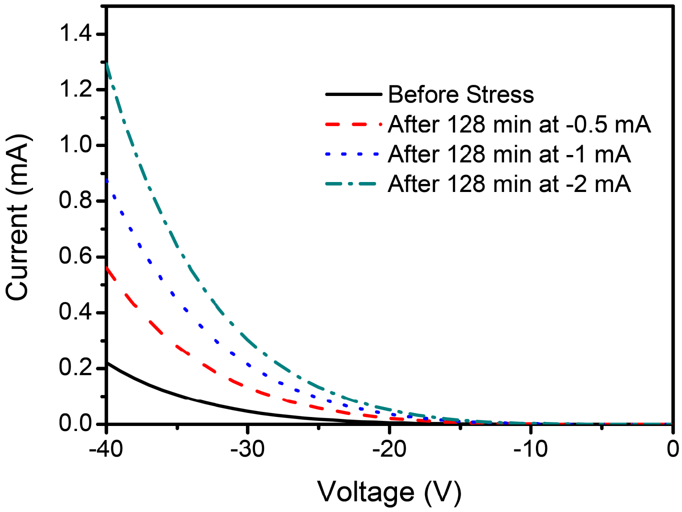

Figure 6.11: current vs voltage characteristics measured before and after stress at different voltage levels

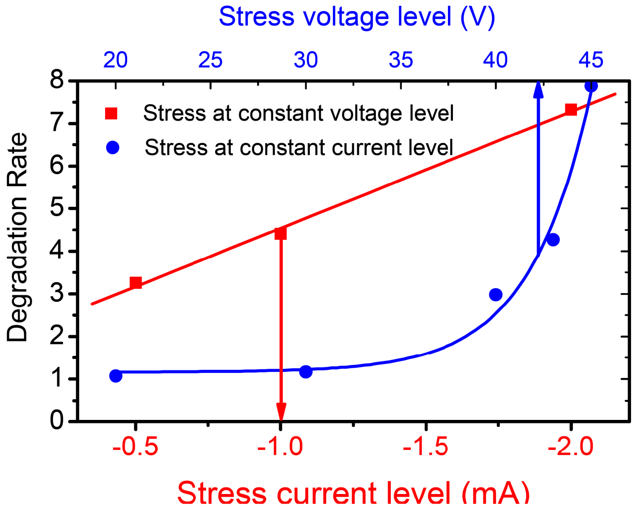

Figure 6.12: current vs voltage characteristics measured before and after stress at different voltage levels

pendence of the degradation rate on the stress voltage and current level: degradation rate is defined as the relative reverse-current increase measured (at -25 V) after stress on samples aged under different conditions. As can be noticed, degradation rate has a superlinear dependence on the stress voltage level, and a linear dependence on the stress current level. This last result suggest that current plays a significant role in determining the degradation process: degradation is correlated to the injection of carriers in the active layer of the LEDs. Under reverse bias conditions, current flows only through localized paths, related to the presence of structural defects. The position of these paths be identified by means of emission microscopy , as shown in Figure 6.4. During stress, injected carriers can be significantly accelerated by the high electric , thus achieving enough energy to interact with the lattice and induce the generation/propagation of point defects. This process can result in an increase in reverse-bias current and luminescence.

6.3.3 Results of ESD tests

As described above, the leakage paths responsible for reverse-current conduction can represent weak regions with respect to reverse-bias stress. Therefore, the presence of these paths can - in principle - influence the robustness of LEDs towards ESD events. In order to evaluate how the devices behave then submitted to ESD events, we have carried out an ESD testing campaign on a large number of LEDs. The ESD robustness tests were carried out by the TLP method, by applying pulses (100 ns duration) with increasing voltage amplitude to the LEDs. For each voltage pulse we have measured (i) the corresponding TLP current (Figure 6.13 (a)) and (ii) the leakage current after the pulse (Figure 6.13 (b)). After ESD failure, LEDs behave as short circuits: ESD damage interests a localized region, as demonstrated by Scanning Electron Microscopy (SEM) investigation (see a sample image in Figure 6.14).

In most of the cases, damaged region is located in correspondence of one of the leaky paths identified (before stress) by emission microscopy. This result suggests that the leakage paths responsible for reverse current conduction constitute weak points with respect to ESD events, since they allow an extremely high current to flow through a small-size path. The presence of structural defects (V-defects, dislocations, ...) can therefore strongly limit the ESD stability of the LEDs. Results indicate that even TLP pulses with (reverse) current smaller that the failure threshold can modify the electrical characteristics of the LEDs: in particular, reverse current levels greater than 10 mA can induce a decrease in the leakage current of the LEDs (Figure 6.13 (b)), corresponding to a certain improvement of the electrical characteristics of the samples. This effect can be possibly due to the annihilation of one or more leakage paths, due to the extremely high current densities injected through small-size defects.

6.3.4 Discussion

We have described an analysis of the origin of the failure of LEDs submitted to reverse-bias stress and ESD robustness tests. We have demonstrated the following relevant results: (i) under reverse-bias, tunneling is the dominant conduction mechanism, and current flows through localized defect-related paths; (ii) reverse-bias stress can induce an increase in the reverse current and RBL of the LEDs, due to the generation/propagation of defects in proximity of pre-existing leakage paths; (iii) reverse-bias

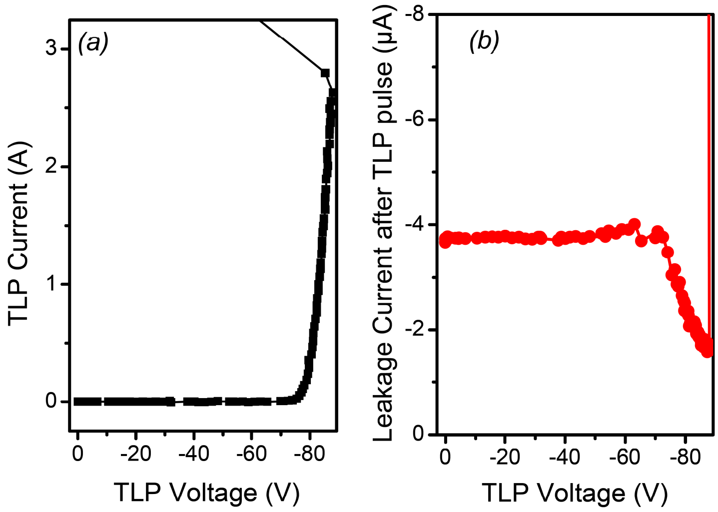

Figure 6.13: (a) I-V curves of one of the analyzed LEDs measured by the TLP setup. The maximum TLP current reached by the LEDs before failure was used as a parameter to define the ESD robustness of the LEDs (for this device it is equal to -2.6 A). (b) leakage current measured after each TLP pulse: TLP current levels greater than 10 mA can induce a decrease in the leakage current of the devices, possibly due to the annihilation of defect-related leakage paths

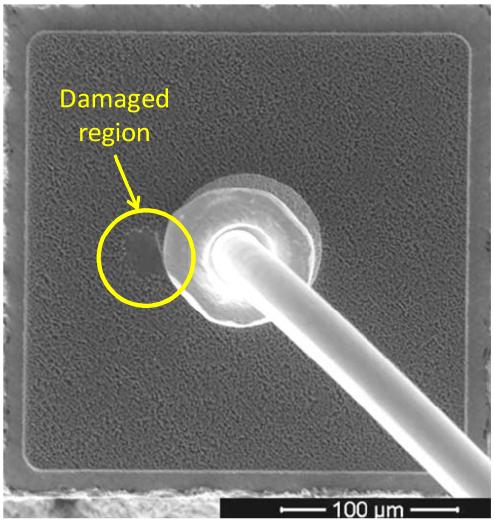

Figure 6.14: SEM image of one LED after ESD failure. The position of the damaged region is highlighted in the figure

degradation is induced by highly accelerated carriers, injected by tunneling in the active region of the LEDs; (iv) the presence of structural defects can strongly limit the ESD robustness of the LEDs. The measurements carried out within this work indicate that a significant improvement of the ESD and reverse-bias robustness of GaN-based LEDs can be obtained only by an accurate control of the defectiveness of the active layer.

Chapter 7

Ageing mechanisms of 420nm GaN HBLED

7.1 Introduction

The development of InGaN/GaN LEDs for solid state general illumination systems has drastically increased performance and reliability of blue and white LEDs. In the last years most of the research efforts have been directed toward phosphor converted white LEDs for general illumination purposes. The properties of GaN based LEDs can be also applied to several different fields: medical, material analysis, biological, etc. Particularly interesting are the effects of light with a spectra located in the so-called actinic wavelengths (around 420nm), they can be absorbed and induce photochemical reactions is several biological compounds like chlorophyll. The properties of solid state lighting can be the ideal solution for application requiring high flux with a nearly monochromatic spectra like in medical and biological environment. However these fields are also the application of LED devices strongly depends on their reliability. While some studies have demonstrated lifetime of several thousands of hours for low power devices [87], the reliability of high power LEDs is still a critical issue. The aim of this work is to describe the ageing mechanisms of high brightness 420nm LEDs subjected to electro-thermal stress. During the stress test several devices characteristic will be monitored in order to describe the nature of the physical process responsible for the ageing modes.

7.2 Experimental details

The analysis has been carried out on InGaN-based HBLEDs emitting at 420 nm. The chip size of the devices is $1070x1070\mu m$ with a p-n junction size of $970x970\mu m$ (see Fig. 7.1) devices are encapsulated in a Luxeon-like package and thermally connected to a 3x5 cm aluminium heatsink. The nominal current is 350mA, with an electrical input power of 1W. Devices have been stressed in a termocontrolled oven with a case temperature (Tc) ranging from 60 to 100řC. Maximum stress duration is equal to 500 hours for the analyzed devices. At each step of the stress tests we have carried out a detailed electrical, optical and capacitive characterization by means of current voltage (I-V) optical power vs input current (L-I) and capacitance vs voltage (C-V) measurements.

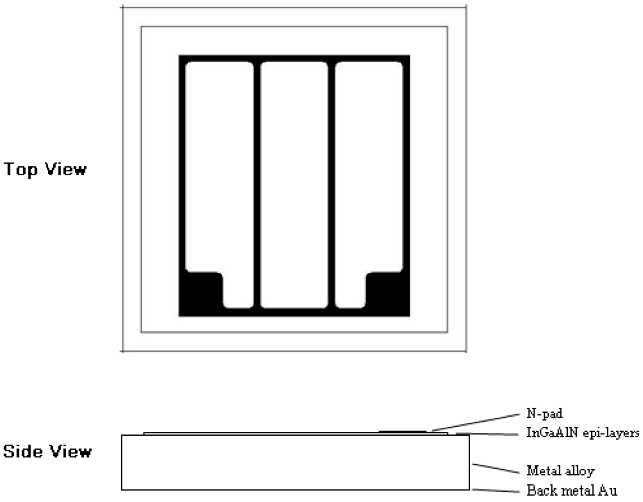

Figure 7.1: LED chip and heatsink layer structure.

7.3 Results and discussion

7.3.1 Fast electrical and capacitive degradation

Electrical and capacitive measurement show a fast decrease of capacitance well correlated with the increase of series resistance of the device (as presented in Fig. 7.2). This phenomenon takes place during the first few hours of device operation and is probably related with a rapid p-type doping decrease related to the flow of carrier through the Mg doped region.

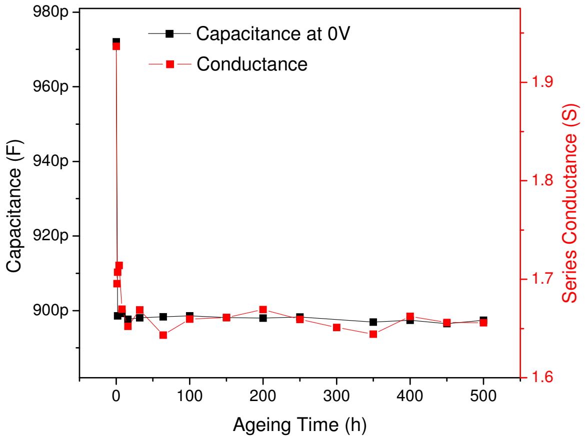

Figure 7.2: Series conductance and capacitance at 0V kinetics.

The Mg passivation has been related by several authors [67] to LED degradation and could easily explain the reduction of available hole carriers and therefore the increase of series resistance well correlated with a decrease of total junction capacitance. The kinetics indicates that this phenomenon is probably caused by the flow of current, takes place in the first hours of operation of the device and then saturates. The thermal stability of the metal contact could also be a cause for the degradation, but considering that: i) the junction temperature (given the thermal resistance of approx. 10 K/W) is well below contact annealing temperature reported by several authors [88], ii) the junction capacitance should not be sensibly affected by the metal contact stability, we tend to refuse this hypothesis. The p-type doping decrease

7.3.2 Optical modification during ageing

The second ageing mode is related to the change of optical characteristics. The log-log and relative LI plot are presented in Fig. 7.3 and 7.4. In the low current zone of log-log LI plot a clear and gradual increase in output power is detected. While in the LI plot normalized to the untreated device is evident that the Op suffers a slight decrease for currents above 10mA, this effect is more evident in the first few hours of ageing, while in the following it nearly gets saturated by the OP increase at low currents.

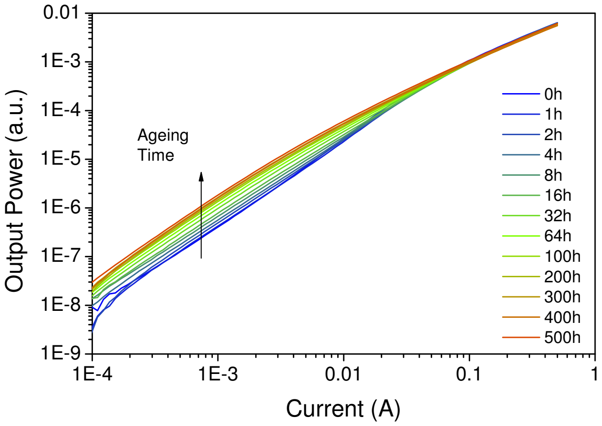

Figure 7.3: Log-log LI plot of LED optical characteristics during ageing. Stress conditions for the sample are 350mA, 60řC.

Our hypothesis is that these two opposite phenomenon can be explained with two different mechanism taking place simultaneously. While the Op decrease at high current levels can be explained with a defect density increase as reported by several author [77], the OP raise requires more analysis to formulate an hypothesis. The low current OP increse is presented in Fig. 7.3 as a semi-rigid OP shift without sensible change in the slope and is detected around the $1mA \approx 0.1A/cm^2$ region. The semirigid increase suggests that this phenomenon is more likely related to a change in the injection efficiency rather than reduction of non radiative recombination. A possible explanation can be the decrease of low forward bias diagonal tunneling (DT) during ageing, caused by a variation of the charge distribution in the quantum wells. As proposed by Yan et al. [89] the carrier tunneling probability P_0 for DT is related to the apparent doping concentration of the QWs, N_I. The DT probability P_0 is reported in 7.1 while β is the term presented in 7.2. A schematical representation of the physical mechanism responsible for Diagonal Tunneling is presented in 7.5.

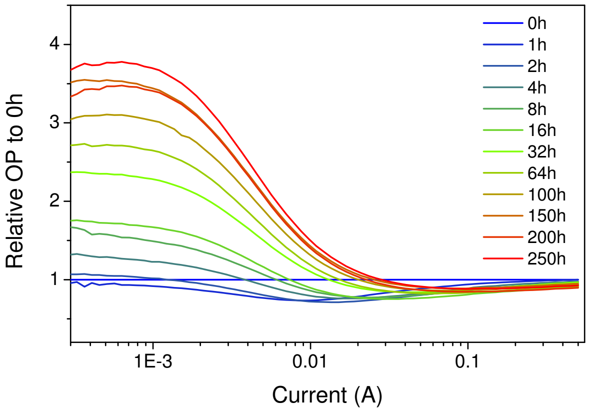

Figure 7.4: Relative OP to untreated during ageing for a device subjected to 350mA, 100řC ageing.

$$P_0 \propto (-\beta E_g) \tag{7.1}$$

$$\beta \approx \frac{8\pi}{3h}\sqrt{\frac{m^*\epsilon_r\epsilon_0}{N_I}} \tag{7.2}$$

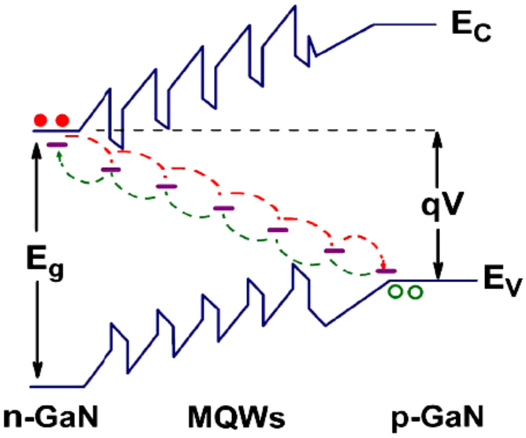

Figure 7.5: Schematical representation of the trap assited Diagonal Tunneling, as proposed by Yan et al. [89].

Where: N_I is the reduced doping level at the SCR edge, and m^* is the effective mass of the carriers. From the IV plot of LED devices we have enlightened 3 different conduction mechanisms: two related to tunneling for applied bias and the diffusion limited by series resistance for higher biases.

Comparing the electrical characteristic before (the plot reports the "After 2h" data to avoid the effects of the already described first ageing mechanism) and after the

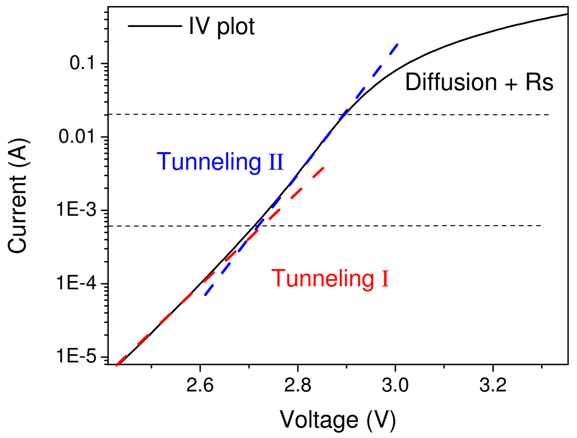

Figure 7.6: Electrical IV characterization, 3 distinct regions are shown on the basis of different conduction mechanism.

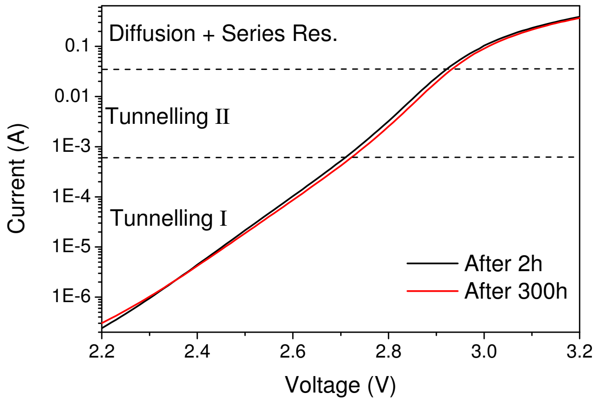

Figure 7.7: Effects of ageing on the IV characteristics of LED.

ageing treatment it is possible to notice a slight decrease of slope in the Tunnelling I region as long as a decrease of current in the Tunnelling II region. This behaviour although minimal could indicate a slight reduction in tunnelling current components at low current bias during degradation. To further investigate this phenomenon we have monitored the change in the quantum well charge profile during ageing by means of CV measurements. Results, presented in Fig. 7.8, indicate a reduction of net charge concentration in the QW during ageing. The change is particularly noticeable in the last quantum well, at around 116 nm from the junction.

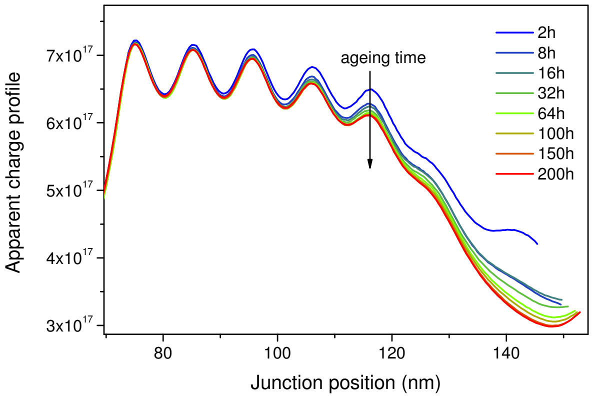

Figure 7.8: Apparent charge profile obtained from CV measurement during ageing.

This behavior could reduce the global NI term in equation 7.2 and therefore decrease the DT probability. The forward current flowing in the junction will therefore more likely be injected in the QWs rather than tunnel through the region. In conclusion the change of the charge profile increases the injection efficiency and therefore both radiative and non radiative recombination rates increasing the total amount of OP emitted in the low current bias region. To support our hypothesis we report in Fig.7.9 the kinetics of the inverse of optical increase at low bias (1mA) and the apparent charge at 116nm from the p-n junction. The plot shows that the two mechanisms evolve with the same kinetic during the ageing indicating a good correlation of the two ageing modes.

These results support the hypothesis that DT could be ascribed as a cause for the reduced injection efficiency in the low current injection regime. The cause for the reduction of charge profile in QW region during the degradation is still not completely clear. In order to better study this ageing process and to understand if the mechanism is thermally activated we have performed the stress tests at different case temperatures (from 60 to 100°C). Results, presented in Fig.6, confirm that the mechanism is driven by the flow of current, rather than by the temperature reached by the devices during operation.

7.3.3 Shunt path generation

Some devices, subjected to 350mA, 100°C ageing treatment, have also shown a steep and sudden decrease of the output OP. LEM microscope analysis (Fig. 7.11)

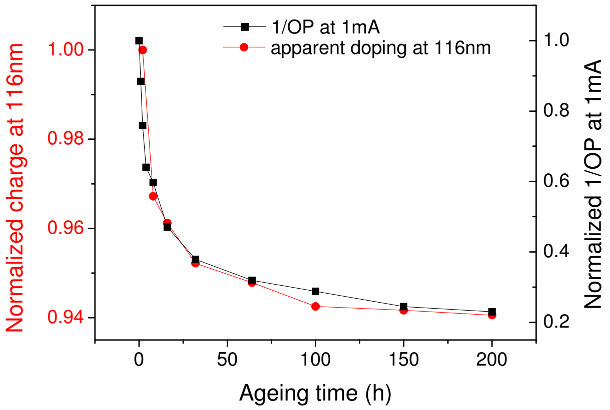

Figure 7.9: Charge at 116nm and 1/OP at kinetics during ageing.

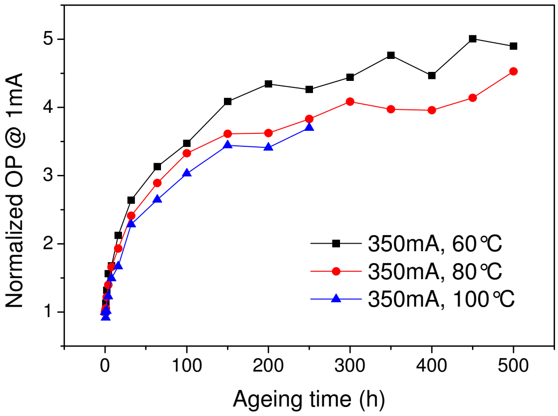

Figure 7.10: Kinetics of the relative increase of optical power in the low current region for different aging temperatures.

have shown the creation of thermal emitting ohmic shunt paths located near the bonding contacts on the device chip. This degradation mechanism could be related to a localized defect in the device structure that act as shunt path when subjected to high temperature. The feed-forward mechanism related to the high density power can generate then a permanent damage.

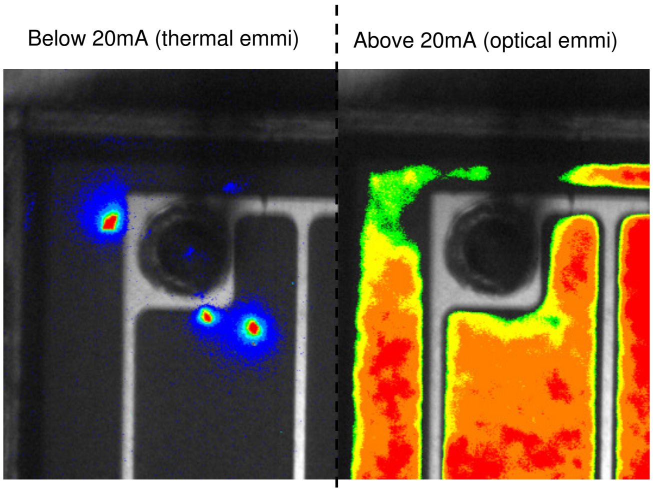

Figure 7.11: Emission maps of LED which suffered steep decrease in OP. On the left the localized thermal emission at 20mA close to the contacts, on the right the optical emission at 30mA with a noticeable localized reduction of emission.

7.4 Discussion

Stress tests carried out on 420nm HBLEDs indicate that different ageing mechanisms take place: i) a fast electrical and capacitive degradation probably related to a Mg passivation; ii) an OP degradation at high injection regime probably related to defect density increase, iii) a gradual OP increase at low injection regime correlated to an apparent charge decrease in QW region and possibly ascribed to a reduction of Diagonal Tunnelling during ageing, iv) a sudden decrease of OP caused by a localized ohmic shunt path.

Chapter 8

Degradation of low flux white LEDs

The recent progresses in the development of high performances Light Emitting Diodes based on Gallium Nitride and yellow phosphors made possible their inclusion in different application fields, like Solid State Lighting, Automotive and Entertainment. Several properties required in the design of lighting applications are available with the LED technology: high efficiency, high Color Rendering Index (CRI), good thermal management and stability during operation. In particular, the key for the replacement of the traditional light sources with LED-based systems is the high reliability, that allows for lifetimes of several tens of kilohours. The more relevant improvements in terms of PC-LEDs performances have been achieved in high-flux devices [90]. Several research labs have recently claimed the demonstration of LEDs that show efficiency values up to 150 lm/W, and similarly the improvements on the phosphors efficiency increased the CRI at values around 90 [91]. Despite these straightforward results, the reliability of power device is still a critical aspect since the high temperature levels reached during operation have a strong impact on the lifetime [[92]. In addition, thereŠs not information available in literature regarding the degradation mechanisms and failure modes that still limit the lifetime of low-flux white LEDs. Thus, the aim of this work is the identification of the failure modes of low-flux commercially available PC-LEDs and the relationship between the flux decay and the chip structure. In order to achieve these results, two families of white LEDs have been submitted to different accelerated aging conditions (electro-thermal stress). The analysis has been carried out with a statistical approach, submitting to stress 80 LEDs for about 1,600 hours. The results have shown both a parametric degradation and several catastrophic failures.

With this work we demonstrated (i) the impact of the temperature on the degradation kinetics, in terms of flux decay and chromatic shift; (ii) the validity of the exponential model of the degradation process for lifetime prediction; (iii) the weak dependence of the stress current level on the degradation; (iv) the effect of the package degradation (lens, phosphors and epoxy stability) on the chromatic properties, (v) the detection of catastrophic failure modes like the chip detachment, thanks to measurement techniques as X-Ray imaging and thermal resistance monitoring during stress.

8.1 Experimental details

Two families of low-flux, commercially available PC-LEDs with PLCC4 package and a nominal current of 30 mA have been chosen. Samples with different chip structure and package composition have been selected. In particular, one family is based of a vertical structure chip (Truncated Inverse Pyramid) on SiC substrate (here called Set A) and the other based on thin film technology on sapphire substrate, with contacts on the surface (Set B). In order to extend the temperature range of the analysis, five different stress conditions have been chosen: (i) 30 mA, 80 °C, (ii) 30 mA, 100 °C, (iii) 50 mA, 80 °C, (iv) 50 mA, 100 °C, and (v) 140 °C, no bias (see Tab. I). For each aging condition a set of 8 samples from Set A and 8 from Set B have been randomly selected, for a total amount of 80 LEDs. The duration of the aging was about 1600 hours for each condition. During the first hour of stress, the forward voltage of each LED has been measured at steady-state conditions. The values collected have been converted to junction temperature, thanks to the Voltage-Temperature characteristics measured before stress (see session III).

Stress conditions	Set A (°C)	Set B (°C)
30 mA, 80 °C	111.7 ± 5.4	115.7 ± 6.3
30 mA, 100 °C	135.8 ± 21.5	144.8 ± 4.1
50 mA, 80 °C	129.4 ± 3.9	141.2 ± 20
50 mA, 100 °C	151.7 ± 9.8	169.6 ± 20.9
140 °C	140	140

Table 8.1: Spontaneous polarization and piezoelectric constant of II-Nitrides

In Tab. 8.1 the average values and the standard deviation of the junction temperature reached under stress among the 8 LEDs per aging condition have been reported. As can be noticed, the wide set of temperatures made possible to investigate in detail the influence of the junction temperature on the degradation. In addition, a pure thermal storage at 140 °C has been performed in order to observe the degradation modes activated only by temperature. Such temperature (140 °C) represents the mean value of the temperature span used for electro-thermal aging. During stress the optical power, the Electro Luminescence (EL) spectra and the Current vs. Voltage (I-V) characteristics of the devices have been monitored. In particular, the EL spectra collected at 30 mA have been used to calculate the luminous flux and the CIE 1931 X and Y chromatic coordinates. At the end of stress, the thermal resistance values have been collected and compared with the values before stress. A failure analysis has been carried out on samples that showed sudden failure, by means of Emission Microscopy and X-Ray imaging.

8.2 Characterization

The samples have been extensively characterized by means of electrical, optical and thermal measurements. The initial optical characterization revealed that the LEDs from Set B emit as twice as LEDs from Set A. In Fig. 8.1 the I-V characteristics of several samples have been reported, together with the averages. Samples from Set A exhibited the highest operating voltage (and thus the highest power dissipation) due to the different technology used for the ohmic contacts. In addition, the curves are more scattered for Set A, indicating a wide binning.

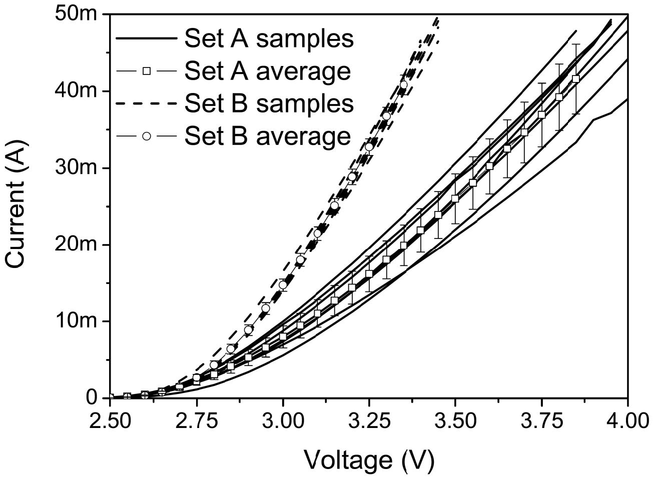

Figure 8.1: I-V characteristics of 10 samples from Set A (solid lines) and Set B (dashed lines).The squares and the circles represent the average values for Set A and Set B devices, respectively.

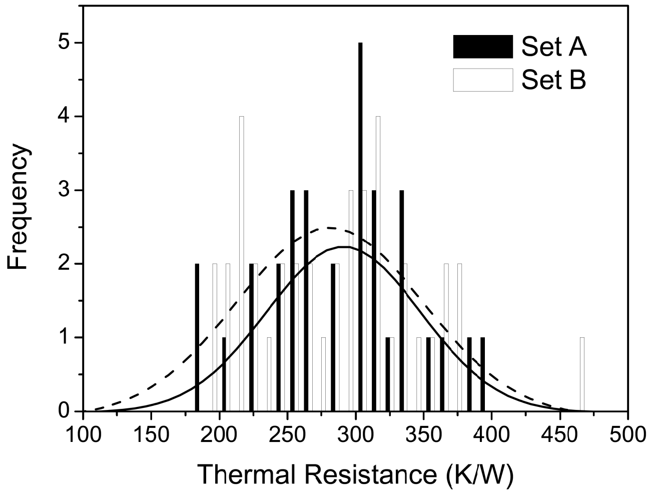

Figure 8.2: Frequency count of thermal resistance of all samples: lines represent the Gaussian fitting of data.

The electrical measurements have been used to extrapolate the thermal resistance (Rth) of each sample. The junction temperature has been estimated by means of the well-known technique of forward voltage [53]. The thermal resistance values calculated for 40 LEDs from the Set A and 40 from Set B have been reported in Fig. 8.2. The Gaussian fit revealed an average Rth value of 289 ± 55 K/W for Set A and 285 ± 61 K/W for Set B, in good agreement with the specifics provided by the manufacturer.

8.3 Results

8.3.1 Luminous degradation

Fig. 8.3 and 8.4 report the average values of the relative luminous flux of samples from Set A and B, respectively. The degradation kinetics have a roughly exponential time dependence and the degradation rate is correlated to the junction temperature during stress (see Tab. 8.1). The comparison of the two sets reveals the highest degradation rate for samples of Set B (see Fig. 8.4). In order to obtain a degradation law, different models have been applied in fitting the experimental data. The 50% of loss in the luminous flux ($L_{50\%}$) has been used as failure criteria. Since the kinetics were affected by instabilities due to experimental errors, the data have been fitted by single-τ exponential function, ignoring the recovery during first hours. This method was also usefull to extrapolate the lifetime data on those LEDs that did not reach the failure criteria. Since the degradation kinetic were clear and uniform for all the devices, the data have not been censored. The first attempt of finding a degradation law was the investigation on the correlation between the Time To Failure (TTF) and the junction temperature. The TTF data have been reported in the Arrhenius Plot. The LEDs from Set B showed the exponential behavior for degradation:

$$L_{50\%}(T) = Aexp\left\{\frac{E_a}{kT}\right\} \tag{8.1}$$

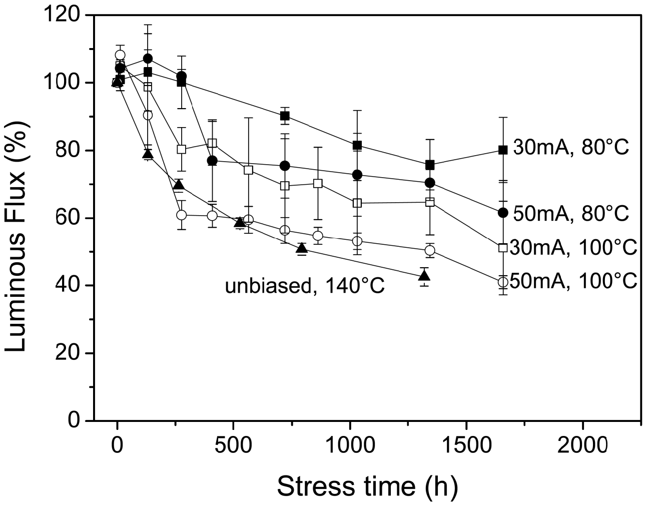

Figure 8.3: Relative Luminous Flux of LEDs from Set A for each aging condition: average values and standard deviations are reported.

This model has been reported together with experimental data in Fig. 4. The activation energy of the process was found to be about Ea = 470 meV, similar to activation energies obtained in other works [93], [94]. It's worth noting that the temperature range of validity of the model is very wide (105 - 190 °C, including the operative range of the device). The extrapolated model is able to make a prevision on LED lifetime. Using a thermal resistance of 300 K/W, a 100 mW value for input electrical power (corresponding to I=30 mA) at RT (T = 300 K), we obtain an estimation of 30.28 kh, with upper and lower predicted response of 71.37 kh and 3.35 kh respectively. On the other

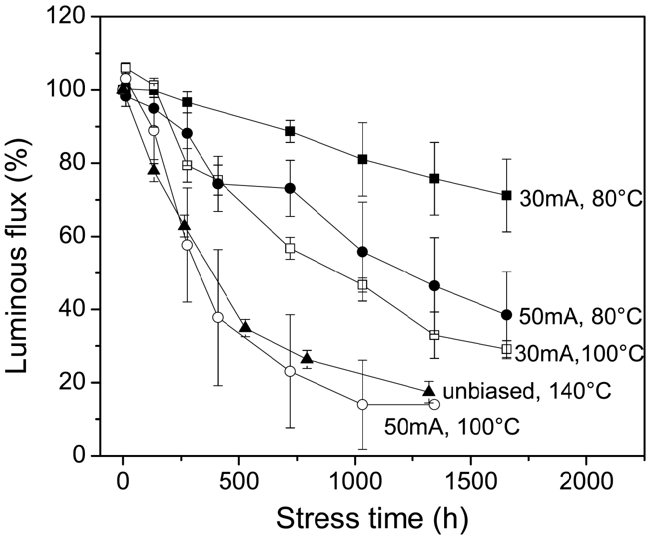

Figure 8.4: Relative Luminous Flux of LEDs from Set B for each aging condition: average values and standard deviations are reported.

hand, the current level was not found to have a detectable impact on degradation rate, as can be noticed looking at the Arrhenius Plot (Fig. 8.5). Similar results cannot be extended to LEDs from Set A since the activation energy is too small and the data too scattered to prove that the degradation process is thermally activated. In order to estimate a MTTF value for these samples, a statistical analysis has been performed by means of the Weibull model, that was earlier used by other authors for lifetime estimation on low flux white LEDs [95]. However, this attempt did not give relevant results, indicating that a long term stress can provide more accuracy in the lifetime estimation analysis. In Fig. 8.3 and 8.4 we reported also the kinetics of the degradation induced by the pure thermal storage at 140 °C. The luminous flux decay was more prominent with respect to samples submitted to the electro-thermal stress at the same junction temperature level (i.e. 30 mA, 100 °C). An attempt of explanation of this phenomenon will be provided afterwards.

8.3.2 Chromatic degradation

The stress induced a chromatic degradation of the LEDs emission. The CIE X and Y chromatic coordinates measured during aging showed a shift in the color space. In particular, LEDs from Set A manifested a shift toward blue emission, while Set B LEDs shifted to yellow emission. In order to better describe the degradation process, the EL spectra of some representative samples from Set A and Set B aged at 140 °C have been reported in Fig. 8.6 and 8.7. Similar results have been detected for electro-thermally aged devices. In the inset graph shows the ratio between the integral of yellow and blue peak.

The degradation mechanisms of the two families can be described. While the LEDs from Set A manifested a decay in yellow and blue peak, more enhanced for yellow (a variation in the ratio of about 40%), the blue peak of LEDs from Set B tended to disappear during stress, and the variation at the end of the stress was around 3000%. Furthemore, the chromatic degradation on electro-thermally aged devices was found to be thermally activated.

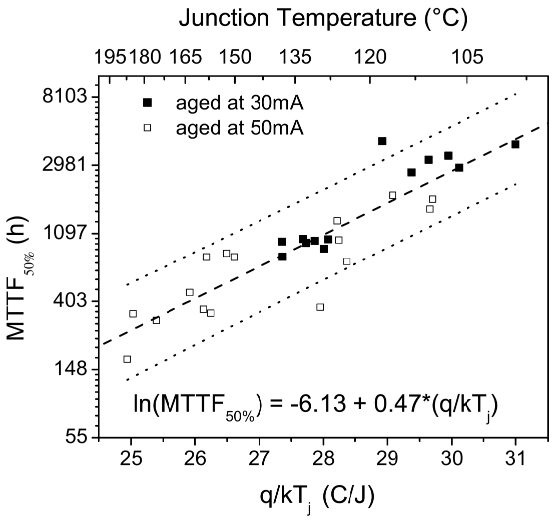

Figure 8.5: Arrhenius plot of the Time To Failure at 50% for all LEDs from Set B submitted to electrical aging. In the plot are also reported the prediction limits, useful for estimation of lifetimes.

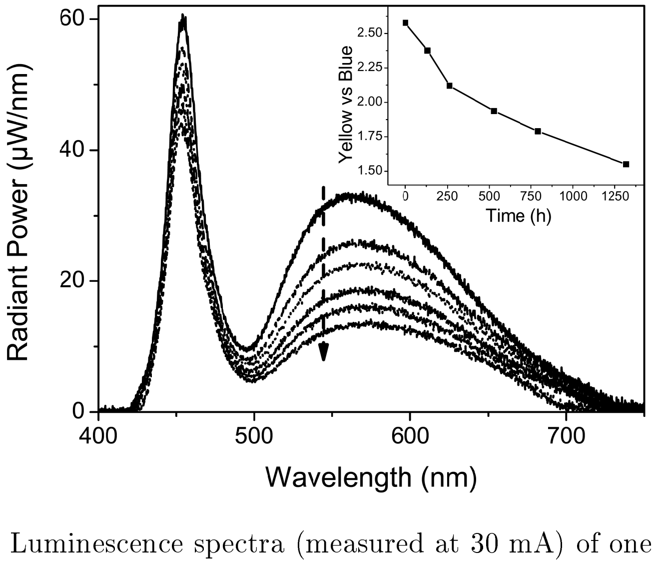

Figure 8.6: Electro Luminescence spectra (measured at 30 mA) of one representative LED from Set A submitted to thermal aging. In inset graph the ratio between Yellow/Blue peak during stress is reported.

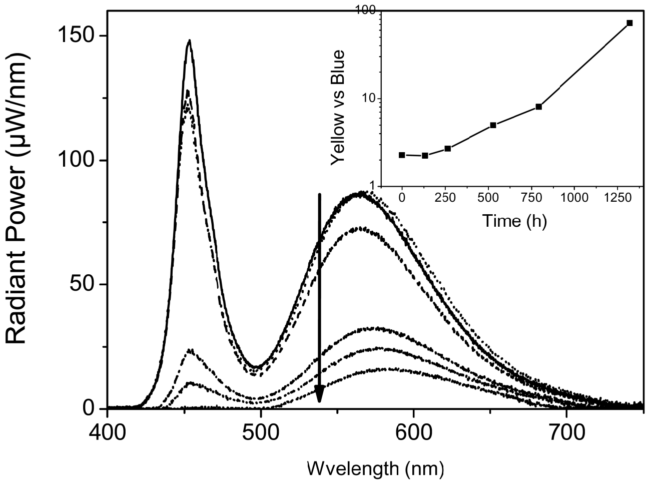

Figure 8.7: Electro Luminescence spectra (measured at 30 mA) of one representative LED from Set B submitted to thermal aging. In inset graph the ratio between Yellow/Blue peak during stress is reported.

8.3.3 Electrical Characterization

Electro-thermal and pure thermal stress did not induce any modification in the electrical behavior of samples, neither in the low and reverse voltage region (indicating that the stress did not generate/propagate defects), nor in the forward voltage region (indicating a good stability of the ohmic contacts). However, several samples from Set A submitted to harsher conditions have shown a current increase in the low forward voltage region: an identification of the degradation process will be provided in the Failure Analysis section. In addition, the thermal resistance of the aged devices has been measured and compared to the value before stress. While the thermal resistance of the LEDs from Set A remained unchanged during stress, an increase was detected in thermal resistance of LEDs from Set B. In Fig. 8.8 the thermal resistance values for several aging conditions of Set B LEDs have been reported. As can be noticed, the harsher stress conditions induced an increase in thermal resistance. The degradation process introduces a positive feedback: the higher the temperature is, the higher will be the increase of thermal resistance and so on. The temperature increase detected was confirmed by a decrease in luminous efficiency at higher current levels for these LEDs. An explanation of this degradation mechanism will be provided in the next section.

8.3.4 Degradation Mechanism identification

In both the families A and B we may infer that the degradation mechanism associated with the worsening of the chromatic properties is related to the package. This hypothesis is based on the proven reliability of InGaN blue LEDs when aged at the temperature and current levels used for stress [67].

Furthermore, excluding the instability of the YAG phosphors [92], [96] one have to consider the instability of the epoxy composing (i) the lens and (ii) the whole package. The transmittance of the epoxy of the lens could degrade during aging due to high temperatures and act as a filter. On the other hand, it was observed that the white

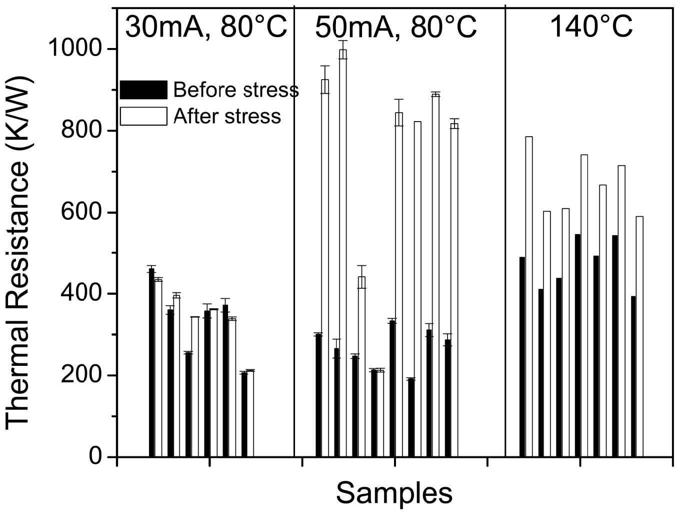

Figure 8.8: Thermal resistance values measured before and after stress of LEDs from Set B for different aging conditions.

epoxy of the package darkened during aging, with a worsening of the reflectivity that may impact on chromatic properties [97], [69].

The more enhanced thermally activated degradation process of LEDs from Set B suggests the use of different and more unstable material for the encapsulation. Since the activation energy is higher than the energy of LEDs of Set A, there is a correlation between temperature distribution and the impact on degradation.

8.4 Failure analysis

Several samples from Set A and B failed during stress. Two different failure analysis techniques have been employed in order to identify the failure modes: the Emission Microscopy and the X-ray imaging.

8.4.1 Emission Microscope analysis

The analysis was performed both on samples from Set A and Set B, but interesting results have been obtained only for failed LEDs from Set A that became short circuits during stress. Several samples submitted to harsher stress conditions manifested a current increase in the low voltage region. For instance, the I-V characteristics of one LEDs submitted to aging at I = 50mA, T = 100 °C have been reported in Fig. 8.9. This sample failed after first 276 hours: it was removed from the package by etching and observed by means of SEM imaging. Several holes with a few microns diameter have been found on the surface, more concentrated around the edge of the contact. The holes detection suggested the hypothesis that they were generated by thermo-electrically activated migration of already present dislocations. The dislocations growth can be transversal to the junction plane, implying a shortening of the junction itself.

This hypothesis was confirmed by the Emission Microscopy image reported in Fig. 8.10. The particular of the emission image of a failed sample biased at -5 mA has been reported. The false-color spots are localized mainly around the contact area (in

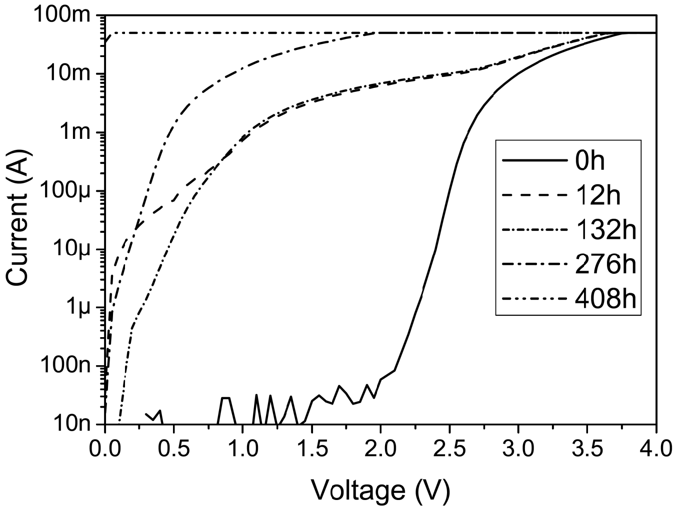

Figure 8.9: I-V characteristics of one LED of Set A that failed in early stage of stress at 50 mA, 100 °C

the figure one can notice the contact finger). The hypothesis of shortening path is in good agreement with the increase of leakage current observed. When the current density flowing through these dislocations is higher enough, the junction is shortened and the devices does not emit any more. These shortening path could be broken by submitting the device to high current levels (above nominal values): in that case the devices return to emit, but the leakage current persists. This mechanism has not been detected in LEDs from Set B, due to the different pad configuration (better current spreading) and to a lower dislocation density (different epitaxy process, confirmed by a higher luminous efficacy and a lower forward voltage).

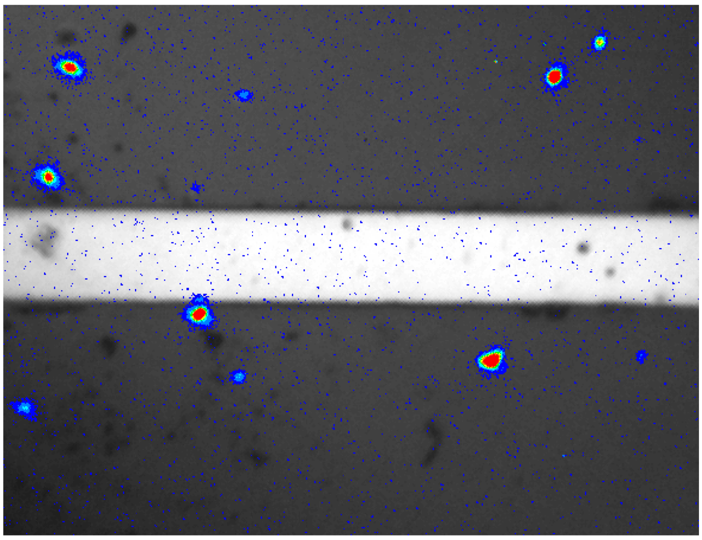

Figure 8.10: False colors emission microscope image of failed sample from Set A biased at -5 mA. The plot reports the particular of the contact finger. The shortening path are recognizable as light spots.

8.4.2 X Ray analysis

At the end of the aging, the failure analysis was performed on samples that showed a total failure. The failed devices (aged at 50 mA, 80 °C) have been submitted to X-ray imaging, and compared to untreated devices. The analysis showed that the entire layer containing the chip, the bonding wires and phosphors of aged sample is detached from the aluminum layer below. A schematic explanation of the detachment process is reported in Fig. 8.11. The layer is in thermal and electrical contact with the LED and the detachment implies an increase in the operating temperature: this hypothesis was confirmed by thermal resistance increase reported in Fig. 8.10 Since the thermal resistance increase is thermally activated, the physical process of encapsulation detachment was ascribed to the high temperature levels. In particular, the mismatching of the thermal expansion coefficients of the materials composing the phosphors layer and the package may be responsible for detachment. In addition to the thermal resistance increase, almost all samples aged at 50 mA and 100 °C failed at about 1000 hours. This failure was ascribed to the electrical detachment of the bonding wire, caused by the strong displacement of the encapsulation from the electrical pad of the package. This is a confirmation of the role of the package in the degradation and failure of devices from Set B.

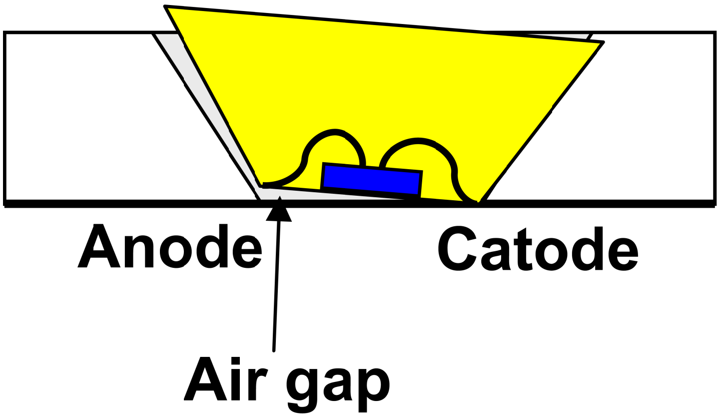

Figure 8.11: Schematic diagram of the failure process detected by means of X-ray imaging on several LEDs of Set B stressed at 50 mA, 80 °C.

8.5 Discussion of the results

An in-depth electro-optical-thermal characterization and accelerated lifetime testing on different families of low-flux PC-LEDs have been carried out on a large set of samples. The initial characterization pointed out the differences in terms of performances between the two different designs of LED structure. During the electro-thermal aging the optical, electrical and thermal properties have been monitored in order to find a correlation among the different failure modes. A reliability analysis based on results obtained during the stress provided the estimation of an exponential degradation model, suitable for the lifetime prediction. In particular the work provided several results: (i) the degradation is correlated with the structure and the composition of the package, (ii) the output decay is thermally activated, (iii) the not-optimized matching between different materials composing the package can strongly affects the device reliability, (iv) the electrical treatment can induce catastrophic failures depending on the chip structure. In addition, several techniques for failure analysis as the Emission Microscopy and X-ray imaging have been successfully used.

Chapter 9

ZnO transparent contact LED

The work reported in this chapter is the result of the PhD visiting period of the Candidate carried out at EPFL - Ecole Politechnique Federale de Lausanne at the Laboratory of advanced semiconductors for photonics and electronic - LASPE. The period has been aimed to the comprehension of the growth and processing techniques necessary for the development of next generation GaN Light Emitting Devices. During this period several works have been carried out by the candidate to fully comprehend this field; in the following general overview of LED manufactoring will be described as long as the more interesting achieved results.

9.1 Introduction

The development of new LED devices and the continuous research for better performances has pushed the research work in two different fields: (i) Increase of the internal efficiency, and (ii) increase of Extraction efficiency. While the first is mainly relate to the quality of materials and the different growth conditions, the extraction efficiency is instead related to different factor, from the layer thickness, to processing and packaging of the produced LED chip. Different processing procedures and materials have been recently used to increase the extraction efficiency [26]. A method adopted to increase the extraction efficiency has been the use of different semi-transparent superficial contacts that allow the extraction of the light from above the sample [98] by means of special thin film of metals, the most used is Ni/Au. One of the principal method adopted has been the roughening of the emissive surface of the LED itself. With the surface roughening it is possible to reduce the amount of light reflected back to the active region, and thus increase the amount of extracted light [99]. The surface roughening can be also performed with a specific pattern, the research carried out in this field has leaded to the development of Photonic crystals, [100] where the surface of the device is specifically structured with nanometric air spaces, and have a photonic effected on the LED emitted light thus increasing extraction. The combination of a transparent contact (by means of a TCO-Transparent Conductive Oxide) and roughness patterning has been used to further increase the extraction efficiency, unfortunately this process require intermediate steps for the patterning of the TCO, that increase costs and manufacturing time. With this work we have used LP-CVD, low pressure Chemical vapour Deposition, performed at the University of Neuchatel (CH) to deposit ZnO over the GaN wafer. This techniques allow the deposition of a thin ZnO layer that can be used as a TCO for the generation of contacts over the sample. The interesting feature of LP-CVD is the deposition of a rough oxide that can allow the theoretical increase of the extraction efficiency from the device.

9.2 Processing of GaN devices

9.2.1 Surface preparation

Before starting the processing, and in any case between two different processing steps it is fundamental to properly prepare and clean the surface of the sample. Every time the sample surface is in contact with air, the formation of oxides and the deposition of chemical compound must be considered. It is specifically important before the deposition of metal contact, which are very sensitive to oxides and other impurities, to clean the surface in order to obtain good electrical performances. Different cleaning techniques can be adopted, varying with the processing step:

Initial and prior to metallization cleaning

- Ultrasonic bath for 5 minutes at moderate power in Acetone
- Wash with Acetone, then Methanol and finally Isopropanol (AMI) solvants
- Dry with compressed N_2 flux

Standard cleaning procedure

- 5 minutes at 60W Oxygen plasma (removes organic impurities)
- 30 seconds in $HCl : H_2O$ 1:1 followed by 1 minute H_2O rinse
- 30 seconds in BHF (buffered hydrofluoric acid) followed by 1 minute H_2O rinse
- Dry with compressed N_2 flux

9.2.2 Photolithography

Photolithography is the process step used to define a geometric pattern on the wafer in order to create the device structure. It is based on a photosensitive organic polymer called "photoresist". The photoresist deposition is obtained by mean of a spinner, the sample is placed on a rotating base, where the photoresist is deposited in liquid form and then "spinned"to create an homogeneous photoresist film. The thickness depend on the spinning velocity. The photoresist used in this work is AZ5214: spinning speed of 5200 rpm will give a 1.4 μm film thickness. To increase the adesion of AZ5214 it has been used Hexamethil-disilizane (HMDS) as an adhesion promoter prior to the deposition of the photoresist. The resist is the solidified by means of a thermal treatment at 90 °C for 5 minutes. To define the geometrical pattern the photoresist is selectively exposed to UV light by means of a specific chrome mask deposited on a quartz window. The alignment is obtained with a mask aligner. When the photoresist is exposed to UV light the chemical structure of the polymer changes [101] [102] and it offer different resistance to a special solving solution called developer. The developer used for EZ5214 is MF-319. The procedure to deposit the photoresist is reported in the folloring:

- Spin at 5000 rpm for 30 seconds uder N_2 flow;
- Spin at 5000 rpm with HMDS for 30 seconds;
- Spin at 5000 rpm with AZ5214 for 30 seconds;
- "‘pre-bake"’ at 90 °C for 5 minutes.

With EZ5214 it is possible to obtain both positive and negative photolithography. A rapid thermal treatment is able to change the polymeric structure of the photoresist, thus reversing the mask image. The positive process procedure is reported below:

- Fix the mask in the mask-aligner, place the wafer and perform alignment;
- Expose to UV for 3.5 seconds (this is the reference time for a Photoresist thickness of 1.4 μm);
- Remove the sample from the mask aligner;
- Develop the sample in MF-319 for 45 seconds;
- Rinse with H_2O and dry.

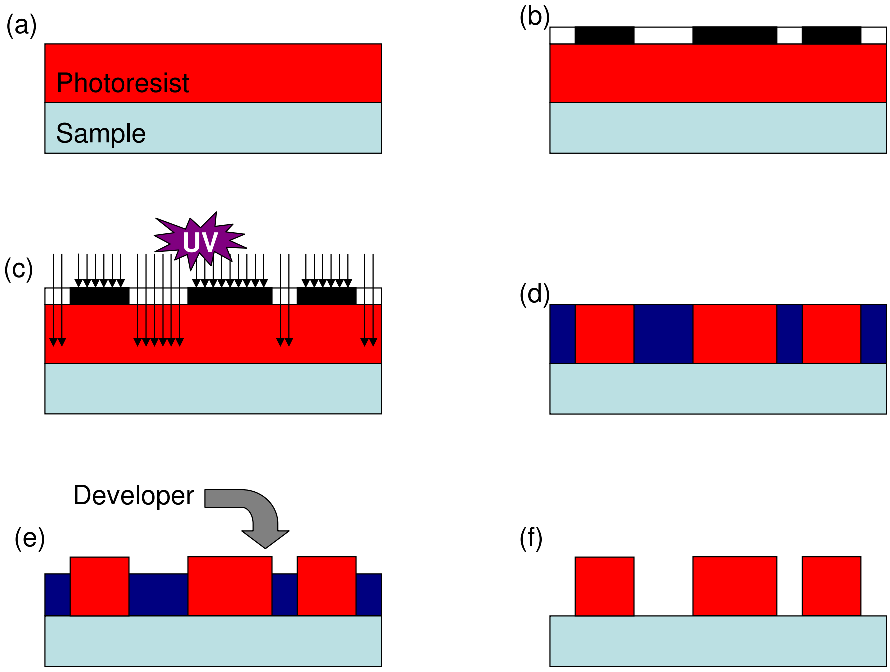

Figure 9.1: Positive lithography process: (a) sample with spinned photoresist, (b) mask alignement, (c) UV exposition, (d) Exposition result, (e) development, (f) photolitography completed.

The negative process, reported in the following, uses an intermediate step where the polymerization is inverted:

- Fix the mask in the mask-aligner, place the wafer and perform alignment;
- Expose to UV for 1.5 seconds;
- Remove the sample from the mask aligner;
- perform polymerization inversion with a thermal treatment at 115 °C for 2 minutes;
- Expose to UV for 40 seconds without mask;
- Develop the sample in MF-319 for 45 seconds;
- Rinse with H_2O and dry.

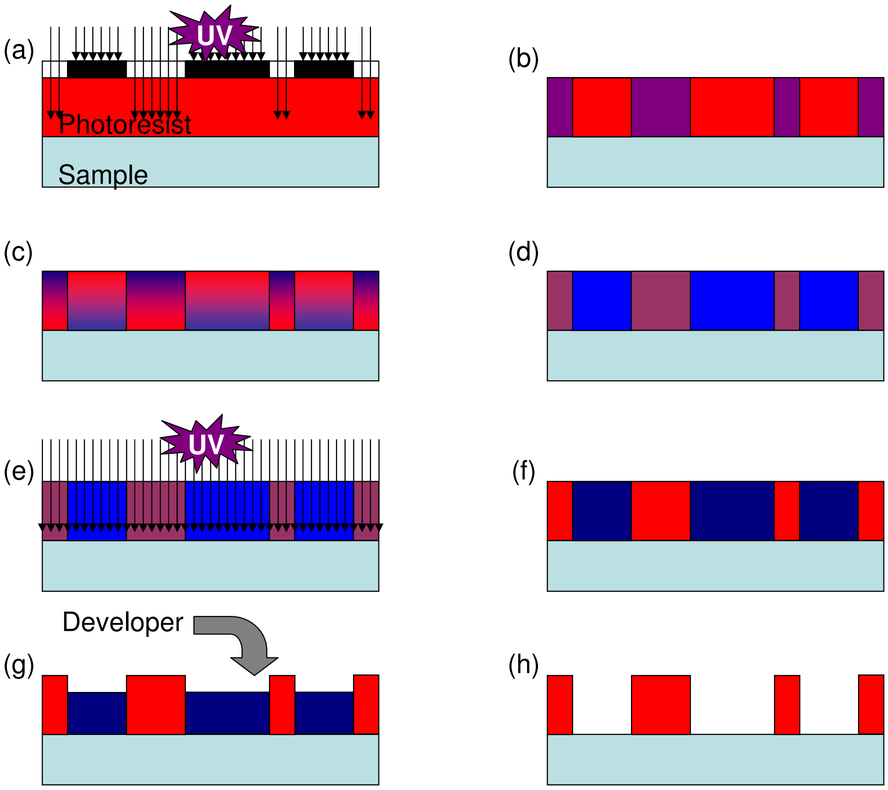

Figure 9.2: Positive lithography process: (a) UV exposition, (b) first exposition result, (c) Thermal tratment, (d) image reversed, (e) UV exposition, (f) second exposition result, (g) development, (h) completed.

9.2.3 Metal deposition

The metal deposition is fundamental to place electrical contacts on the wafer and obtain a device measurable by means of a semiconductor parameter analyzer. The metal deposition is achieved by means of an E-BEAM machine: the sample is placed in a low pressure chamber, where an electron beam is focused on a melting pot containing a highly purified metal species, the metal, heated to the sublimation point, evaporates thus creating a metallic film over the sample (see Fig. 9.3). The chamber is equipped with a turning multiple melting pot system that allow the deposition of different metals without removing the substrate from the chamber. To measure the thickness of the deposited material a quartz oscillator is placed close to the sample, the material deposited over the quartz varies the oscillating frequency and determine the metallic thickness. To obtain a good conduction over the GaN it is necessary to deposit a metal with the correct work function in order to achieve a good ohmic contact.

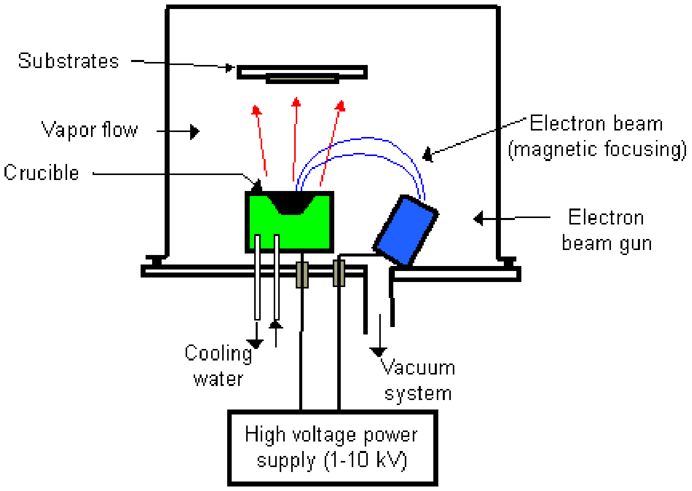

Figure 9.3: Example of an E-Beam deposition chamber.

p-GaN contact Resistance of p-GaN ohmic contact has a high resistivity value of $10^{-2}\Omega cm 10^{-4}\Omega cm$. The problem consist in high GaN bandgap and electron affinity ($\chi = 4.1eV$), which requires high work function (Φ_m) metals in order to achieve low barrier $\Phi_B = \Phi_M - (E_G + \chi)$. Several expedient have been developed in order to build up a low resistivity contact: a moderate-high doping concentration of GaN and an accurate surface treatment to remove possible oxide formations. Pd is the most used for the p-GaN contact which is generally followed by multi metal layers of Nichel/Gold, Platinum and Tungsten, Gold is generally the final metal deposited to avoid oxidation.

n-GaN contact Several author have worked on low resistance ohmic contact on n-GaN [103], [98]; Fan et al. [104] have developed a multilayer technology to create an ohmic contact on n-GaN with a low resistance of $10^{-7}\Omega cm$. The GaN layer is a n-GaN doped with Silicon with density of $1x10^17 \div 510^17 cm^{-3}$. A multi metal layer Ti/Al/Ni/Au is deposited with thickness of 150/2200/400/500 Årespectively. Following a rapid thermal annealing at 900 °C for 30s establish a reaction between multilayer element generating TiAl AuNi, which give robustness and stability even at high temperature, avoiding electromigration. The ohmic contact created is based on tunneling transport (see Fig. 9.4). Due to high efficiency of this contact, most ohmic contact on n-GaN are based on Titanium/Aluminium multilayer metalization. The contact used for the processing during the Thesis has been mostly Ti/Al/Ti/Au which ensures the optimal tunneling conditions.

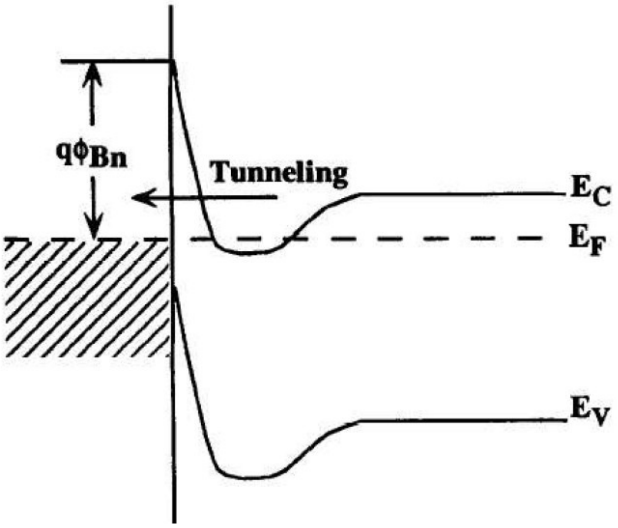

Figure 9.4: Band diagram of tunneling metal-semiconductor contact on high n doped GaN.

Lift-off Lift off procedure is an alternative technique opposed to standard etching technique for the deposition of metal film patterns [105]. This technique is used to simplify and speed up the processing, since less steps are required. While the standard etching technique protects some area of the deposited metal with the photoresist and the remove the unprotected metal zones by means of wet or dry etching, lift-off works the opposite way. The photoresist masking is performed prior to the deposition of the metal thus allowing only some area of the wafer to be covered by the metal film. When the resist is removed the material on the top is lifted-off and washed together with the sacrificial layer below. This technique does not require the etching phase, therefore it is faster and suitable for wafer that might be damaged by such step. The disadvantages are: (i) retention (i.e. a not complete detach of the not required areas), (ii) ears (i.e. metal residue on the sidewalls), (iii) redeposition. A comparison between etching and lift-off microtechionques is reported in Fig. 9.5. As can be noticed the lift-off technique is a negative techniques, as a result to obtain the same final result of the etching method it must be adopted in conjunction with negative photolithography.

9.2.4 PECVD dielectric deposition

The dielectric deposition is necessary to create non conductive layer on the surface of the device, they can be useful for example for the confinement of current in the case of Laser Diode structures (SiO_2, [106]) or for the passivation of surface dandling bonds (Si_3N_4, [107]). To deposit SiO_2 and Si_3N_4 it is used Plasma Enhanced Chemical Vapor Deposition, PECVD, as presented by [108]. The process is based on plasma-activated gaseous precursors that react on the surface of the heated sample and generate an homogeneous dielectric film. The growth rate varies with the power of the generated plasma, standard growth values for a plasma of 40W are 40 nm/min for SiO_2 and 25 nm/min for Si_3N_4.

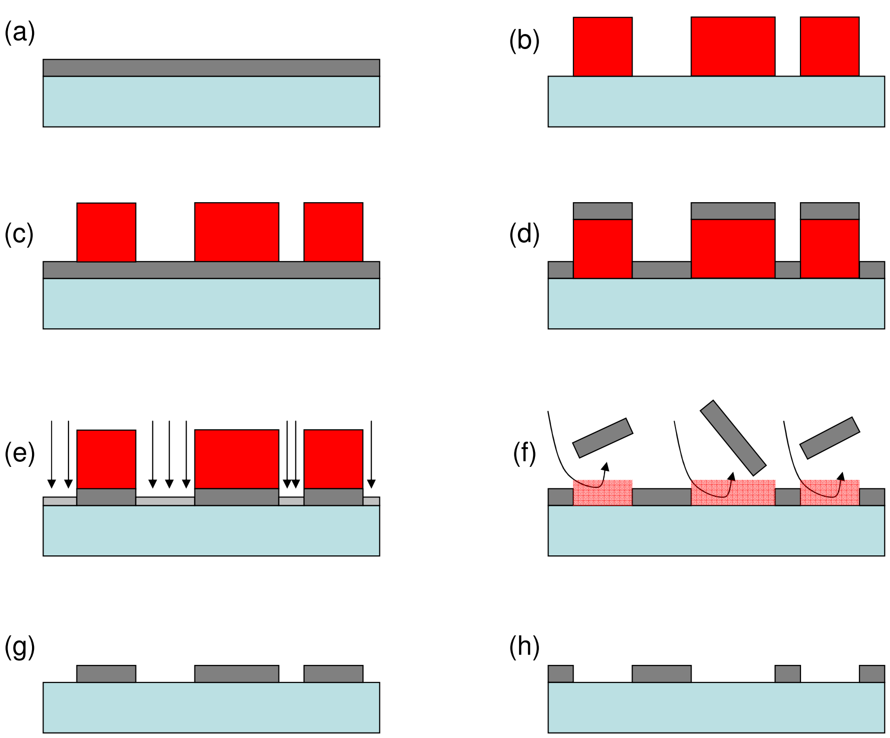

Figure 9.5: Etching (left): (a) metal deposition, (b) making, (c) etching, (d) resist removal and final step; Lift off (right): (e) masking, (f) metal deposition, (g) resist removal, (h) final result.

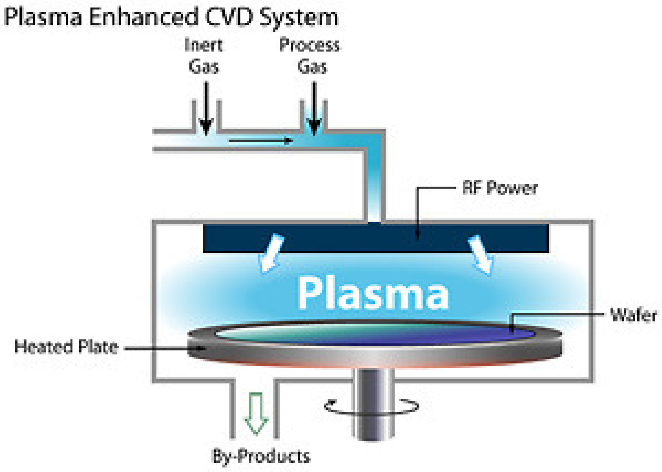

Figure 9.6: structure of a PECVD reactor, courtesy of dowcorning corp.

9.2.5 Etching

Etching is used for the removal of material (semiconductor, resist, dielectric, metal) during the process. The first important aspect to consider is the difference between wet and dry etching. The wet etching is based on a chemical reaction that take place on the surface of the sample by means of a liquid etchant. Wet etching is isotropic (i.e. occurs in all directions) and the etching rate depends on the etchant solution and on the material to be etched. Dry etching is a physical and chemical carving that take place in a plasma chamber or by ion beam.

Ethcing of GaN can be obtained with wet etching by means of KOH solutions [109], [110]. Unfortunately the wet etching of GaN has proved to be problematic and is not completely isotropic, but follow some preferential paths on the crystalline structure [111]. The dry etching of GaN is instead achieved with several methods [112]. The technique used during the thesis period has been the Inductively Coupled Plasma - ICP using Cl_2 and Ar [113]. ICP work with two different RF fields, the first one generate the plasma, while the second accelerate the plasma toward the sample which is placed in different part of the reactor. This technique allow a better control of the process since the plasma generation is independent from the accelerating RF field, thus allowing an optimal balance between chemical and mechanical etching action. The etching thickness can be monitored in-situ by means of a reflectometer.

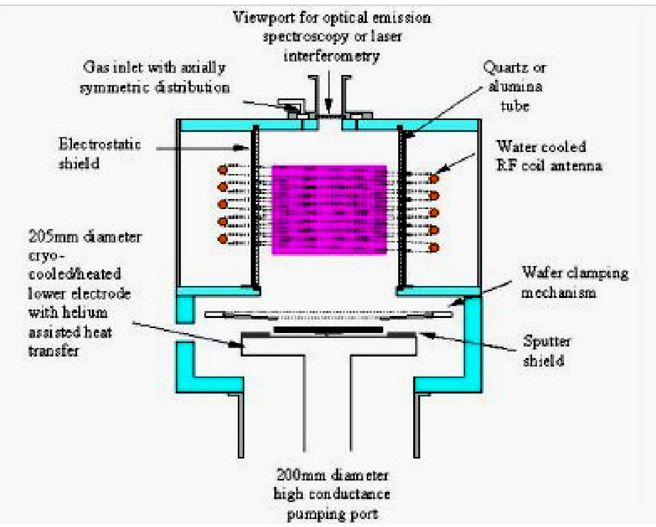

Figure 9.7: Structure of a ICP reactor, courtesy of Oxford Instruments

Etching of dielectric Can be performed with dry method by means of a Reactive Ion Etching - RIE machine using CF_4 plasma. This method is preferred to obtain anisotropic etching and thus abrupt sidewalls. SiO_2 and Si_3N_4 can be also removed by wet etching with Buffered Hydrofluoric Acid (BHF).

9.2.6 Annealing

The thermal annealing of the layers is important for a substantial improvement of the electrical properties and mobility in p-GaN. The introduction of Mg annealing by

Nakamura [23] allowed the break of Mg-H bondings that reduced the acceptor doping level. Mg passivation of the p-type GaN layer is achieved by means of a thermal treatment under N_2 or O_2 atmosphere, with temperature in the range of 500-800 °C. The rapid thermal annealing - RTA of the contacts is instead used to reduce the contact resistance.

9.3 Experimental Details

The basic idea of this work has been the deposition of a thin layer of ZnO over the GaN wafer to be used as transparent p-type contact by means of LP-CVD Low pressure Chemical Vapor Deposition. To better study the contact 3 different layer thickness has been deposited: 0.1 μm, 1 μm and 2 μm. The sample are named A2021-1, A2021-2, A2021-3 and A2021-R respectively for 0.1 μm, 1 μm, 2 μm ZnO thickness and reference sample for comparison.

The processing has been differentiated from the standard LED process which composed by substantially 3 steps: (i) p-contact deposition, (ii) mesa etching and (iii) n-type contact deposition.

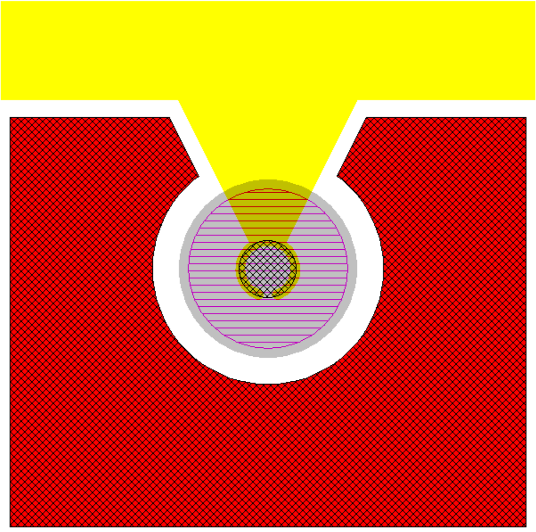

Figure 9.8: Mask layers for the processing of ZnO LEDs.

In order to develop the transparent conductive oxyde contact on the p-type GaN surface a different mask setup was required, it has been used a VCSEL mask structure (reported in Fig. 9.8. The VCSEL-Vertical Cavity Surface Emitting Laser structure is composed by a circular mesa where a DBR mirror, and a carrier confinement layer must be grown in order to achieve the laser operation. In our case only some of the masks necessary for the VCSEL have been used(in particular: Mesa, Aperture2, P contact and n contact). The processing has been carried out in a particular protective manner: ZnO is extremely sensible to acids and mechanical stresses. Its adhesion strength to the GaN is quite limited that can be removed with tweezers mishandling.

The purpose of this work was also to compare the final devices with a standard Semi-transparent contact LED. For this reason a reference LED A2021-R has been processed based on the same wafer but with a thin Ni/Au contact instead of ZnO.

The processing steps for the ZnO LEDs are reported in the following:

p-type annealing The annealing of the Mg has been performed as for the usual LED process under O_2 atmosphere at 600 °C.

ZnO etching After the first sample cleaning procedure, carried out without the use of acids, the lithography for the Mesa mask (in Grey in fig. 9.8) has been performed on the samples. The resist deposition has been carried out at a spinning speed of 3000rpm to obtain a thicker layer, since it will be used in auto-align process. The ZnO has been etched by means of highly diluted (1:100) HCl acid, the etching times were very reduced in the order of 10 to 30 seconds varying with the thickness of ZnO layer. ZnO is extremely sensible to acid etchant and much careful must be used to prevent underetch. This phase has been the most critical of the process and the etching has been carried out by means of consecutive step of few seconds in order to check the results with a microscope. Results are presented in fig. 9.9, 9.10, 9.11 for A2021-1, A2021-2 and A2021-3 respectively. As can be noticed there is a certain amount of under-etch, in particular for the A2021-1 sample in the order of 8-10 μm.

Mesa definition The mesa has been etched by means of Cl_2 Ar ICP reactor with a power of 50W, the photoresist has not been removed from the previous step, thus allowing an auto-aligment of the ZnO layer with the Mesa structure. The mesa height has been selected at 300nm.

Deposition of p-contact for the reference sample To generate a transparent contact on the reference device the mask ITO (purple horizontal lines in fig. 9.8) has been used by means of a negative lithography and lift off deposition. The deposition of the thin Ni/Au contact of 5/5nm has been followed by the thermal oxidation at 500 °C of the metal multilayer to generate the semitransparent contact.

Deposition of the SiO_2 The deposition of an isolation layer has been necessary in order to avoid short circuit between the two contacts respectively anode and cathode of the diode. An SiO_2 layer of 300nm has thus been deposited by means of PECVD.

Aperture To allow the deposition of the two contacts a negative lithography with the Aperture mask (diagonal black lines in fig. 9.8) has been performed. The result is that the samples are covered with photoresist and only two apertures are present for every device, the circular one in the center of the mesa (to allow the p-contact), and the n-contact region. The subsequent Dry etching by means of RIE eliminated the SiO_2 located in the apertures thus allowing the deposition of contacts.

p-metal deposition The deposition of the p-metal contact has been carried out by means of the p-contact mask (yellow area in fig. 9.8) with lift off technique. Since titanium guarantees the best adhesion and we have no problem of work function, for the ZnO contact it has been used Ti/Ni/Au multilayer with a thickness of 2/30/200nm respectively. In the case of the reference sample with Ni/Au semitransparent layer Ti/Au (3/200nm) contact has been used.

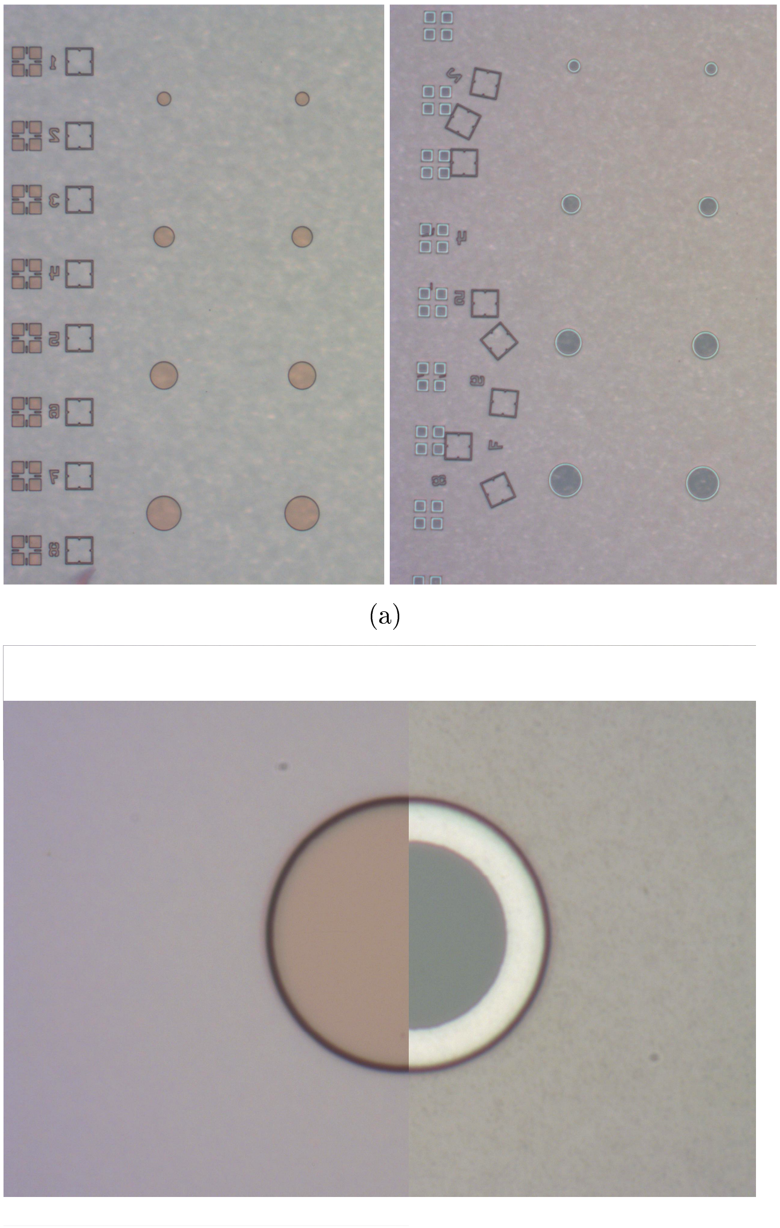

(a)

(b)

Figure 9.9: Before (left) and after (right) Etching of the ZnO on A2021-1 respectively at 2.5x (a) and 50x(b) zoom of the microscope.

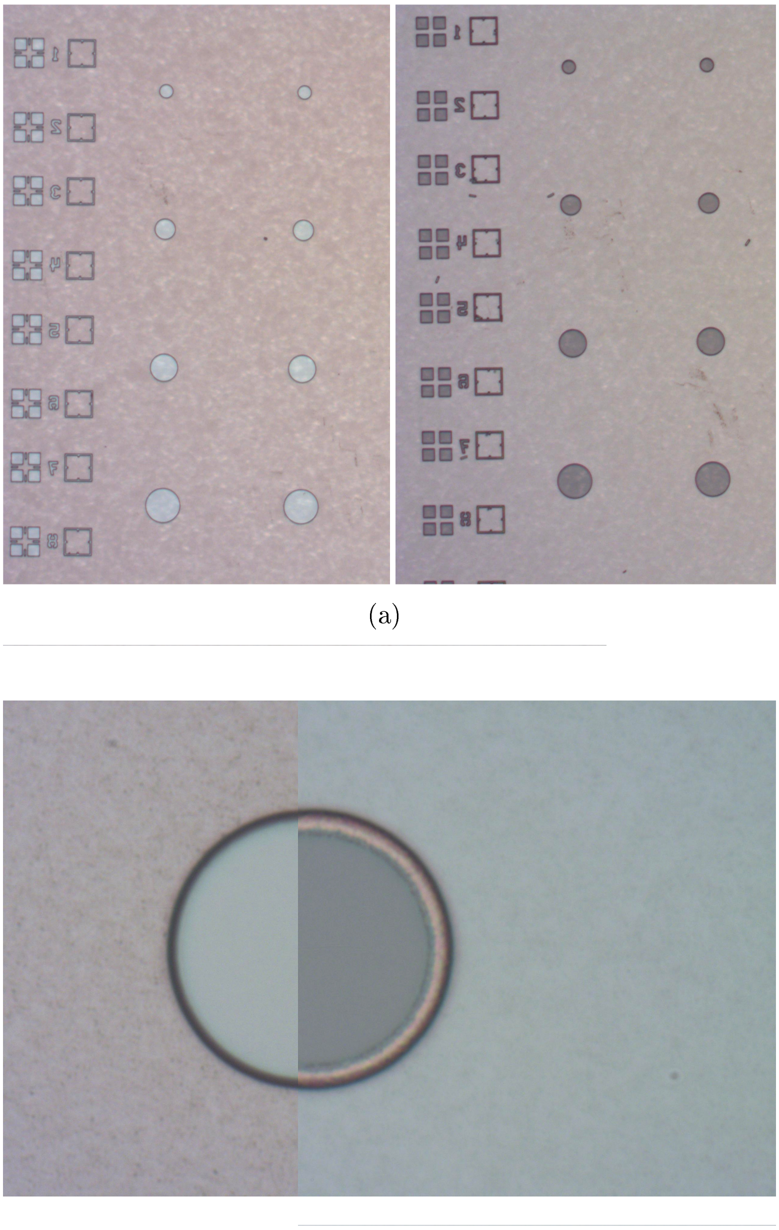

(a)

(b)

Figure 9.10: Before (left) and after (right) Etching of the ZnO on A2021-2 respectively at 2.5x (a) and 50x(b) zoom of the microscope.

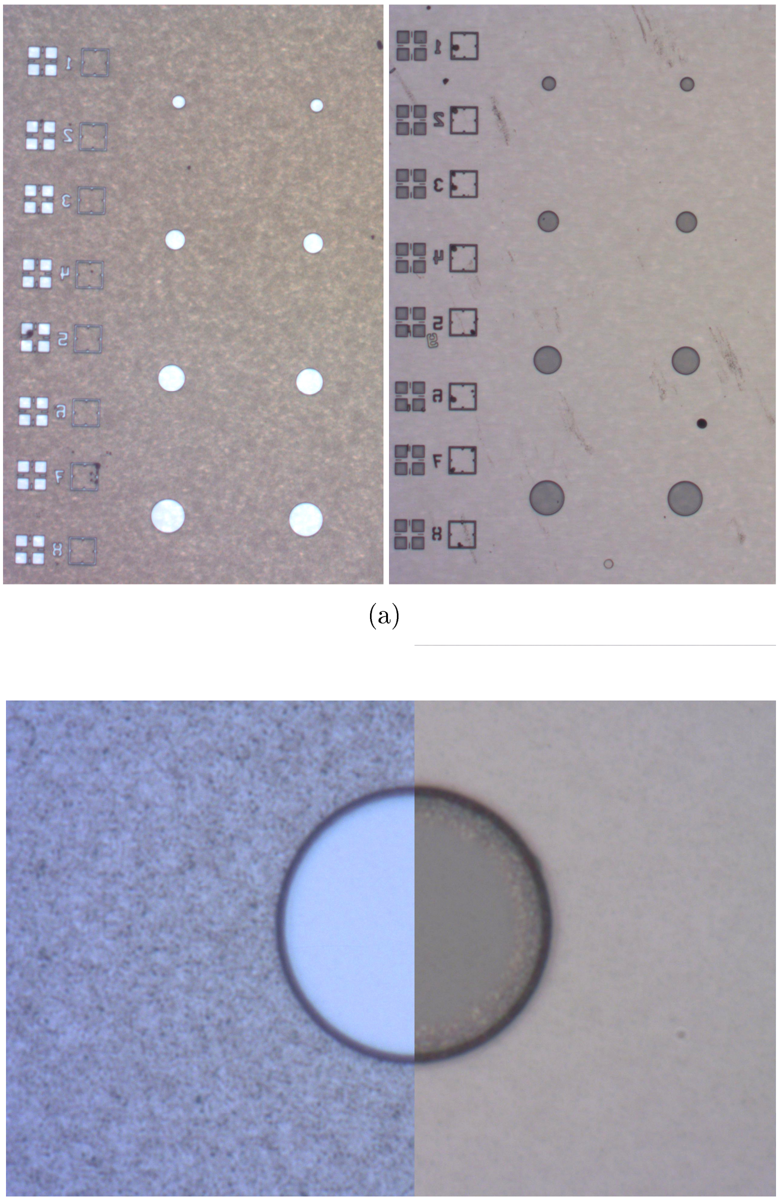

(a)

(b)

Figure 9.11: Before (left) and after (right) Etching of the ZnO on A2021-3 respectively at 2.5x (a) and 50x(b) zoom of the microscope.

n-metal deposition The deposition of the n-contact has been carried out as for the standard LED process with the n-contact mask (red area in fig. 9.8) negative lithography. Since the ZnO is now protected by the SiO_2 and the deposition is of the lift-off type (photoresist covers all the sample except the n-contact) it has been possible to properly clean and de-oxidate the surface prior to the deposition by means of BHF and HCl acid to ensure good electrical properties of the contact.

The completed device and an output emission map is reported in fig. 9.12.

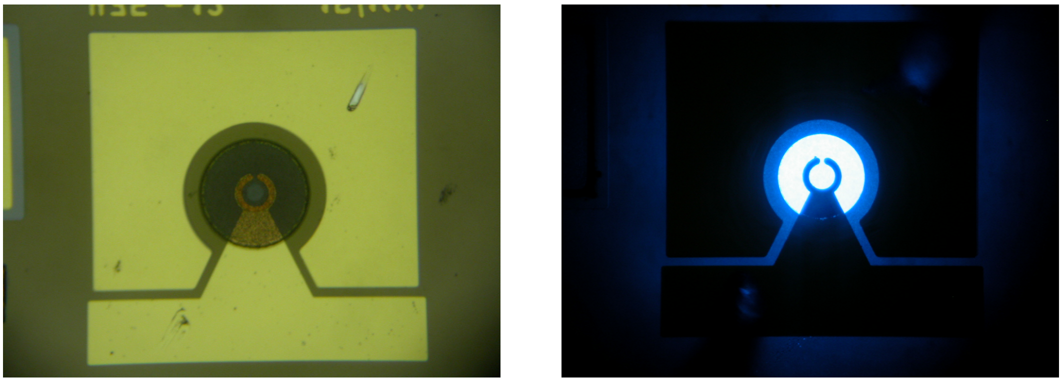

(a) (b)

Figure 9.12: (a) The complete process and final device, (b) The Output emission of a device from A2021-3 group.

9.4 Results

9.4.1 AFM measurements

The first interesting result is related to the deposition of the ZnO layer and the measurement of the roughness for the three different layer thicknesses. The results from AFM measurements indicate that the rms roughness increases with the increasing of the layer thickness and in particular it can be summarized as:

- A2021-1, ZnO thickness = $0.1\mu m$, rms roughness = 12.23nm;
- A2021-1, ZnO thickness = $1\mu m$, rms roughness = 53.06nm;
- A2021-1, ZnO thickness = $2\mu m$, rms roughness = 86.74nm.

It is important to notice that the superficial aspect of the layer varies substantially with the thickness, as reported in figures 9.13, 9.14 and 9.15 . Creation of separate crystals start to appear for higher thickness thus increasing the roughness.

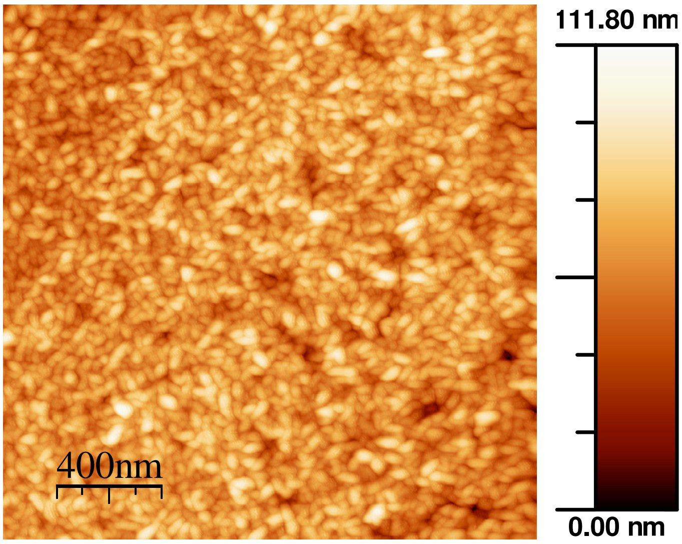

Figure 9.13: AFM measurement of the surface of sample A2021-1.

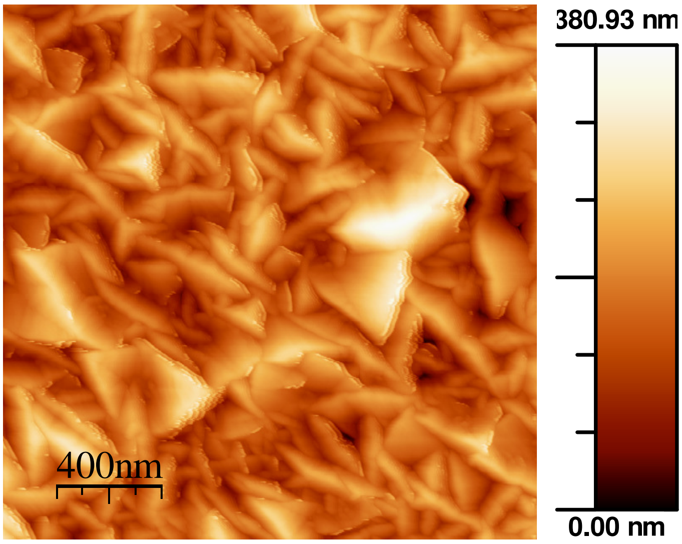

Figure 9.14: AFM measurement of the surface of sample A2021-2.

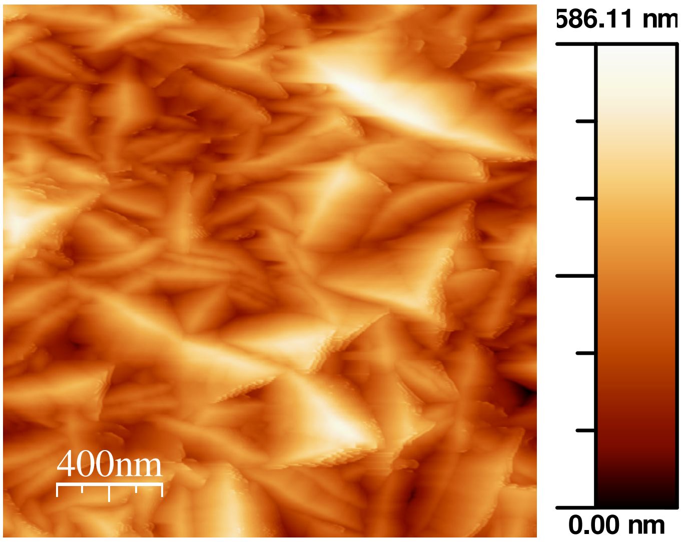

Figure 9.15: AFM measurement of the surface of sample A2021-3.

9.4.2 Electrical results

The electrical characterization of the samples are reported in fig. 9.16. Electrical properties are of great interest for the development of the contact. Since the structure are not optimized to have a reduced turn-on voltage it is still quite high, but independent from the contact type. The series resistance of the measured sample is instead a good indicator of the properties of the superficial contact. Results show that an increase of the thickness also contribute to the reduction of the series resistance of the devices, thus improving electrical characteristics. Electrical results are presented in fig. 9.16. The extrapolation of the Series resistances (R_S) from the electrical characteristics indicate a good increase of the conduction mechanisms as reported in table 9.1.

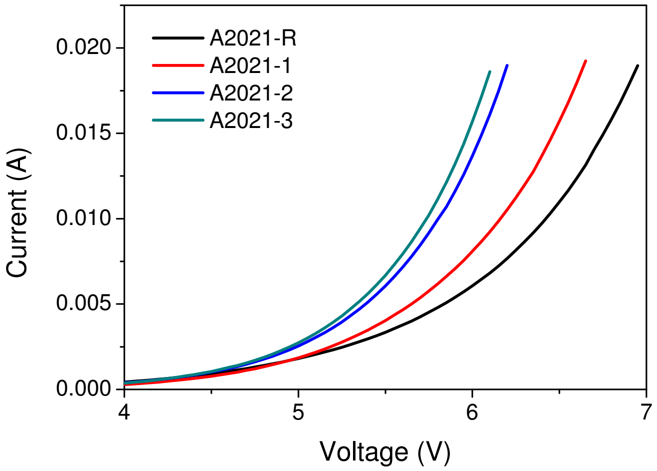

Figure 9.16: Comparison of Current-Voltage measurement of ZnO and reference sample.

Sample	Series Resistance
A2021-R	59.7 Ω
A2021-1	53.6 Ω
A2021-2	46.3 Ω
A2021-3	41.8 Ω

Table 9.1: Series Resistance for different samples.

9.4.3 Optical Results

Optical results are the most important and interesting for this study. In order to achieve a good statistics a large number of samples have been measured. Optical output has been measured both from top and bottom of the devices in order to have a better understanding of the device properties and effects of the different contact structure. A substantial increase of the optical output characteristic is detected both from top and bottom emission, see Fig. 9.17 and 9.17. The OP increases with the increase of the ZnO layer thickness and varies with the injection current. Observing the relative OP with respect to reference data (9.17(b) and 9.17(b)) it is possible to notice that the increase of OP is higher when measured from the TOP of the device rather then from bottom.

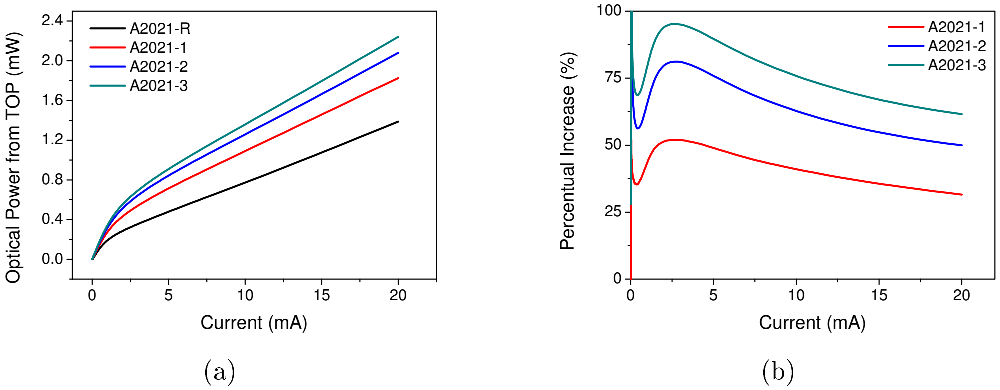

(a) (b)

Figure 9.17: (a)Comparison of Top Optical output vs Current measurement of ZnO and reference sample, (b) relative increase with respect to the reference sample.

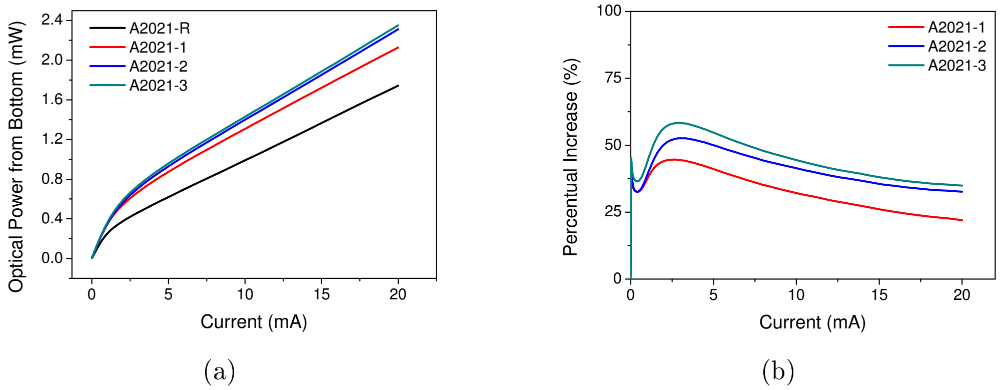

(a) (b)

Figure 9.18: (a)Comparison of Bottom Optical output vs Current measurement of ZnO and reference sample, (b) relative increase with respect to the reference sample.

9.5 Discussion

With this work it has been introduced a ZnO transparent conductive oxide (TCO) to be used as p-type contact with the purpose to increase extraction efficiency. A modified processing procedure has been carried out in order to integrate the TCO on the LED structure. Results have shown a substantial increase of the Optical output properties of the devices. Increasing the roughness of the ZnO contact the emitted OP also increase. It has also demonstrated that the extraction efficiency increase is more prominent when measuring the device from the top. This is ascribable to the surface toughness increase located only at the top of the device while no change is performed on the back surface (Shappire). It is though quite interesting to notice that a considerable increase of extraction efficiency is present also in the back of the device. To better understand the phenomena a graph reporting the correlation between rms roughness and OP increase (average value between 10 and 20mA) at the top and at the bottom of the sample has been plotted, see fig. 9.19.

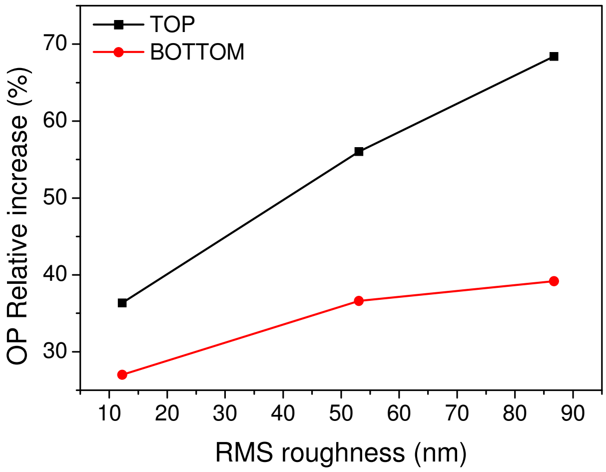

Figure 9.19: Correlation between OP relative increase with the rms roughness.

Observing Fig. 9.19 plot we notice that the TOP extraction efficiency increases almost linearly with the roughness of the p-contact, thus demonstrating that the surface roughness has a strong effect on the output power and a linear correlation with the extraction efficiency. The measurements carried out from the bottom show that the Extraction efficiency increase is not linear and start to saturate for higher values of rms roughness. Considering that the roughened surface is on the opposite side with respect to the measurement indicate that the increase of the roughness also increases the reflection of photons from the contact. To explain this phenomena different hypothesis have been formulated: (i) this mechanism is however limited by size of the ZnO crystals on the top of the contact that with an high vertical aspect ratio (for thick films of ZnO) convoy more easily the photon toward the air than back to the semiconductor; (ii) the increase of bottom extraction is related to the direction of photons, that must be inside the critical angle, photons may need to travel several time (from bottom to top) inside the LED structure prior to have the correct angle, thus increase the absorption probability.

Conclusions

During the Phd thesis period several aspects of GaN light emitting diodes have been studied and analyzed. In particular several efforts have been done in order to improve the knowledge about characterization and reliability of next generation Light emitting diodes and Laser Diode devices. The work carried out at DEI-University of Padova in strict cooperation with devices manufacturers, and has covered many different solutions and applications of Light Emitting Devices. The focus has been the comprehension of the emission, conduction and internal physical mechanism that determine both the device performance and reliability. Particular emphasis has been given toward the identification of the physical mechanisms and the failure modes related with the degradation of the different parts of the devices structure. During the work have been analyzed: (i) the emission properties and performances of GaN Laser Diodes for Blu-Ray systems, (ii) the degradation mechanisms that take place during operation life of LD, (iii) the role of different driving condition (i.e. current, temperature, optical field) in determining the degradation kinetics, (iv) study of the effects of degradation on LED-like sample to better understand the physical mechanism involved in LD reliability issues, (v) the study of the characteristics of AlGaN DUV LEDs and identification of degradation mechanisms, (vi) analysis of the physical mechanism responsible for reverse luminescence on InGaN Green LEDs, (vii) degradation analysis of Green LEDs subjected to reverse bias and ESD events, (viii) variation in the injection efficiency during ageing for near UV high brightness LEDs, (ix) the role of packaging and phosphores in the degradation and failure of low flux white LEDs. During the PhD visiting period the work has been instead focused on the comprehension development of new processing solution for GaN LED devices, in particular regarding the increase of performances of the devices. Transparent ZnO p-contact with intrinsic roughened surface has been adopted and studied. The PhD work has thus generated several achievement and interesting results that are reported in the following.

InGaN Laser Diode We have described an analysis of the degradation of Blu-ray (violet) LDs for application in high-density optical data storage systems. The research has been carried out by means of a wide set of ageing tests, and was aimed at understanding how the different driving forces (current, temperature, and optical field) influence the degradation rate. Stress was found to induce an increase in the threshold current of the devices, according to the square root of the stress time. This kind of degradation kinetic has been already described in previous literature reports, and ascribed to a defectŰimpurity diffusion process. We have shown that a significant correlation between the threshold current increase and the subthreshold emission decrease exists; this fact suggests that degradation is due to an increase in the nonradiative recombination rate in the active layer. Furthermore, we have shown that: 1) the degradation rate depends significantly on the stress current level; 2) LDs degradation occurs also below the lasing threshold current; 3) the degradation process is thermally activated, with activation energy equal to 250 meV (for stress at constant current, 70 mA); 4) pure thermal stress induces only a limited increase in the threshold current of the devices; and 5) the entity of the optical field does not play a key role in determining the degradation rate; 6) by means of an optical method we have extrapolated the non radiative lifetime during degradation and demonstrated that the threshold current increase is strictly correlated with the increase of non radiative recombination rate. The relevant results presented within this paper indicate that degradation is related to the increase in the nonradiative recombination in the active layer. The degradation process has been shown to be electrothermally activated, with a strong dependence on the stress current level and limited activation energy.

LED-like sample The research activities carried out on the LED-LIKE samples were aimed at understanding the possible correlation between the degradation of LED-LIKE and laser samples. we demonstrated that: 1) Stress can induce the degradation of the optical characteristics of LED-LIKE devices, 2)Degradation is more prominent at low measuring current levels, and this result suggests that the OP decrease is due to the increase in non-radiative recombination, 3) degradation kinetics have a square-root dependence on stress time. This result is consistent with our previous findings on laser diodes, and suggests that degradation is correlated to a diffusion process, 4) Defect-related (generation-recombination) components of the I-V curves show an abrupt decrease during the initial stage of the stress tests (not correlated to any modifications in the optical parameters), followed by a gradual increase according to the square-root of stress time. The gradual variation in the G/R components of the I-V curves is strongly correlated to the decrease in output power and 5) The C-V curves of the devices show modifications after stress. In particular we have detected: (i) a shift of the critical voltage towards higher levels, possibly due to the decrease in the generation-recombination components detected after stress; (ii) an increase in junction capacitance in the whole analyzed voltage region, possibly correlated to modifications in the electrical characteristics of the samples; (iii) no strong modifications in the apparent charge profiles.

AlGaN Deep Ultra Violet LEDs The reliability analysis carried out on AlGaN DUV LED operating at different emission wavelengths indicate that (i) gradual degradation is correlated to the increase in the non-radiative recombination in the active region of the devices; (ii) stress determines an increase in the defect-related current components of the LEDs, possibly due to an increase in the concentration of defects in the active region; (iii) stress determines an increase in the operating voltage of the LEDs and a decrease in junction capacitance; (iv) the degradation kinetics are strongly dependent on the stress current level, while operating temperature has only a limited impact on the degradation rate; (v) during stress the devices can show catastrophic degradation, due to the generation of parasitic conductive paths in parallel to the junction, in correspondence of the mesa borders.

Characterization and reliability of Green InGaN LED subjected to reverse bias We have described an analysis of the conduction and emission mechanisms of

LEDs submitted to reverse-bias polarization, as long as the effects of stress and ESD robustness tests. Results indicate that i) tunneling is the most important conduction mechanism responsible for reverse-bias leakage, (ii) the flow of reverse current can generate a bluish light emission, possibly due to the recombination of carriers in the QW region, (iii) reverse-bias emission is localized on a number of spots, possibly correlated with the presence of preferential paths for leakage current conduction, (iv) reverse-bias stress can induce an increase in the reverse current and RBL of the LEDs, due to the generation/propagation of defects in proximity of pre-existing leakage paths; (v) reverse-bias degradation is induced by highly accelerated carriers, injected by tunneling in the active region of the LEDs; (vi) the presence of structural defects can strongly limit the ESD robustness of the LEDs.

InGaN/GaN high power LEDs emitting at 420nm Stress tests carried out on 420nm HBLEDs indicate that different ageing mechanisms take place: i) a fast electrical and capacitive degradation probably related to a Mg passivation; ii) an OP degradation at high injection regime probably related to defect density increase, iii) a gradual OP increase at low injection regime correlated to an apparent charge decrease in QW region and possibly ascribed to a reduction of Diagonal Tunnelling during ageing, iv) a sudden decrease of OP caused by a localized ohmic shunt path.

Reliability of low flux GaN LEDs An electro-optical-thermal characterization and accelerated lifetime testing on different families of low-flux PC-LEDs has demonstrated that: (i) the degradation is correlated with the structure and the composition of the package, (ii) the output decay is thermally activated, (iii) the not-optimized matching between different materials composing the package can strongly affects the device reliability, (iv) the electrical treatment can induce catastrophic failures depending on the chip structure, (v) by means of failure analysis it has been demonstrated that during operation the detachment of the chip from the package can take place thus inducing the complete degradation of the LED characteristics. An exponential degradation model, suitable for the lifetime prediction has also been extrapolated from the analysis.

Processing of LED with ZnO p-contact A GaN LED structure has been processed by means of the deposition of a ZnO conductive layer to be used as p-contact deposited by LP-CVD and intrinsically roughned. The adopted processing procedure has demonstrated to be functional for the actual realization of the device. Analysis of different ZnO layer thickness and roughness demonstrated a substantial increase of the optical performances of the device as long as the reduction of the series resistance, when compared to a standard Ni/Au semi-transparent contact structure.

Bibliography

[1] J. Pankove, E. Miller, e J. Berkeyheiser, “Gan electroluminescent diodes,” *RCA review, technical journal*, vol. 32, no. 3, p. 283, 1971.

[2] M. Ikeda e S. Uchida, “Blue-violet laser diodes suitable for blu-ray disk,” *Physica status solidi (a)*, vol. 194, no. 2, pp. 407–313, 2002.

[3] A. Avramescu, T. Lermer, J. Müller, C. Eichler, G. Bruederl, M. Sabathil, S. Lutgen, e U. Strauss, “True green laser diodes at 524 nm with 50 mw continuous wave output power on c-plane gan,” *Applied Physics Express*, vol. 3, p. 061003, 2010.

[4] S. Nakamura, *et al.*, “High-power, long-lifetime ingan/gan/algan-based laser diodes grown on pure gan substrates,” *Japan Journal of Applied Physics*, vol. 37, pp. 309–312, 1998.

[5] M. Osinski, J. Zeller, P.-C. Chiu, B. S. Phillips, e D. B. Barton, “AlGaN/InGaN/GaN blue light emitting diode degradation under pulsed current stress,” *Appl. Phys. Lett.*, vol. 69, no. 7, pp. 898–900, 1996.

[6] D. L. Barton, M. Osinski, P. Perlin, P. G. Eliseev, e J. Lee, “Single-quantum well InGaN green light emitting diode degradation under high electrical stress,” *Microel. Reliab.*, vol. 39, pp. 1219–1227, 1999.

[7] T. Yanagisawa e T. Kojima, “Degradation of InGaN blue light-emitting diodes under continuous and low-speed pulse operations,” *Microel. Reliab.*, vol. 43, pp. 977–980, 2003.

[8] L. Sugiura, “Dislocation motion in gan light-emitting devices and its effect on device lifetime,” *Journal of Applied Physics*, vol. 81, no. 4, pp. 1633–1638, 1997.

[9] G. Meneghesso, S. Levada, R. Pierobon, F. Rampazzo, E. Zanoni, A. Cavallini, A. Castaldini, G. Scamarcio, S. Du, e I. E. and, “Degradation mechanisms of GaN-based LEDs after accelerated DC current aging,” in *IEEE International Electron Devices Meeting*, 2002.

[10] C. H. Seager, S. M. Myers, A. F. Wright, D. D. Koleske, e A. A. Allerman, “Drift, diffusion, and trapping of hydrogen in p type GaN,” *J. Appl. Phys.*, vol. 92, no. 12, pp. 7246–7252, 2002.

[11] A. Y. Polyakow, *et al.*, “Enhanced tunneling in GaN/InGaN multi-quantum well heterojunction diodes after short-term injection annealing,” *J. of Appl. Phys.*, vol. 91, no. 8, pp. 5203–5207, 2002.

[12] A. Zoroddu, F. Bernardini, V. Fiorentini, e P. Ruggerone, “Spontaneous polarization and piezoelectric constants of III-V Nitrides,” *Physical review B*, vol. 64, p. 045208, 2001.

[13] S. F. Chichibu, *et al.*, “Effective band gap inhomogeneity and piezoelectric field in ingan/gan multiquantum well structures,” *Appl. Phys. Lett.*, vol. 73, p. 2006, 1998.

[14] H. P. Maruska e J. J. Tietjen, “The preparation and properties of vapor-deposited single-crystal-line gan,” *Appl. Phys. Lett.*, vol. 15, no. 10, pp. 327–329, 1969.

[15] H. Amano, N. Sawaki, I. Akasaki, e Y. Toyoda, “Metalorganic vapor phase epitaxial growth of a high quality GaN film using an AlN buffer layer,” *Appl. Pyhs. Lett.*, vol. 48, pp. 353–355, 1986.

[16] K. Naniwaea, S. Itoha, H. Amanoa, K. Itoha, K. Hiramatsua, e I. Akasakia, “Growth of single crystal gan substrate using hydride vapor phase epitaxy,” *Journal of Crystal Growth*, vol. 99, no. 1-4, pp. 381–384, 1990.

[17] S. T. Kim, Y. J. Lee, D. C. Moon, C. H. Hong, e T. K. Yoo, “Preparation and properties of free-standing hvpe grown gan substrates,” *Journal of Crystal Growth*, vol. 194, no. 1, pp. 37–42, 1998.

[18] K. Motoki, *et al.*, “Preparation of large freestanding gan substrates by hydride vapor phase epitaxy using gaas as a starting substrate,” *Jpn. J. Appl. Phys.*, vol. 40, pp. 140–143, 2001.

[19] A. Cho e J. R. Arthur, “Molecular beam epitaxy,” *Progress in solid state chemistry*, vol. 10, p. 157, 1975.

[20] H. Hirayama, S. Fujikawa, N. Noguchi, J. Norimatsu, T. Takano, K. Tsubaki, e N. Kamata, “222Ű282 nm algan and inalgan-based deep-uv leds fabricated on high-quality aln on sapphire,” *Physica status solidi a*, vol. 206, no. 6, pp. 1176–1182, 2009.

[21] J. P.Zhang, H. M. Wang, M. E. Gaevski, C. Q. Chen, Q. Fareed, J. W. Yang, G. Sim, e M. A. Khan, “Crack-free thick algan grown on sapphire using aln/algan superlattices for strain management,” *Applied physics letters*, vol. 80, no. 19, pp. 3542–3544, 2002.

[22] H. Amano, M. Kito, K. Hiramatsu, e I. Akasaki, “P-type conduction in Mg-Doped GaN treated with low-energy electron beam irradiation (LEEBI),” *Jpn. J. Appl. Phys.*, vol. 28, pp. L2112–L2114, 1989.

[23] S. Nakamura, T. Mukai, M. Senoh, e N. Iwasa, “Thermal annealing effects on p-type mg-doped gan films,” *Japan Journal of Applied Phyics*, vol. 31, pp. L139–L142, 1992.

[24] S. J. Pearton, J. C. Zolper, R. J. Shul, e F. Ren, “GaN: Processing, defects and devices,” *J. Appl. Phys.*, vol. 86, no. 1, pp. 1–78, 1999.

[25] S. Tomiya, T. Hino, S. Goto, M. Takeya, e M. Ikeda, "Dislocation related issues in the degradation of GaN-based laser diodes," *IEEE Journal of Selected Topics in Quantum Electronics*, vol. 10, no. 6, pp. 1277–1286, 2004.

[26] E. F. Schubert, *Light Emitting Diodes*. Cambridge University Press, 2003.

[27] D. S. Lee, D. Byrnes, A. Parekh, S. Ting, e W. Quinn, "Carrier injection efficiency in nitride leds," *Journal of Crystal Growth*, vol. 310, no. 23, pp. 5158 – 5161, 2008.

[28] A. Hangleiter, D. Fuhrmann, M. Grewe, F. Hitzel, G. Klewer, S. Lahmann, C. Netzel, N. Riedel, e U. Rossow, "Towards understanding the emission efficiency of nitride quantum wells," *Physica Status Solidi A*, vol. 201, pp. 2808–2813, 2004.

[29] A. Getty, E. Matioli, M. Iza, C. Weisbuch, e J. S. Speck, "Electroluminescent measurement of the internal quantum efficiency of light emitting diodes," *Applied Physics Letters*, vol. 94, no. 18, p. 181102, 2009.

[30] M. Kneissl, D. Bour, L. Romano, C. V. de Walle, J. Northrup, W. Wong, D. Treat, M. Teepe, T. Schmidt, e N. Johnson, "Performance and degradation of continuous-wave InGaN multiple-quantum-well laser diodes on epitaxially laterally overgrown GaN substrates," *Appl. Phys. Lett.*, vol. 77, pp. 1931–1933, 2000.

[31] J. T. Hsu, J. D. Tsay, Y. D. Guo, C. C. Chuo, e S. M. Pan, "Efficiency enhancement of InGaN/GaN light-emitting diodes utilizing island-like GaN substrate," *Phys. Stat. Sol. (b)*, vol. 241, no. 12, pp. 2713–2716, 2004.

[32] M. Furitsch, *et al.*, "Comparison of degradation mechanisms of blue-violet laser diodes grown on SiC and GaN substrates," *Phys.Stat.Sol. (a)*, vol. 203, pp. 1797–1801, 2006.

[33] V. Kummler, G. Bruderl, S. Bader, S. Miller, A. Weimar, A. Lell, V. Harle, U. Schwartz, N. Gmeinwieser, e W. Wegscheider, "Degradation analysis of InGaN laser diodes," *Phys. Stat. Sol. (a)*, vol. 194, pp. 419–422, 2002.

[34] L. Marona, P. Wisniewski, P. Prystawko, I. Grzegory, T. Suski, S. Porowski, P. Perlin, R. Czernecki, e M. Leszczynski, "Degradation mechanisms in InGaN laser diodes grown on bulk gan crystals," *Applied Physics Letters*, vol. 88, no. 20, p. 201111, 2006.

[35] O. H. Nam, *et al.*, "Recent progress of high power GaN-based violet laser diodes," *Phys.Stat.Sol. (c)*, vol. 7, pp. 2278–2282, 2003.

[36] T. Schoedl, U. T. Schwarz, V. Kümmler, M. Furitsch, A. Leber, A. Miler, A. Lell, e V. Haerle, "Facet degradation of GaN heterostructure laser diodes," *Applied Physics Letters*, vol. 97, pp. 123 102–1–123 102–3, 2005.

[37] M. Miyachi, T. Tanaka, Y. Kimura, e H. Ota, "The activation of Mg in GaN by annealing with minority-carrier injection," *Appl. Phys. Lett.*, vol. 72, no. 9, pp. 1101–1104, 1998.

[38] F. Manyakhin, A. Kovalev, e A. E. Yunovich, “Aging mechanisms of InGaN/AlGaN/GaN light-emitting diodes operating at high currents,” *MRS Internet J. Nitride Semicond. Res.*, vol. 53, no. 3, pp. 1–6, 1998.

[39] M. Takeya, T. Mizuno, T. S. S. Ikeda, T. Fujimoto, Y. Ohfuji, K. Oikawa, Y. Yabuki, S. Uchida, e M. Ikeda, “Degradation in AlGaInN lasers,” *Phys. Stat. Sol. (c)*, vol. 7, pp. 2292–2295, 2003.

[40] L. A. Coldren e S. W. Corzine, *Diode Lasers and Photonic Integrated Circuits.* John Wiley & Sons, 1995.

[41] C. J. Pan e G. C. Chi, “The doping of GaN with Mg diffusion ,” *Solid-State Electronics*, vol. 43, no. 3, pp. 621–623, 1999.

[42] Rafal Jakiela and Adam Barcz and Ewa Dumiszewska and Andrzej Jagoda, “Si diffusion in epitaxial GaN ,” *Physica status solidi (c)*, vol. 3, no. 6, pp. 1416–1419, 2006.

[43] C. J. Pan and G. C. Chi and B. J. Pong and J. K. Sheu and and J. Y. Chen , “Si diffusion in p-GaN ,” *Journal of Vacuum Science and Technology B*, vol. 22, p. 1727, 2004.

[44] S. Limpijumnong e C. G. V. de Walle, “Diffusivity of native defects in GaN,” *Physica Review B*, vol. 69, no. 3, p. 035207, 2004.

[45] M. Ikeda, T. Mizuno, M. Takeya, S. Goto, S. Ikeda, T. Fujimoto, Y. Ohfuji, e T. Hashizu, “High-power gan-based semiconductor lasers,” *Physica Status Solidi (C)*, vol. 1, no. 6, pp. 1461–1467, 2004.

[46] T. Asano, *et al.*, “Over 100-mw blue-violet laser diodes for blu-ray disc system,” *Proceedings of SPIE*, vol. 5365, pp. 297–305, 2004.

[47] S. Nakamura, “Ingan-based laser diodes with an estimated lifetime of longer than 10 000 hours,” *Proceedings of SPIE*, vol. 3283, no. 2, p. v, 2004.

[48] C. van Opdorp e G. Hooft, “Method for determining effective nonradiative lifetime and leakage losses in double-heterostructure lasers,” *Journal of Applied Physics*, vol. 52, p. 3827, 1981.

[49] Y. C. Shen, G. O. Mueller, S. Watanabe, N. F. Gardner, A. Munkholm, e M. R. Krames, “Auger recombination in ingan measured by photoluminescence,” *Applied Physics Letter*, vol. 91, p. 141101, 2007.

[50] H. Y. Ryu, K. H. Ha, J. H. Chae, K. S. Kim, J. K. Son, O. H. Nam, Y. J. Park, e J. I. Shim, “Evaluation of radiative efficiency in ingan blue-violet laser-diode structures using electroluminescence characteristics,” *Applied Physics Letters*, vol. 89, no. 17, p. 171106, 2006.

[51] J. Müller, G. Brüderl, M. Schillgalies, S. Tautz, D. Dini, A. Breidenassel, B. Galler, e S. Lutgen, “Burn-in mechanism of 450 nm ingan ridge laser test structures,” *Applied Physics Letters*, vol. 95, no. 5.

[52] M. Khizar, Z. Y. Fan, K. H. Kim, J. Y. Lin, e H. X. Jiang, “Nitride deep-ultraviolet light-emitting diodes with microlens array,” *Applied Physics Letters*, vol. 86, pp. 173 504–1–173 504–3, 2005.

[53] Y. Xi e E. F. Schubert, “Junction temperature measurement in GaN ultraviolet light emitting diodes using diode forward voltage method,” *Appl. Phys. Lett.*, vol. 86, no. 12, pp. 2163–2165, 2004.

[54] F. Rossi, *et al.*, “Influence of shortterm lowcurrent dcaging on the electrical and optical properties of AlGaN blue Light-Emitting Diodes ,” *J. Appl. Phys.*, vol. 99, pp. 053 104–1–053 104–7, 2006.

[55] J. P. Zhang, *et al.*, “Algan-based 280 nm lightemitting diodes with continuous-wave power exceeding 1 mwat 25 ma,” *Applied physics letters*, vol. 85, no. 23, p. 5532Ű5534, 2004.

[56] K. X. Chen, Y. A. Xi, F. W. Mont, J. K. Kim, E. F. Schubert, W. Liu, X. Li, e J. A. Smart, “Recombination dynamics in ultraviolet lightemitting diodes with Si-doped $Al_xGa_{1-x}N/Al_yGa_{1-y}N$ multiple quantum well active regions,” *Journal of Applied Physics*, vol. 101, no. 11, p. 113, 1996.

[57] A. A. Allerman, M. H.Crawford, A. J. Fisher, K. H. A. Bogart, S. R. Lee, D. M. Follstaedt, P. P. Provencio, e D. D. Koleste, “Growth and design of deep-UV (240-290 nm) light emitting diodes using AlGaN alloys,” *J. of Crys. Growth*, vol. 272, pp. 227–241, 2004.

[58] P. N. Grillot, M. R. Krames, H. Zhao, e S. H. Teoh, “Sixty Thousand Hour Light Output Reliability of AlGaInP Light Emitting Diodes,” *IEEE Transactions on Devices and Materials Reliability*, vol. 6, no. 4, pp. 564–574, 2006.

[59] X. A. Cao e S. F. LeBoeuf, “Current and temperature dependent characteristics of deep-ultraviolet light-emitting diodes,” *IEEE Transaction on Electron Devices*, vol. 54, no. 12, pp. 3414–3417, 2007.

[60] O. Pursiainen, N. Linder, A. Jeager, e R. Oberschmid, “Identification of aging mechanism in the optical and electrical characteristics of light-emitting diodes,” *Appl. Phys. Lett.*, vol. 79, no. 18, pp. 2895–2897, 2001.

[61] C. R. Moon, B. D. Choe, S. D. Kwon, H. K. Shin, e H. J. Lim, “Electron distribution and capacitance-voltage characteristics of n-doped quantum wells,” *J. Appl. Phys.*, vol. 84, no. 5, pp. 2673–2683, 1998.

[62] C. R. Moon e H. J. Lim, “Influence of quantum well structural parameters on capacitance-voltage characteristics,” *Appl. Phys. Lett.*, vol. 74, no. 20, pp. 2987–2989, 1999.

[63] M. Shatalov, *et al.*, “Time-resolved electroluminescence of algan-based light-emitting diodes with emission at 285 nm,” *Applied physics letters*, vol. 82, no. 2, pp. 167–168, 2003.

[64] Y. Xia, E. Williams, Y. Park, I. Yilmaz, J. Shah, E. Schubert, e C. Wetzel, "Discrete steps in the capacitance-voltage characteristics of GaInN/GaN light emitting diode structures," in *Mater. Res. Soc. Symp. Proc. Vol. 831*, 2005.

[65] O. Pursiainen, N. Linder, A. Jeager, e R. Oberschmid, "Identification of aging mechanism in the optical and electrical characteristics of light emitting diodes," *Appl. Phys. Lett.*, vol. 79, no. 18, pp. 2895–2897, 2001.

[66] Y. Xi, J.-Q. Xi, T. Gessmann, J. M. Shah, J. K. Kim, E. F. Schubert, A. J. Fischer, M. H. Crawford, K. H. A. Bogart, e A. A. Allerman, "Junction and carrier temperature measurements in deep ultraviolet light emitting diodes using three different methods," *Appl. Phys. Lett.*, vol. 86, pp. 031 907–1–031 907–3, 2005.

[67] M. Meneghini, L. Trevisanello, U. Zehnder, T. Zahner, U. Strauss, G. Meneghesso, e E. Zanoni, "High-temperature degradation of GaN LEDs related to passivation," *IEEE Transactions on Electron Devices*, vol. 53, no. 12, pp. 2981–2987, 2006.

[68] S. M. Myers, S. H. Seager, A. F. Wright, e B. L. Vaandrager, "Electron-beam dissociation of the MgH complex in p-type GaN," *J. Appl. Phys.*, vol. 92, no. 11, pp. 6630–6635, 2002.

[69] M. Meneghini, L.-R. Trevisanello, G. Meneghesso, e E. Zanoni, "A review on the reliability of gan-based leds," *IEEE Transactions on Device and Materials Reliability*, vol. 8, no. 2, pp. 323–331, 2008.

[70] R. Dupuis e M. Krames, "History, development, and applications of high-brightness visible light-emitting diodes," *Journal of Lightwave Technology*, vol. 26, no. 9, pp. 1154 – 1171, 2008.

[71] J. C. Brooksby, J. Mei, e F. A. Ponce, "Correlation of spectral luminescence with threading dislocations in green-light-emitting ingan quantum wells," *Applied Physics Letters*, vol. 90, p. 231901, 2007.

[72] J.-H. Ryou, W. Lee, J. Limb, D. Yoo, J. P. Liu, R. D. Dupuis, Z. H. Wu, A. M. Fischer, e F. A. Ponce, "Control of quantum-confined stark effect in ingan/gan multiple quantum well active region by p-type layer for iii-nitride-based visible light emitting diodes," *Applied Physics Letters*, vol. 92, p. 101113, 2008.

[73] M. F. Schubert, S. Chhajed, J. K. Kim, E. F. Schubert, D. D. Koleske, M. H. Crawford, S. R. Lee, A. J. Fischer, G. Thaler, e M. A. Banas, "Effect of dislocation density on efficiency droop in gainn/gan light-emitting diodes," *Appl. Phys. Lett.*, vol. 91, p. 231114, 2007.

[74] X. A. Cao e S. D. Arthur, "High-power and reliable operation of vertical light-emitting diodes on bulk GaN," *Appl. Phys. Lett.*, vol. 85, pp. 3971–3973, 2004.

[75] X. A. Cao, *et al.*, "Investigation of radiative tunneling in gan/ingan single quantum well light-emitting diodes," *Solid-State Electronics*, vol. 46, pp. 2291–2294, 2002.

[76] H. Kuan, “High Electrostatic Discharge Protection Using Multiple Si:N/GaN and Si:N/Si:GaN Layers in GaN-Based Light Emitting DiodesŤ,” *Japan Journal of Applied Physics*, vol. 47, p. 1544, 2008.

[77] X. A. Cao, P. M. Sandvik, S. F. LeBoeuf, e S. D. Arthur, “Defect generation in InGaN/GaN light-emitting diodes under forward and reverse electrical stresses,” *Microel. Reliab.*, vol. 43, pp. 1987–1991, 2003.

[78] S. Jeon, J. Lee, E. Park, J. Jang, J. Lim, S. Kim, , e J. Park, “The effect of the internal capacitance of InGaN-light emitting diode on the electrostatic discharge properties,” *Applied Physics Letters*, vol. 94, p. 13106, 2009.

[79] M. Peter, A. Laubsch, P. Stauss, A. Walter, J. Baur, e B. Hahn, “Green ThinGaN power-LED demonstrates 100 lm,” *Physica status solidi (c)*, vol. 5, no. 6, pp. 2050–2052, 2008.

[80] Z.-Q. Fang, D. C. Reynolds, e L. D. C, “Changes in electrical characteristics associated with degradation on InGaN blue light emitting diodes,” *J. of Elect. Mat.*, pp. 448–451, 2000.

[81] Y. D. Jho, J. S. Yahng, E. Oh, , e D. S. Kim, “Field-dependent carrier decay dynamics in strained InxGa1-xN/GaN quantum wells,” *Physica Review B*, vol. 66, p. 035334, 2002.

[82] J. W. Robinson, J. H. Rice, K. H. Lee, J. H. Na, R. A. Taylor, D. G. Hasko, R. A. Oliver, M. J. Kappers, C. J. Humphreys, e G. A. D. Briggs, “Quantum-confined Stark effect in a single InGaN quantum dot under a lateral electric field,” *Applied Physics Letters*, vol. 86, no. 21, p. 213103, 2005.

[83] G. Blume, “AlGaInN resonant-cavity LED devices studied by electromodulated reflectance and carrier lifetime techniques,” *IEEE Proceedings, Optoelectronics*, vol. 152, no. 2, p. 118, 2005.

[84] Y. D. Jho, J. S. Yahng, E. Oh, e D. S. Kim, “AlGaInN resonant-cavity LED devices studied by electromodulated reflectance and carrier lifetime techniques,” *Physical Review B*, vol. 66, p. 035334, 2002.

[85] M. F. Schubert, J. Xu, Q. Dai, F. W. Mont, J. K. Kim, e E. F. Schuber, “On resonant optical excitation and carrier escape in gainn/gan quantum wells,” *Applied Physics Letters*, vol. 94, no. 8, p. 081114, 2009.

[86] A. Hangleiter, F. Hitzel, C. Netzel, D. Fuhrmann, U. Rossow, G. Ade, e P. Hinze, “Suppression of nonradiative recombination by v-shaped pits in $gainn/gan$ quantum wells produces a large increase in the light emission efficiency,” *Phys. Rev. Lett.*, vol. 95, no. 12, p. 127402, 2005.

[87] P. Schlotter, J. Baur, C. Hielscher, M. Kunzer, H. Obloh, R. Schmidt, e J. Schneider, “Fabrication and characterization of gan/ingan/algan double heterostructure leds and their application in luminescence conversion leds,” *Materials Science and Engineering B*, vol. 59, no. 1-3.

[88] L. Ching-Ting e K. Hsiao-Wei, "Long-term thermal stability of ti/al/pt/au ohmic contacts to n-type gan," *Applied Physics Letters*, vol. 76, no. 17.

[89] D. Yan, H. Lu, D. Chen, R. Zhang, e Y. Zheng, "Forward tunneling current in gan-based blue light-emitting diodes," *Applied Physics Letters*, vol. 96, no. 8.

[90] U. Zehnder, B. Hahn, J. Baur, M. Peter, S. Bader, H. J. Lugauer, e A. Weimar, "Gainn leds: straight way for solid state lighting," vol. 6797.

[91] C. Sommer, F. P. Wenzl, P. Hartmann, P. Pachler, M. Schweighart, G. Leising, e S. Tasch, "Silicate phosphors and white led technology: improvements and opportunities," I. T. Ferguson, N. Narendran, T. Taguchi, e I. E. Ashdown, Eds., vol. 6669, no. 1. SPIE, 2007, p. 66690O.

[92] N. Narendran, Y. Gu, J. P. Freyssinier, H. Yu, e L. Deng, "Solid-state lightning: failure analysis of white LEDs," *J. of Crys. Growth*, vol. 268, pp. 449–456, 2004.

[93] T. R. Philips Lumileds, "Gainn leds: straight way for solid state lighting," vol. 6797.

[94] T. Yanagisawa, "Estimation of the degradation of InGaN/AlGaN blue light-emitting diodes," *Microel. Reliab.*, vol. 37, no. 8, pp. 1239–1241, 1997.

[95] S. Levada, M. Meneghini, G. Meneghesso, e E. Zanoni, "Analysis of DC current accelerated life tests of GaN LEDs using a weibull-based statistical model," *IEEE Transactions on Device and Materials Reliability*, vol. 5, no. 4, pp. 688–693, 2005.

[96] S. Ishizaki, H. Kimura, e M. Sugimoto, "Lifetime estimation of high power LEDs," *J. Light & Vis. Env.*, vol. 31, no. 1, pp. 11–18, 2007.

[97] L. Trevisanello, M. Meneghini, G. Mura, M. Vanzi, M. Pavesi, G. Meneghesso, e E. Zanoni, "Accelerated life test of high brightness light emitting diodes," *IEEE Transactions on Device and Materials Reliability*, vol. 8, no. 2, p. 304Ũ311, 2008.

[98] J. K. Sheu, Y. K. Su, G. C. Chi, P. L. Koh, M. J. Jou, C. M. Chang, C. C. Liu, e W. C. Hung, "High-transparency ni/au ohmic contact to p-type gan," *Applied Physics Letters*, vol. 74, no. 16, pp. 2340–2342, 1999.

[99] T. Fujii, Y. Gao, R. Sharma, E. L. Hu, S. P. DenBaars, e S. Nakamura, "Increase in the extraction efficiency of gan-based light-emitting diodes via surface roughening," *Applied Physics Letters*, vol. 84, no. 6, pp. 855–857, 2004.

[100] D.-H. Kim, *et al.*, "Enhanced light extraction from gan-based light-emitting diodes with holographically generated two-dimensional photonic crystal patterns," *Applied Physics Letters*, vol. 87, no. 20, p. 203508, 2005.

[101] E. Reichmanis e C. Wong, *The chemistry of polymers for microlithographic applications, Polymers for electronic and photonic applications.* Academic press, San Diego, 1993.

[102] J. M. Shaw, J. D. Gelorme, N. C. LaBianca, W. E. Conley, e S. J. Holmes, "Negative photoresists for optical lithography," *IBM Journal of Research and Development*, vol. 41, no. 1.2.

[103] M. E. Lin, Z. Ma, F. Y. Huang, Z. F. Fan, L. H. Allen, e H. Morkoç, “Low resistance ohmic contacts on wide band-gap gan,” *Applied Physics Letters*, vol. 64, no. 8, pp. 1003–1005, 1994.

[104] Z. Fan, S. N. Mohammad, W. Kim, Özgür Aktas, A. E. Botchkarev, e H. Morkoç, “Very low resistance multilayer ohmic contact to n-gan,” *Applied Physics Letters*, vol. 68, no. 12, pp. 1672–1674, 1996.

[105] G. J. Dolan, “Offset masks for lift-off photoprocessing,” *Applied Physics Letters*, vol. 31, no. 5, pp. 337–339, 1977.

[106] S. Nakamura, M. Senoh, S. ichi Nagahama, N. Iwasa, T. Yamada, T. Matsushita, H. Kiyoku, e Y. Sugimoto, “Characteristics of ingan multi-quantum-well-structure laser diodes,” *Applied Physics Letters*, vol. 68, no. 23, pp. 3269–3271, 1996.

[107] B. Green, K. Chu, E. Chumbes, J. Smart, J. Shealy, e L. Eastman, “The effect of surface passivation on the microwave characteristics of undoped algan/gan hemts,” *IEEE Electron Device Letters*, vol. 21, no. 6, pp. 268–270, 2000.

[108] “On the nitrogen and oxygen incorporation in plasma-enhanced chemical vapor deposition (pecvd) sioxny films,” *Thin Solid Films*, vol. 402, no. 1-2, pp. 154 – 161, 2002.

[109] D. A. Stocker, E. F. Schubert, e J. M. Redwing, “Crystallographic wet chemical etching of gan,” *Applied Physics Letters*, vol. 73, no. 18, pp. 2654–2656, 1998.

[110] J. R. Mileham, S. J. Pearton, C. R. Abernathy, J. D. MacKenzie, R. J. Shul, e S. P. Kilcoyne, “Patterning of aln, inn, and gan in koh-based solutions,” vol. 14, no. 3. AVS, 1996, pp. 836–839.

[111] H. M. Ng, N. G. Weimann, e A. Chowdhury, “Gan nanotip pyramids formed by anisotropic etching,” *Journal of Applied Physics*, vol. 94, no. 1, pp. 650–653, 2003.

[112] S. J. Pearton, R. J. Shuf, G. . F. M. Lane, e C. Constantine, “Dry etching of iii-v nitrides,” vol. 395.

[113] R. J. Shul, G. B. McClellan, S. A. Casalnuovo, D. J. Rieger, S. J. Pearton, C. Constantine, C. Barratt, J. R. F. Karlicek, C. Tran, e M. Schurman, “Inductively coupled plasma etching of gan,” *Applied Physics Letters*, vol. 69, no. 8, pp. 1119–1121, 1996.